2019

Adhesion of bituminous and cementitious materials using Particle-Probe Scanning Force Microscopy

Yujie Li
University of Vermont

ADHESION OF BITUMINOUS AND CEMENTITIOUS MATERIALS USING PARTICLE-PROBE SCANNING FORCE MICROSCOPY

A Dissertation Presented

by

Yujie Li

to

The Faculty of the Graduate College

of

The University of Vermont

In Partial Fulfillment of the Requirements
for the Degree of Doctor of Philosophy
Specializing in Civil and Environmental Engineering

January, 2019

Defense Date: November 5, 2018
Thesis Examination Committee:

Ting Tan, Ph.D., Advisor
Jie Yang, Ph.D., Chairperson
Frederic Sansoz, Ph.D.
George Pinder, Ph.D.
Appala Raju Badireddy, Ph.D.
Cynthia J. Forehand, Ph.D., Dean of the Graduate College

ABSTRACT

As the most important materials in civil engineering, bituminous and cementitious materials have been used widely in pavements and constructions for many years. Accurate determination of adhesion is important to the bonding properties of bituminous and cementitious materials. In this work, we presented a novel approach to measure the adhesion between binders and aggregate mineral particles at microscopic scale.

Particle probe scanning force microscopes (SFM) were used to study the adhesion between mineral microspheres representing the primary aggregate constituents (Al_2O_3, SiO_2 and $CaCO_3$) and various control (PG 64-22 and PG 58-22) and modified binders. Results showed that these modified SFM probes could effectively measure the adhesion between binders and aggregate minerals. Consistent adhesion measurements were obtained between different asphalt binders and aggregate mineral particles. Statistical analyses were performed to evaluate effects of different factors on the aggregate-modified binder adhesion, including aggregate constituents, binder types, modifier types and cantilever properties. Due to the stronger polarity of alumina particles, stronger interactions occur within alumina-binder pairs than within silica- and calcium carbonate-binder pairs. Meanwhile, morphologies of different modified binders clearly demonstrated microstructural variations in these binders.

The adhesion between steel and different cement hydrated products was measured using particle probe SFM. Adhesive forces are collected between steel microspheres and new (four-week old) and old (six-month old) cement in air and saturated lime water. Mixed Gaussian models were applied to predict phase distributions in the cement paste, i.e., low density C-S-H, high density C-S-H, CH, other hydrated products and the unreacted components. For new cement in saturated lime water, adhesive forces between steel and low density C-S-H, high density C-S-H and other hydrated products are intermediate among all groups selected. The adhesive forces between steel and calcium hydroxide are smallest, whereas the adhesive forces between steel and the unreacted phases are largest. For the six-month old cement, the interweaving of calcium carbonate crystals and C-S-H during the carbonation produces greater adhesive forces to steel, consistent with the adhesive forces between steel and the control calcium carbonate specimen. CH turned into calcium carbonate by reacting with carbon dioxide in air. An increase in adhesive forces was found between steel and calcium carbonate in the old cement than those between steel and CH in the new cement.

Particle probe SFM is able to measure the adhesion in bimaterials. For bituminous materials, this methodology provides opportunities to evaluate the effects of different processing methods and to generate quantitative information for the development of multi-scale asphalt mixture cracking models. For cementitious materials, these studies opened new avenues to study the interactions between steel and cement at microscale under a variety of environmental conditions and can be formulated as crack initiation and propagation criteria incorporated in multiscale models for reinforced concrete structures.

Keywords- *adhesion, bituminous materials, mineral aggregates, steel, cement, particle probe scanning force microscopy*

CITATIONS

Material from this dissertation has been published in the following form:

Li, Y., Yang, J., Hughes, J and Tan, T.. (2018). “An experimental study on adhesion between steel and cement pastes using particle probe scanning force microscopy”, *Journal of the American Ceramic Society*, https://doi.org/10.1111/jace.15971.

Li, Y., Yang, J., and Tan, T.. (2018). “Measuring adhesion between early-stage cement and steel using particle probe scanning force microscopy”, *Cement and Concrete Composites*, 90, 126-135.

Li, Y., Yang, J., and Tan, T.. (2017). “Adhesion between Modified Binders and Aggregate Minerals at Ambient Conditions Measured with Particle-Probe Scanning Force Microscopes”. *Journal of Materials in Civil Engineering*, 29(8), 04017068.

Li, Y., Yang, J., and Tan, T.. (2017). “Statistical analyses of aggregate mineral-binder adhesion measured using particle probe scanning force microscopes”, *Transportation Research Record: Journal of the Transportation Research Board*, doi:10.3141/2632-03.

Li, Y., Yang, J., and Tan, T.. (2016). “Measuring adhesion between modified asphalt binders and aggregate minerals use of particle probe scanning force microscopes”, *Transportation Research Record: Journal of the Transportation Research Board*, 2574, 117-123

Li, Y., Yang, J., and Tan, T.. (2015). “Study on adhesion between asphalt binders and aggregate minerals under ambient conditions using particle-modified atomic force microscope probes", *Construction and Building Materials*, 101, 159-165.

ACKNOWLEDGEMENTS

I would like to thank my advisor Prof. Ting Tan and co-advisor Prof. Jie Yang for their excellent guidance, not only as advisors but also mentors of life. Without their numerous time, energy and patience, I cannot build this thesis. Besides my advisors, I would like to thank the rest of my thesis committee: Prof. George Pinder and Prof. Frederic Sansoz and Prof. Appala Raju Badireddy for their insightful comments and valuable guidance. I would like to acknowledge the help and collaboration of Prof. John Hughes, Prof. Keith Mintz and Dr. Kristin Schutz in providing XRD and the facilities to synthesize C-S-H gels. I would particularly like to thank my friends and the members of my research group who helped and supported me throughout this venture. My sincere thanks also goes to Michele von Turkovich and Troy Pauli at the UVM microscopy imaging center and Dr. Joseph Boesenberg at Brown University for the assistance of image characterization. Finally, I would like to take this opportunity to express sincere gratitude to my parents and my boyfriend for their love, understanding and unceasing encouragement and support.

TABLE OF CONTENTS

Page

LIST OF TABLES

LIST OF FIGURES

CHAPTER 1: INTRODUCTION AND BACKGROUND

As the most important materials in civil engineering, bituminous and cementitious materials have been used widely in pavements and constructions for many years.

1.1 Bituminous materials

Bituminous materials have been extensively used for roadway constructions. The United States has the largest highway systems consisting of 4,092,730 miles in the world [1]. The failure of roadway infrastructure causes significant cost to the human society. An AASHTO report [2] estimated that that only half of the major US roads are in good condition, whereas 13 percent are in poor condition. Each year, the construction and maintenance costs for the US roadway infrastructure are approximately $100 billion dollars [3], with asphalt paving as the largest portion. More than $30 billion asphalt materials are produced by US plants annually [4]. Therefore, it is critical to produce and maintain high performance pavement materials.

Bituminous materials consist of bitumen which is a black or dark solid or viscous cementitious substances consists chiefly high molecular weight hydrocarbons derived from distillation of petroleum or natural asphalt. Bitumen has adhesive properties, and is soluble in carbon disulphide. Asphalt mixtures have been used as road construction materials for thousands of years [5]. Hot Mix Asphalt (HMA) was first recorded to build roads in the United States in the 1860s, which is one of the most widely used pavement materials nowadays [5]. It is a mixture of asphalt binder and graded mineral aggregates, mixed and compacted at elevated temperatures. In the mixture, asphalt is the agent that binds aggregates together, which is usually produced from the fractional distillation of crude oil

[6]. Since asphalt binders are extremely complex in chemical compositions, they are usually classified into two broad chemical groups, i.e., asphaltenes and maltenes. The maltenes can be further subdivided into resins, aromatics and saturates via the SARA separation method provided by the ASTM standards [7]. Asphaltenes are polar and complex aromatic materials of high molecular weight. In the oil phases, the aromatics consist of nonpolar carbon chains in which unsaturated systems dominate; while saturates consist of straight and branch nonpolar hydrocarbons [8]. The resins are molecules in-between comprised of hydrogen, carbon and small amounts of oxygen, sulfur and nitrogen [6, 9]. The asphaltenes and resins could be linked in an open network or dispersed as discrete particles depending on the ratio between asphaltenes and maltenes [8]. Fig.1 shows the representative molecules structures for SARA fractions in the molecular dynamics simulations [10].

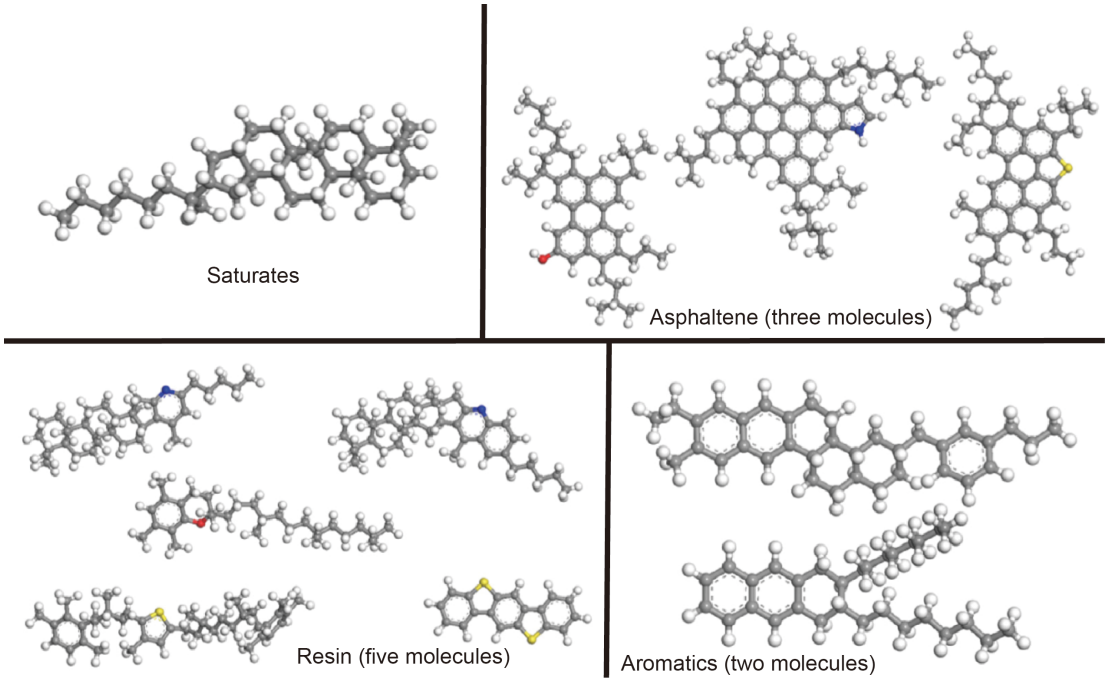

Figure 1: Molecular structures of asphalt SARA fractions (carbon: grey, sulfur: yellow, hydrogen: white, oxygen: red, nitrogen: blue) [204]

Superpave performance grading (PG) is based on the idea that an HMA asphalt binder's properties should be related to the conditions under which it is used. For asphalt binders, the PG standard involves expected climatic conditions as well as aging considerations. Therefore, the PG system uses a common battery of tests (similar to the older penetration and viscosity grading systems), but specifies that a particular asphalt binder must pass these tests at temperatures that are dependent upon the climatic conditions in the area of use. PG grades are reported using two numbers, the first represents the average seven-day maximum pavement temperature (°C) in the service condition, whereas the second represents the minimum pavement design temperature likely to be experienced (°C). For instance, a PG 58-22 is intended for use at locations with the average seven-day maximum pavement temperature is 58°C and the expected minimum pavement temperature is -22°C. Notice that these numbers are pavement temperatures and not air temperatures (these pavement temperatures are estimated from air temperatures using an algorithm contained in the LTPP Bind program). In general, PG binders that differ in the high and low temperature specifications by 90°C or more generally require modifications as shown in Fig. 2 [11].

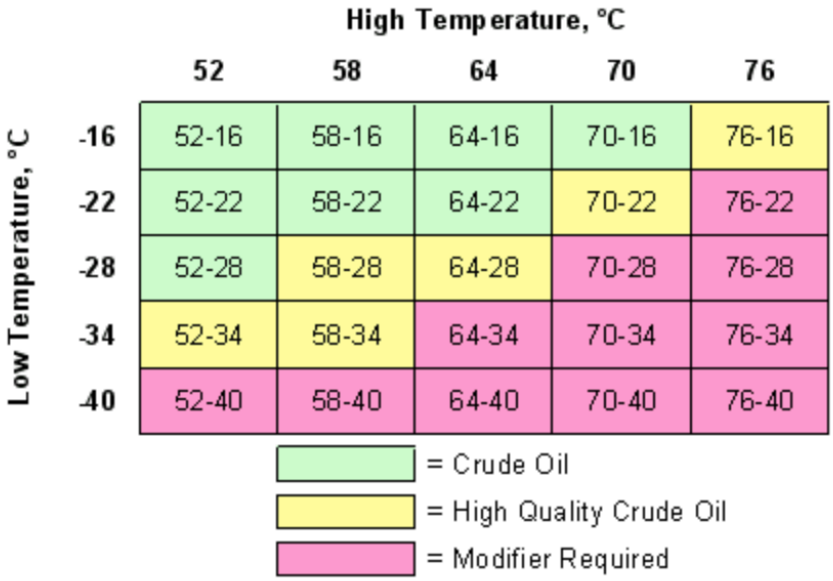

Figure 2: Prediction of PG grades for different crude oil blends [11].

Raw asphalt binders are not suitable for modern roads because of some disadvantages, such as high temperature rutting and low temperature cracking [12]. Therefore, engineers are driven to modify bitumen materials to improve their performance during service. As the traffic demand on pavement materials keeps increasing, the research for hot mix asphalt has been substantial [13]. Asphalt modifiers have been used to optimize durability and rut resistance in HMA and benefited for environment [14]. There are three types of modified methods for asphalt binders, including physical modification, chemical modification and other modifications [15]. Table 1 shows the types of modifiers and additives used in asphalt binders. The most modifiers are common to use in the industry, such as styrene butadiene styrene (SBS), styrene-butadiene-styrene triblock rubber (SBR) and polyphosphoric acid (PPA) [6].

Table 1: The type of physical modifier and additive used in the asphalt binders [6]

Type of Modifier	Type of additive
Thermoplastic Elastomer	Styrene – butadiene – styrene (SBS) Styrene – butadiene – rubber (SBR) Styrene – isoprene – styrene (SIS) Styrene – ethylene – butadiene – styrene (SEBS) Ethylene – propylene – diene terpolymer (EPDM) Isobutene – isoprene copolymer (IIR) Natural rubber Crumb tyre rubber Polybutadine (PBD) Polyisoprene
Thermoplastic Polymer	Ethylene vinyl acetate (EVA) Ethylene methyl acrylate (EMA) Ethylene butyl acrylate (EBA) Atactic polypropylene (APP) Polyethylene (PE) Polypropylene (PP) Polyvinyl Chloride (PVC) Polystyrene (PS)
Thermosetting Polymers	Epoxy Resin Polyurethane Resin Acrylic Resin Phenolic resin

SBS is widely used in modifying asphalt binders because of its relatively good appropriate solubility in asphalt, as well as the relatively excellent properties and acceptable cost of SBS modified bitumen [16]. Elastomeric phases of SBS absorb the oil fractions from the asphalt and swells it, conducting to a continuous polymer phase which is formed throughout the modified asphalt leading to significant change of rheological properties [17].

SBR is produced by the free radical copolymerization of styrene and butadiene in emulsion. The benefit of adding SBS in asphalt binders is to improve the elastic characteristic of asphalt without increasing the stiffness or rigidity of asphalt at low

temperatures [18]. Also, the modified asphalt with SBR increased resistance to rutting and improvement of cracking resistance at low temperatures [19-21].

PPA is being increasingly used as a modifier of asphalt for pavement construction. PPA ($H_{n+2}P_nO_{3n+1}$) is liquid mineral polymer additive of orthophosphoric acid (H_3PO_4) used either by itself or in conjunction with other polymers [22]. The commercial Polyphosphoric acid is a mixture of orthophosphoric acid with pyrophosphoric acid, triphosphoric and higher acids and is on the basis of its calculated content of H_3PO_4 as for example 115%. PPA is commonly used to shift the high temperature PG grade of asphalt to the next higher grade. Adding PPA can increase viscosity without increasing the penetration, and increase the high temperature stiffness of an asphalt binder with only minor effect on the intermediate and low temperature properties. In the last ten years, it has been reported that PPA increases the high temperature performance grade of asphalts with only minimal effect on the low temperature performance grade while mitigating the aging of the asphalt. Despite these perceived benefits, the mechanisms of PPA modified asphalt are not well understood, and the long-term performance effects are not known.

Mineral aggregates are hard, inert materials such as sand, gravel, crushed stone, slag, or rock dust. As the principal load-supporting components of asphalt pavement, the content of aggregates in asphalt are total 90 to 95 percent of the mixture by weight and 75 to 85 percent by volume [23]. When mixed to produce asphalt mixtures, the aggregates are comprised of various fine and coarse solids, primarily limestone (calcium carbonate), granite (72.04 wt.% silica and 14.42 wt.% alumina) and sand (silica) [24]. Thus, the major chemical components of the asphalt mixture aggregates are silica (SiO_2), calcium carbonate ($CaCO_3$) and alumina (Al_2O_3).

1.2 Cementitious materials

The global concrete and cement market valued USD 457.2 billion in 2011, which is expected to exceed USD 921 billion by 2020 [25], growing at a compound annual growth rate of almost 8% [26]. Cementitious material is one of the principal ingredients that make up the concrete mixture including traditional Portland cement and other cementitious materials, such as fly ash, ground granulated blast furnace slag, limestone fines and silica fume.

Portland cement is the most common type of cement used over the world as a basic ingredient of concrete, mortar, stucco, and non-specialty grout. It was developed from other types of hydraulic lime in England in the middle 19th century, and usually originated from limestone. The fine powders are produced by heating limestone and clay minerals in a kiln to form clinker, which are then grind with 2 to 3 percent of gypsum. Ordinary Portland cement (OPC) is the most commonly used cement. Its name is derived from its similarity to Portland stone quarried on the Isle of Portland in Dorset, England [27]. Since the raw materials has low cost and widespread availability, Portland cement is one of the lowest-cost materials widely used over the last century, which leads to the concrete produced one of the most versatile construction materials.

Concrete is strong under compression, but has weak tensile strength. In reinforced concrete, steel bars are used to improve the tensile performance of concrete. Reinforcing bars form meshes of steel wires used as a tension device to strengthen the concrete under tension [28]. The bond between the concrete and rebar refers to the resistance of surrounding concrete against pulling out of steel rebars.

One fundamental assumption of the classic reinforced concrete theory is that perfect bonding exists between concrete and steel rebars. A variety of factors can lead to the failure of bond between concrete and steel, such as mechanical loads [29], corrosion [30, 31] and thermal variations [32]. Substantial efforts have been devoted to study the bond behavior between concrete and steel rebars in the past century [33-55], including interfacial stress distributions [34, 41, 51], bond-slip [35, 36, 42], cyclic loading [38], corrosion [43, 50], crack patterns [48], and elevated temperatures [52]. Significant research has been performed to study the bond behavior between concrete and steel rebars using the pull-out test [33-55], or the pull-off test [44, 45]. The bond strength between steel rebars and concrete depends on adhesion, friction and mechanical interlock [46, 47, 56, 57].

The pull-out test produces a well-defined failure in the concrete and measures a static strength property of concrete. This test method is to determine the pullout strength by measuring the force to pull an embedded metal from a concrete test specimen or structure. There are two ways to insert rebar into concrete, one is casting rebar into fresh concrete, the other is installing rebar into the hardened concrete.

1.3 Motivations and objective

The micro-mechanism is critical to influence the chemical adhesion between bi-materials. For bituminous materials, the properties of the binders, mineral aggregates and their interface play an important part in determining the cracking mechanism of asphalt mixture. There are three types of cracks in the asphalt mixture, that initially grow either within the asphalt binder, at the binder-aggregate interfaces or within the aggregate particle, as shown in Fig. 3.

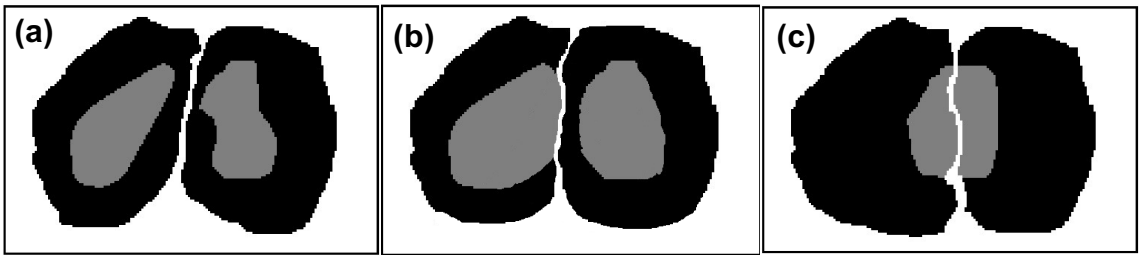

Figure 3**:** A schematic of type of cracks in asphalt mixtures: (a) within the binder; (b) along the binder-aggregate interface; (c) within the aggregates.

More studies have been undertaking on the micro properties between the modified asphalt and mineral aggregates. In this thesis, we aim at studying the adhesion between different modified asphalt binders and the primary aggregate minerals under ambient conditions using the particle probe scanning force microscope at microscale.

For cementitious materials, limited research exists to detail the adhesion between steel and different phases of cement paste at microscale, i.e., a fundamental property that determines the performance of reinforced concrete structures at different service conditions. Lack of such knowledge not only hinders us from further understanding the interactions between steel rebars and cement, but also hinders the development of cement and steel that leads to high-performance reinforced concrete composites and structures. Scanning Force Microscopy (SFM) has been used to study adhesion between the probe and different materials [58], such as between glass and silicon [59, 60], between stainless steel and polymers [61, 62], between ligands and receptors [63, 64]. Conventional SFM probes are pyramids usually made from silicon or silicon nitride that include sharp radius on the order of nanometers [58].

In this thesis, the first research objective of this study is using the particle-modified scanning force microscope probes to quantify adhesion of bituminous and cementitious materials at microscale. For bituminous material, the adhesive force between different asphalt binders and aggregate minerals was measured under ambient conditions. The modified SFM cantilevers by attaching mineral microspheres to the free end, and allowing direct probing between mineral spheres and binder substrates. The modified SFM probes could effectively measure the adhesion differences between binders and aggregate minerals. Our results are consistent with general consensus that SFM techniques characterize the Lifshiz-van der Waals component in adhesion [58].

The second research objective is to study the adhesion between steel and early-hydrated cement at microscale was measured using particle probe scanning force microscopy. The alkaline environment of concrete provides a service condition (pH of 12~13) to rebars [66-69], in which the presence of calcium hydroxide is critical to maintain the high pH values. To simulate the working condition, adhesive forces were collected between steel microspheres and early-hydrated Portland cement paste in saturated limewater (pH≈12.3). As a comparison, adhesive measurements were collected between steel microspheres and cement substrates in air. Conventional SFM probes were also used to perform adhesion tests in corresponding conditions. Then, mixed Gaussian models were used to deconvolute different phases in the cement substrates based on the adhesion measurements. Volume fractions predicted from a stoichiometry-based hydration model were compared with the experimental data on these groups, including low density calcium silicate hydrate, high density calcium silicate hydrate, calcium hydroxide, other hydrated products and the unreacted cement. Finally, adhesive forces between steel microspheres

and different phases were analyzed and determined accordingly. This study focuses on the adhesion induced by intermolecular forces [70] between steel and different hydrated cement phases; while interlocking [71, 72] and frictions are not studied.

CHAPTER 2: LITERATURE REVIEWS

The scanning force microscopy (SFM) is one of the branch of scanning probe microscopy (SPM), which comprises microscopic techniques that relies on the interaction of a physical probe with the substrate. The scanning tunneling microscope (STM), which is the precursor of SFM, was developed by Gerd Binnig and Heinrich Rohrer in the early 1980s [73, 74], and earned the Nobel Prize for Physics in 1986. The first SFM was invented by Binnig, Quate and Gerber in 1986 [75]. The alternative name, atomic force microscopy (AFM), refers to the interactions between probe and substrate on the atomic level. The attractive van-der-Waals forces and the Pauli repulsion due to overlapping electron orbitals can be described by the Lennard-Jones potential [76]. SFM covers a variety of microscopic techniques to measure interactions between probes and substrates. Depending on the condition, forces that are measured in SFM include mechanical contact force, electrostatic forces, magnetic forces, etc. [61-64, 77].

2.1 Scanning force microscope in bituminous materials

The performance of asphalt mixtures is highly dependent on the properties of binders, aggregates and their interfaces. The major distress of asphalt mixtures is cracking, that can occur either within asphalt binders, at the binder-aggregate interfaces or within aggregate particles. Recently, scanning force microscope (SFM) has been used to investigate the properties of asphalt materials. The use of SFM has the potential to single out microscopic features of different phases in asphalt binders, allowing future improvements of both asphalt processing and the modeling of asphalt mixture cracking.

2.1.1 Microstructural characterization

Asphalt binders are complicated mixtures of organic molecules of different sizes and polarities for which the micro-structures are difficult to quantify precisely. SFM has been used to characterize morphologies and chemical compositions of different plain and modified binders. Loeber et al. [78] combined the atomic force microscopy (AFM) and scanning electron microscopy (SEM) to study the microstructures of asphalt binders, and used fluorescence microscopy to understand the structural changes when polymers are added. Their study revealed a network of asphaltene molecules related to asphalt gel, which was confirmed by the high resolution SEM results. They observed a rearrangement of the initial asphaltene which leads to the assumption that polymer can aggregate the asphaltene phase. Jäger et al. [79] identified the four different phases of asphalt binders at the bitumen-scale using atomic force microscopy, which are related to the chemical compositions of bitumen, characterized by a wide range of molecular mass. According to the multi-scale model, the properties of these phases provided material parameters of the bitumen phase at the mastic-scale.

Masson et al. [80] classified the asphalt binders into three distinct groups based on the phase morphologies. One group showed fine domains down to 0.1 μm, another showed domains of about 1 μm, and a third group showed up to four different domains of different sizes and shapes. A high correlation was found between the area of the 'bee-like' structures and the vanadium and nickel contents in bitumen, and between the groups and the average size of molecular planes of aromatics. Schmets et al. [81] used atomic force microscopy and neutron scattering techniques to confirm the appearance of wax-induced phase

separations, which were related to the cracking and healing potential of asphalt binders. They found the effects of wax on bitumen quality and asphalt mixture performance depended on chemical compositions of the bitumen and particularly the nature of the wax.

Pauli et al. [82] studied the morphologies and chromatographic fractions of asphalt binders using AFM, which show that a variety of 'microstructures' of these materials. Also, they found that microstructures develop to different degrees and forms depending on the residual crude sources from which the asphalt or asphalt fraction are derived, the thermal history of the sample and the sample thickness. They hypothesized that the interactions between crystalizing paraffin waxes and the remaining asphalt fractions are responsible for the microstructures, including the well-known bee structures observed within asphalt materials. Zhang et al. [83] studied the morphologies of unmodified and organo-montmorillonite modified asphalt binders by atomic force microscopy, and investigated the effect of thermal and ultraviolet aging on the morphology of the binders. The results showed the dimensions of the 'bee-like' structures decreased with the introduction of organo-montmorillonite. The organo-montmorillonite modified bitumen exhibited good aging resistance, and the single-phase trend could be effectively prevented during thin film oven tests and ultraviolet aging. Lyne et al. [84] used AFM technique to investigate microphase-separated morphologies and the relationship to local mechanical properties of unaged grade 70/100 bitumen binders. The results showed that the adhesive forces measured in the region surrounding (peri phase) the periodic topographic features resembling 'bees' (catana phase) and the region in the 'bee' areas were lower than the adhesive force measured in the smooth matrix (para phase).

Microstructures of asphalt binders are highly dependent on temperature [85-89]. De Moraes et al. [85] studied the microstructures of asphalt binders using thermal phase detection atomic force microscopy. According to the phase and topography images, the 'bee structure' changed considerably at temperatures between 50°C and 56°C, and completely disappeared at temperatures above 57°C. Das et al. [86] used atomic force microscopy to investigate the phase separation behavior at different temperatures for various asphalt binders, and co-relate them to the differential scanning calorimetry measurements. The results showed that the observed phase separation is mainly due to the presence of wax/paraffin fraction in asphalt binders. Nahar et al. [87] investigated the influence of temperature and thermal history on the microstructures of bitumen. The microstructural features of asphalt binders showed a tendency to align themselves with increasing temperature and possessed a 'memory' for its maximum processing temperature.

Soenen et al. [88] combined differential scanning calorimetry (DSC) and atomic force microscopy to analyze the influence of wax on different phases. Their result showed that the "bee" structure disappeared around the melting peak of the DSC curve. Gong et al. [89] investigated the physical and chemical properties of bio-oil rejuvenated asphalt with a series of tests, including conventional tests (penetration, softening point, and ductility), rheological properties (viscosity, high-temperature rutting resistance, and low-temperature cracking resistance) and micro testing techniques. Results clearly demonstrated that bio-oil could soften aged asphalt and improved the low-temperature cracking resistance.

Xu et al. [90] studied the effect of heat, ultraviolet radiation and moisture on the surface structure in aging process of different asphalt using SFM. The results show that

two characteristic regions appear at the surface of samples after aging. Wang et al. [91] used SFM to study the effect of different preparation methods on phases of asphalts, including the solvent method, the alcohol lamp method, and the oven method. Results indicate that the oven method was recommended due to the least effect on the materials structure and chemical property. The solvent method may partial damage the structure of asphalt binder, and the alcohol lamp method burned sample with a flame for the preparation, which is not easy to control and repeat.

2.1.2 Mechanical properties

In asphalt pavements, the adhesion between aggregates and asphalt binders directly affects how roads respond to traffic loads. Different polymers have been added to binders to improve the performance of HMA admixtures [14], such as the styrene-butadiene-styrene triblock rubber (SBR), styrene butadiene styrene (SBS) and polyphosphoric acid (PPA) [6]. Recently, there is an intense discussion on the use of Re-refined Engine Oil Bottoms (REOB) in pavements [92, 93], whose complicated chemical constituents have raised substantial concerns in the asphalt area. There is a strong need for a method to determine the adhesion between binders and aggregates, i.e., the stickiness of aggregates and binders, through which the role of chemical constituents in binders could be accurately quantified. Therefore, there is a growing interest to study mechanical properties of modified asphalt materials using scanning force microscopes.

First, SFM has also been used to measure the adhesion between silicon or silicon-nitride AFM tips and binder substrates [83, 94-96], or the cohesion between functionalized AFM pyramids (carboxyl, methyl and hydroxyl coated tips) and binder substrates [94, 95,

97]. Tarefder and Zaman [94] measured adhesion between bare silicon nitride SFM tips and styrene-butadiene (SB) and styrene-butadiene-styrene (SBS) modified asphalts binders, as well as the cohesion between functionalized SFM tips (carboxyl (-COOH), methyl (-CH3), and hydroxyl (-OH)) and modified asphalt binders. Nazzal et al. [95] studied the nanostructure and microstructure of the modified warm mix asphalt (WMA) material with Advera, Evotherm, and Sasobit by AFM tapping-mode imaging technique, adhesive and cohesive forces between chemically functionalized AFM tips and asphalt binders using AFM force spectroscopy. The result showed that WMA additives significantly increased the adhesive forces prior to moisture conditioning and only Sasobit has significant effect on the adhesive forces after moisture conditioning, and also Sasobit and Advera can reduce the nanoscale cohesive forces within the considered asphalt binders upon moisture conditioning. Allen et al. [98] successfully performed indentation tests using silicon SFM probes to evaluate the microrheological properties among different binder phases and the atomic force microscopy to semi-quantitatively evaluates the micro-rheological properties of asphalt binder and presented differences between these properties amongst the various microstructures within asphalt binders, in addition to the influence of oxidative aging on these properties. By using silicon nitride SFM probes, Furthermore, Yu et al. [97] investigated the effects of compressive forces and scan speed in measuring adhesive forces between silicon tips and binders. Arifuzzaman et al. [99] studied the moisture damage relation in lime and SBS modified asphalts, base asphalt binders showed larger adhesion/cohesion values compared to the SBS modified asphalt under dry conditions, while the trend is opposite under wet conditions. Yao et al. [100] used conventional SFM probes and nano-indentation to capture the micromechanical properties

of asphalt and mixture samples before and after moisture damages and compared the experimental results with the results from surface energy method and freeze-thaw splitting test. Gong et al. [101] investigated the mechanism of asphalt property changes during water immersion using SFM and Fourier transform infrared spectroscopy (FTIR). The SFM mechanical results show reasonable connections to FTIR results which indicates that polar components tend to interact with polar water molecules. These studies have created an innovative niche to examine interactions between aggregates and binders at the nanoscale. However, nanonewton forces measured using AFM tips with nanoscale radii cannot be directly used in microcracking models of asphalt mixtures [102-107].

Second, AFM techniques have been used to measure the adhesion between asphalt binders and mineral surfaces. By aging mica and silica substrates in solutions containing the crude oil or its SARA fractions [7], Kumar et al. [108] measured the adhesion between a carboxylic-terminated borosilicate tip and these substrates in the presence of water to understand the nature of mineral surfaces treated with the whole oil or one of its SARA (saturates, aromatics, resins, and asphaltenes) fractions. Fischer et al. [109] used silicon probes to characterize the wetting angles between an asphalt binder films and several minerals (marble, calcite, mica and quartz). No significant differences in the wetting capabilities were detected between the binder and different minerals. But the catana/peri-phases (‘Bee structures’ in asphalt binders) exhibited higher adhesion to the substrates than the para-phase. By attaching silica particles to the SFM probes. Hogshead et al. [110] measured the bitumen-silica adhesion in ionic liquids. The results showed that the adhesion between bitumen samples obtained from both Canadian and U.S. oil sands are approximately an order of magnitude smaller in an ionic liquid medium than in aqueous

solution. Meanwhile, Al-Rawashdeh and Sargand [107] performed SFM tests to measure the adhesion between silica/calcium carbonate particles and three asphalt binders, and cohesion between carboxylic acid functionalized silica particles and these binders. The binders used in the study included a control PG 70-22 binder and two modifications produced by adding Sasobit and Advera, respectively.

Meanwhile, statistical analyses have been used to investigate different factors on the mechanical performance of asphalt mixtures [111-115]. Liu et al. [113] performed the variance analysis to study different factors on the performance of crumb rubber modified asphalt mixtures, including crumb rubber types, weight ratios, and particle sizes. Mangiafico et al. [114] evaluated the influence of several mix factors on the mechanical performance of reclaimed asphalt pavements, such as aggregates, fillers, binder types and binder contents. Moghaddam et al. [115] statistically evaluated the effects of applied stresses and temperatures on the stiffness modulus of asphalt mixtures made from plain and polyethylene terephthalate modified binders.

In most of these studies, bare or coated bare atomic force microscope tips made from silicon or silicon nitride were used to measure the adhesion, for which the radii are up to several dozen nanometers [116]. More effort is still needed to correlate these nanoscale measurements to cracking behavior described in asphalt mixtures models at micrometer scales [103, 104]. Meanwhile, it is critical to directly quantify adhesion between binders and the primary aggregates minerals. Therefore, direct quantification of adhesion between the primary aggregate constituents (SiO_2, $CaCO_3$ and Al_2O_3) and binders is needed since these findings are crucial to engineering applications of asphalt materials.

2.2 Scanning force microscope in cementitious materials

The primary bonding strength between steel and concrete results from the adhesion, the frictional resistance, and the interlocking between concrete and rebars [117, 118]. A transitional region exists near the steel surface, where the cement density is less than the bulk [119-121]. Results showed an enrichment of calcium hydroxide occurs in the cement-steel interface [121-123]. A comprehensive review has summarized the local properties of the steel-concrete interface [121]. The adhesion between steel and cement is crucial because this fundamental property significantly influences the theory and practice of reinforced concrete structures. Substantial research has been devoted to this topic since the early twentieth century [124-130]. Here, a brief literature review is performed on the experimental methods evaluating the steel-cement bonding in prior studies. Pullout test [131, 132] have been widely used to measure the bond strength between steel rebar and different cement pastes, in which a cylindrical steel bar is pulled out from the surrounding cement matrix. Chapman and Shah [133] showed that the pullout bond strength between smooth bars and concrete did not vary substantially from 1 to 28 days of curing. Fu and Chung [134-136] conducted pull-out tests to evaluate the effects of water-cement ratios, curing ages, polymer admixtures and steel surface treatments on the bond strength between concrete and steel. Pullout tests have been performed to evaluate the bond strength between steel and high-strength concrete [137-140], lightweight concrete [141], recycled concrete [142, 143], self-compacting concrete [144]. Enamel coated steel and concrete exhibited higher pull-out strength than ordinary steel [145]. Another experiment used to measure the steel-cement adhesion is the pull-off test [146-149]. Steel and cement bulks are bonded over a flat surface, and tensile force is applied to pull them away from each other. Khalaf

and Page [146, 147] performed pull-off tests to measure the bond strength between steel and cement mortars with various mixes and surface properties. Similar methods have been used by Montgomery and Samarin [148] to study the bond strength between treated and untreated metal surfaces and cement. In addition to the two mechanical tests aforementioned, Zhang et al. [150] used the Brazilian nut disks to evaluate the bonding between steel and cement/mud system. Electrochemical tests [151, 152] have also been used to evaluate the adhesion between steel and cement. To reveal the role of steel-motar adhesion in corrosion resistance, Axelsson et al. [151] performed the macrocell tests to measure the corrosion rates of the steel-mortar specimens with and without wrapped filter papers. The results showed that steel specimens covered with filter papers exhibited three times the corrosion rate of those without filter papers, meaning that a good mortar-steel adhesion help preventing the steel corrosion. Despite these efforts, limited research exists to quantify adhesion between steel and different hydrated cement phases, or to evaluate the steel-cement adhesion at microscale in different chemical and thermal conditions. Lack of such knowledge hinders us from further understanding the steel-cement interface, and creating high performance cements and steels.

The idea of scanning force microscopy originates from the interactions between the probe on the free end of a microcantilever and the substrates, through which different material properties can be characterized [58, 62, 64]. As surface sciences merge with concrete research [153, 154], SFM has been applied to measure adhesion between a commercial silicon nitride probe and cementitious materials [155]. Conventional SFM probes are pyramids with nanoscale radii, which are designed to characterize nanoscale features of the substrates. The materials of these probes are usually silicon or silicon nitride

[58]. Therefore, the measurements can hardly represent the adhesive forces between steel and cement. In the meantime, it may not be easy to incorporate these nanoscale measurements into to the engineering analysis. Recently, particle probes [156-160] have been used to measure adhesion between aggregate minerals and asphalt binders. The results successfully demonstrated the differences of adhesion between asphalt binders and the primary aggregate minerals, such as calcium carbonate, silica and alumina [156-159]. If particle probes are fabricated using steel microspheres, the adhesive forces between steel and cement substrates can be measured accordingly.

CHAPTER 3: ADHESION BETWEEN ASPHALT BINDERS AND AGGREGATES

In this chapter, we studied of the adhesion between different asphalt binders and the primary aggregate minerals under ambient conditions using the SFM method. We modified the SFM cantilevers by attaching microspheres to the free end of the cantilever, and allowing direct interaction between the spherical particles and the binder substrates.

3.1 Materials

3.1.1 Plain asphalt binders

The plain asphalt binder substrates were prepared using five different binders, including PG 58-22, PG 64-22, PG 70-22 PG 64-16, and PG 64-28 provided by the SHRP's Materials Reference Library (MRL, Austin, TX). PG 64-22 is a widely used binder, and detail characterization has been included in ASTM standards [7]. Binders with the same minimum pavement design temperature but different maximum pavement temperature (PG 58-22, PG 70-22) were selected for comparison. Similarly, binders with the same maximum pavement design temperature but different minimum pavement temperature (PG 64-16, PG64-28) were also selected.

3.1.2 Modified asphalt binders

PG 64-22 and PG 58-22 provided were used as control binders in this study. Three types of modifiers, including SBS, SBR and PPA, were added to control binders at the weight percentages of 2 and 4% to prepare modified binders. To prepare PPA modified specimens, PPA (ICL Performance, St. Lousi, MO) was added into heated control binders

at 120˚C and mixed for 30~45 minutes. Then, the modifications were heated up to ~160˚C for 30 minutes before substrates were prepared [161]. For SBR modifications, SBR (Ultrapave, Dalton, GA) was added to heated control binders at ~165˚C and mixed for 2 hours. For SBS modifications, SBS (Bitumar, QC, Canada) was added to heated control binders at ~175˚C and mixed for 2 hours.

3.1.3 Aggregate mineral particles

Three types of spherical mineral microspheres, including the silica, alumina (Microspheres-Nanospheres Inc., Cold Spring, NY) and calcium carbonate (PlasmaChem Inc., Berlin, Germany), were used for tip attachment. For each type of particle, the mean value of the spherical diameters was ~6 μm.

3.1.4 Substrate specimen preparation

The thin film binder substrates were prepared based on the following procedure. Initially, the binders stored in a 5-oz tin were stirred using a stirring rod for 5 minutes. Then, a small amount of the binder was transferred onto a wafer of an area of 5 x 5 mm2. The material was gradually heated to 163˚C (325˚F) using a Model 11-300-49SHP ceramic hotplate (Thermo Fisher Scientific Inc., Waltham, MA), and a stainless steel spatula was used to spread the asphalt binder on the wafer in ~ 5 minutes. The heated temperature allowed smooth coverage of the binder over the wafer surface. All asphalt binder specimens were then cooled to the ambient temperature, and stored in an oven at 30˚C overnight before adhesion measurements.

3.2 Methods

3.2.1 Scanning force microscope (SFM)

SFM has been used to measure the adhesion between different materials [58, 61-64]. Fig. 4 shows the actual SFM systems we used. Fig. 4(a) is the Nanoscope SFM equipped with a Nanoscope IIIA controller and a J-scanner, we use it for adhesion measurement. Fig. 4(b) shows the asylum MFP-3D-BIO atomic force microscope station, which was used with commercial SFM probes to characterize the substrates and calibrate the spring constant of particle modified probes.

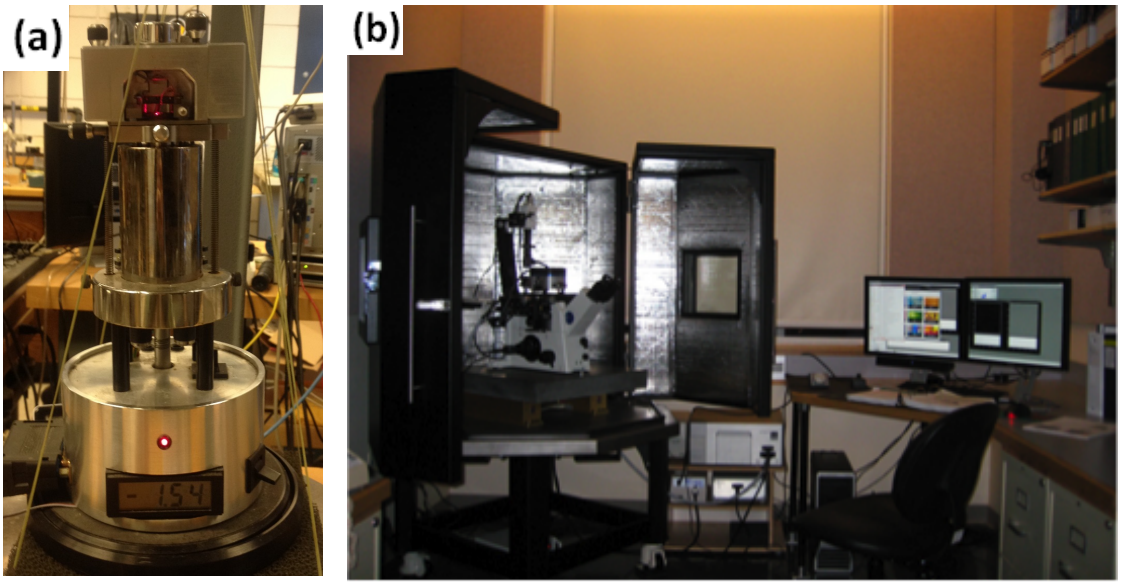

Figure 4: (a) Nanoscope SFM equipped with a Nanoscope IIIA controller and a J-scanner; (b) Asylum MFP-3D-BIO scanning force microscope station

The main principle of SFM as a force probe is shown in Fig. 5. It uses the reflection of laser light for signal sensing. The cantilever with a tip, which is replaced by a microsphere in this study, serves as the lever arm of the force probe to interact with the substrate surface.

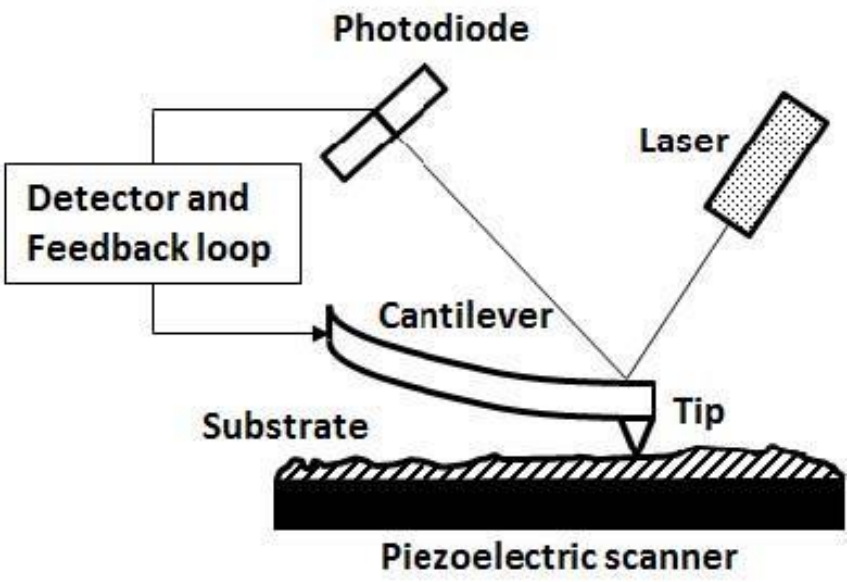

Figure 5**:** A schematic of the Scanning Force Microscopy working principle.

Fig.6 shows a representative force curve collected using SFM. The x-axis is the piezo movement in nm, and y-axis is the PSPD (position-sensitive photo diode) signal. The red line is for approaching as the direction from left to right, and the blue line is for retracting that it goes from right to left. As the tip approaches the surface, the close-range, attractive force between the surface and the tip causes the cantilever to bend towards the surface. However, as the cantilever is brought even closer to the surface, such that the tip makes contact with it, increasingly repulsive force takes over and causes the cantilever to bend away from the surface.

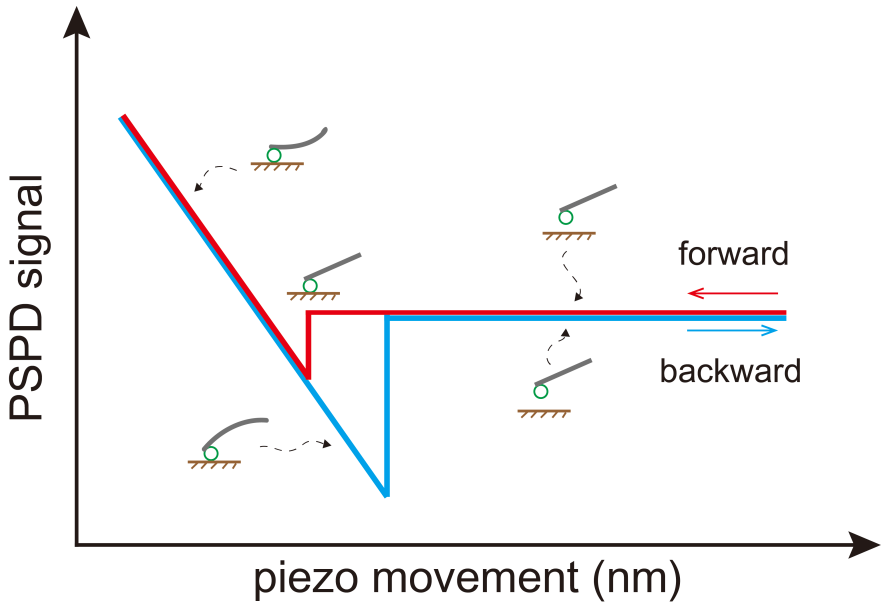

Figure 6: A representative force curve collected using SFM

For force probing, the tip and sample distance is driven to raster [64, 162] and the deflection of the cantilever is used to measure the adhesion force between them. The adhesion is obtained by Hooke's law, which gives

$$F = k\Delta x \tag{1}$$

where k is the spring constant of the cantilever and Δx is the distance between tip-sample contact and the snap-off point.

3.2.2 Development of the particle-modified SFM probes

Particle-modified SFM probes were used to measure the aggregate-binder adhesion by creating direct interaction between the spherical mineral particles and the binder substrates. Cantilevers were NSG11 probes (NT-MDT Inc., Limerick, Ireland), which are

straight rectangles to facilitate the particle attachment. Typical spring constants of plain NSG11 probes are in the range of 2.5 to 10 N/m. Spring constants for those used in adhesion measurements were later determined individually by the thermal tuning method [163, 164].

The attachment of microspheres was achieved by precisely positioning the SFM cantilevers to mineral particles with the help of high resolution optical microscope (Eclipse TS 100, Nikon) and 3D manipulation stages (Ser. NO. 5957, AD-100, Newport) as shown in Fig. 7. Spheres were first spread onto a glass slide and a layer of epoxy (EP 1290, Ellsworth Adhesives) was also created. A plain cantilever was manipulated to touch the epoxy, staying for 10 seconds to ensure epoxy picking up. This epoxy-wet tip was then brought to a particle from which no other spheres were nearby. The movement of the tip to the chosen particle must be extremely slow and the final particle attachment was completed as seen with the optical microscope. After that, the probe was allowed to stay in air for 24 hours to let the epoxy cure. In this study, particles used were silica, alumina and calcium carbonate microspheres.

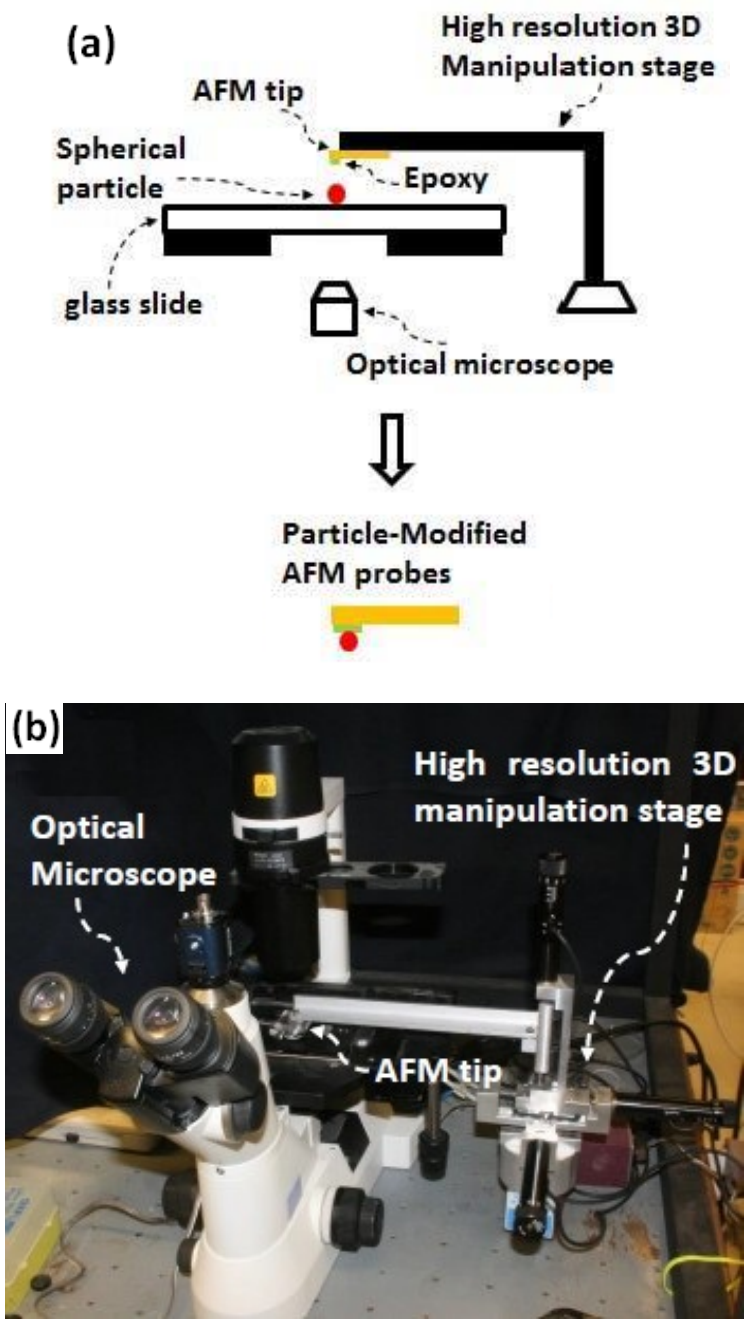

Figure 7: (a) Schematics of the system used to attach the particle to the SFM tip; (b) Image of the actual system.

3.2.3 Determination of the cantilever spring constants

The spring constants of the particle-modified SFM probes were important to the adhesion calculations. In this study, the spring constants were measured using the thermal tuning method [163, 164] in Asylum MFP-3D-BIO scanning force microscope station.

This method relates the measured thermal noise in the SFM cantilever deflection signal to the spring constant using the equipartition theorem [163, 165]. The actual procedures consisted of calibrating the coupling between the deflection signal and the free end movement, measuring the inverse optical lever sensitivity and performing a thermal tune. SFM hardware measures the cantilever's fluctuations as a function of time, and from the time domain measurement, it extracts the frequency spectrum of the cantilever's mechanical response (proportional to the power spectral density, PSD). After that, the spring constants of the particle-modified SFM cantilevers were obtained by an algorithms based on the equipartition theorem [163].

There are three steps to determining the spring constant using Asylum MFP-3D-BIO AFM [166]. First, correcting for virtual deflection effects in the SFM hardware. The virtual deflection is a mechanical coupling of the deflection signal with the Z movement seen on MFP-3D-BIO AFM. Secondly, calibrating the relationship between cantilever deflection (measured in volts) and vertical cantilever motion, which called InvOLS (Inverse Optical Lever Sensitivity) and is measured in nm/V. InvOLS is the slope of contact region, and a parameter necessary for the spring constant algorithm. At last, withdrawing tip and performing a thermal to determine the cantilever's resonant frequency. Fig. 8 shows a representative power spectrum for silicon cantilever. An algorithm computes the spring

constant using the equipartition theorem. By fitting the frequency spectrum to a Lorentzian line shape, the AFM software arrives at an estimate of the cantilever's spring constant.

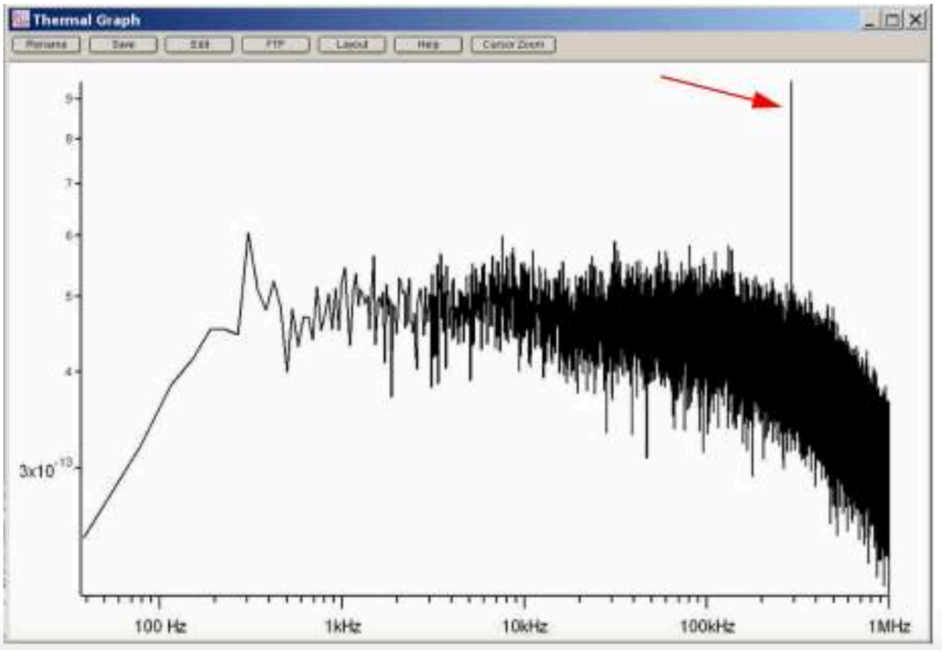

Figure 8: A representative power spectrum for silicon cantilever. The red arrow points to the fundamental resonant frequency of cantilever [166].

3.2.4 Design of Experiment

For plain binders, adhesion measurements were studied based on particle types (silica, alumina, and calcium carbonate), low temperature performance grade (PG 58-22, PG 64-22 and PG 70-22) and high temperature performance grade (PG 64-16, PG 64-22 and PG 64-28). For modified binders, the PG 64-22 was used as the control binder, to which 0, 2 and 4 wt. % SBS, SBR and PPA were added for modifications

Table 2: The design of experiment table.

	Low temperatures performance grade (PG xx-22 binders)			High temperatures performance grade (PG 64-xx binders)		
Particle	**PG 58-22**	**PG 64-22**	**PG 70-22**	**PG 64-16**	**PG 64-22**	**PG 64-28**
$CaCO_3$	×	×	×	×	×	×
Al_2O_3	×	×	×	×	×	×
SiO_2	×	×	×	×	×	×
	Modified Binders					
	PG64-22+ 2, 4 wt.% SBS		**PG64-22 + 2, 4 wt.% PPA**		**PG64-22+2, 4 wt.% SBR**	
$CaCO_3$	×	×	×	×	×	×
Al_2O_3	×	×	×	×	×	×
SiO_2	×	×	×	×	×	×

In this study, a nanoscope E Atomic Force Microscope (Bruker Inc., Santa Barbara, CA) was used. Three types of modified SFM probes were fabricated to characterize the adhesion in related pairs, i.e., the silica-binder, the calcium carbonate-binder and the alumina-binder pair. In the data sets, ten curves were collected at each location on the same substrate, and three locations were selected in total, i.e., thirty measurements between a tip and a substrate. For each particle-binder pair, repetitive data sets were collected using two particle-modified SFM probes and three binder substrate replicas. Therefore, 180 adhesion measurements were collected for each particle-binder pair. Data collections in this study were performed at 25.7˚C and 30% relative humidity. To characterize the binder microstructures, an Asylum MFP-3D-BIO scanning force microscope was used with commercial probes (NanoAndMore USA Corp., Watsonville, CA) in AC mode at the frequency of ~300 kHz.

3.2.5 Parametric distribution fitting

Parametric Distribution fitting is the procedure of selecting a probability distribution to a series of data obtained from repeated measurements of a variable. The aim

of distribution fitting is to predict the probability of occurrence in a certain interval [167], which is given by

$$F(t) = \int_0^t f(u)du \tag{2}$$

Where *F(t)* is probability density function, and *f(t)* is the cumulative distribution function [168]. In this study, four different distributions were performed to fit measurements of the separation distance, including normal, lognormal, Weibull and exponential distributions.

3.2.6 Least squares method

Least squares method is to estimate a quantity to minimize the sum of the squares of the differences between the observed and the estimated values [169, 170]. In the study, the least squares fitting was used to evaluate adhesion, i.e., average surface energy per unit area, using function f (x, β) by:

$$S = \sum_{i=0}^{n} r_i^2 \tag{3}$$

$$r_i = y_i - f(x_i, \beta) \tag{4}$$

Where S is the sum of the squared residuals, r is the set of residuals as the difference between the observed and the estimated values, y is the set of observed values, and β is the set of model coefficients [171].

3.3 Results and discussion

3.3.1 Particle-modified probes

Modified probes was imaged with a scanning electronic microscope (JEOL JSM 6060 USA, Peabody, MA). Figs 9a to 9c showed three representative modified SFM probes with attached silica, alumina and calcium carbonate particles, respectively. Because attaching particle changes the spring constant of particle probe, the spring constant of each particle probe we used in different binder-aggregates pairs was calibrated individually. Table 3 summarized the results of measured spring constants of particle-modified probes, with values ranging from 1.03 to 5.65 N/m. Table 4 showed the values of the particle diameters ranging from 5.15 to 13.03 μm.

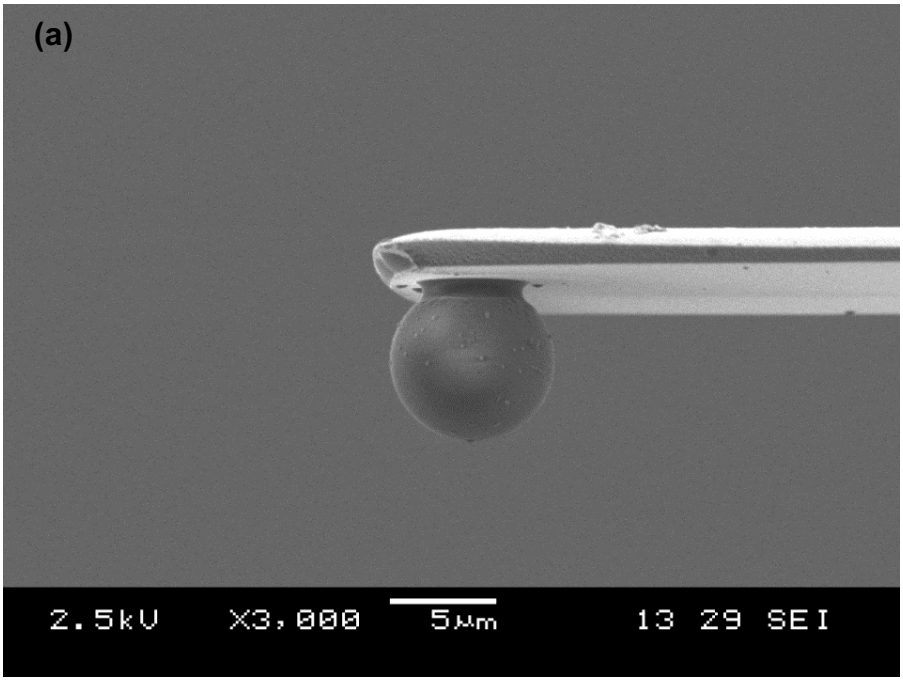

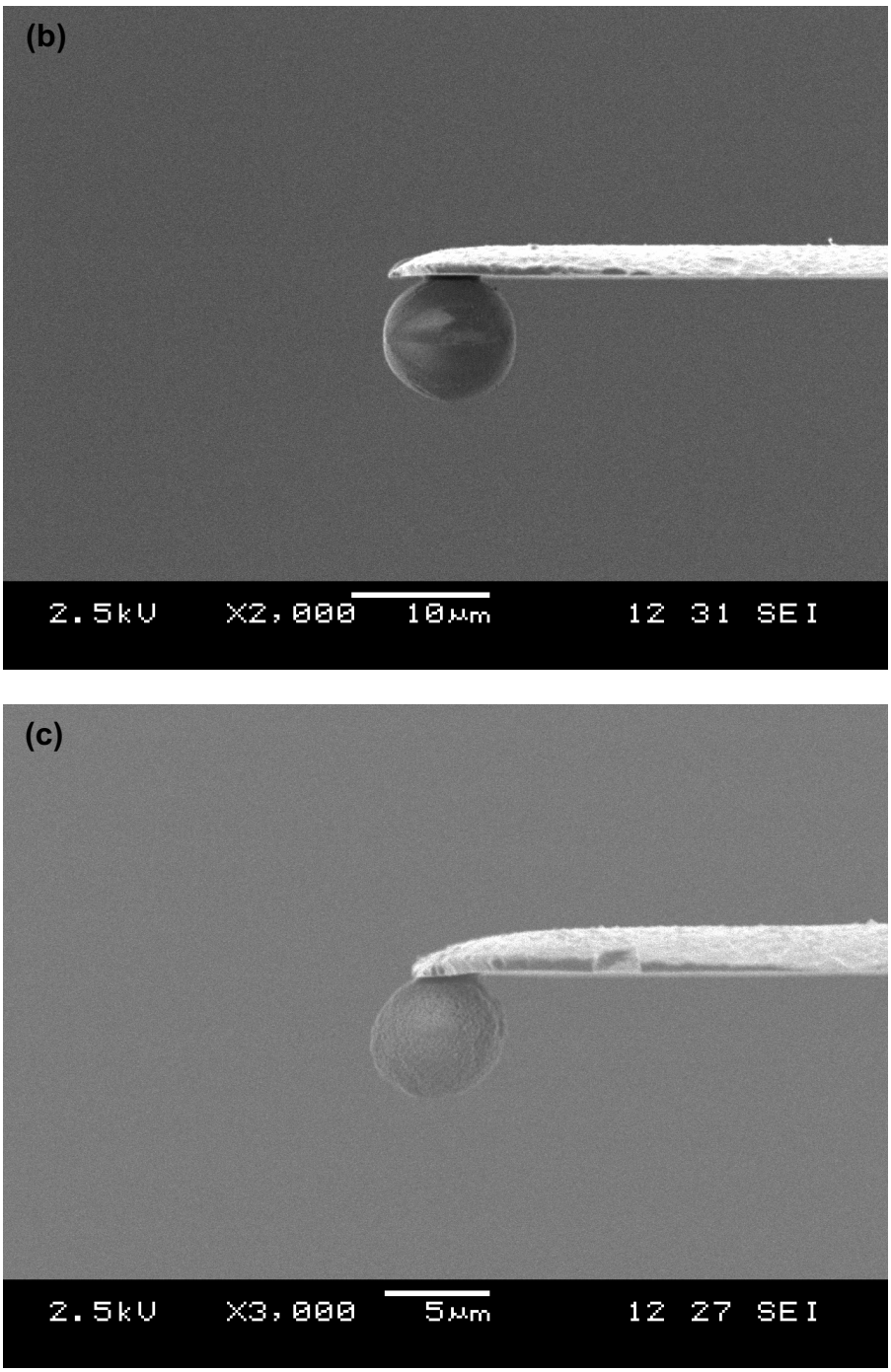

Figure 9: SEM images of particle-modified cantilevers, including (a) a silica particle; (b) an alumina particle; (c) a calcium carbonate particle.

Table 3: Spring constant (N/m) of the particle-modified probes

Binder substrates	Al_2O_3		SiO_2		$CaCO_3$	
	Particle 1	Particle 2	Particle 1	Particle 2	Particle 1	Particle 2
PG 64-16	3.02	4.31	4.65	3.55	1.50	3.86
PG 64-22	2.22	3.36	5.58	5.01	5.44	5.12
PG 64-28	2.30	5.24	2.30	2.67	3.29	3.96
PG 58-22	4.11	5.65	3.83	3.11	3.65	1.84
PG 70-22	3.07	1.83	4.35	1.6	2.62	1.64
PG 64-22+2%PPA	3.25	2.81	2.91	2.83	2.8	1.03
PG 64-22+4%PPA	2.65	3.07	2.04	3.38	1.59	1.43

Table 4: Diameters (μm) of the particle-modified probes

Binder substrates	Al_2O_3		SiO_2		$CaCO_3$	
	Particle 1	Particle 2	Particle 1	Particle 2	Particle 1	Particle 2
PG 64-16	6.34	7.44	9.13	7.98	8.58	6.59
PG 64-22	7.69	8.33	8.26	6.96	7.74	10.13
PG 64-28	7.36	8.52	7.84	7.72	8.43	9.63
PG 58-22	13.03	10.42	7.98	7.85	8.09	6.85
PG 70-22	10.82	8.20	7.43	6.08	6.93	5.15
PG 64-22+2%PPA	7.64	7.32	10.06	8.47	7.22	8.18
PG 64-22+4%PPA	7.26	7.95	7.09	7.28	7.91	6.94

3.3.2 Cement paste substrates

The surface morphology of the asphalt binders is characterized using Tapping Mode by conventional SFM probes. A representative surface of PG 58-22 asphalt binder substrate of 70μm × 70μm is shown in Figure 10. The root mean square (RMS) of the substrate surface roughness was ~20 nm. Therefore, the surface is smooth enough to enable good contact between the microspheres and the asphalt binder substrates at microscale.

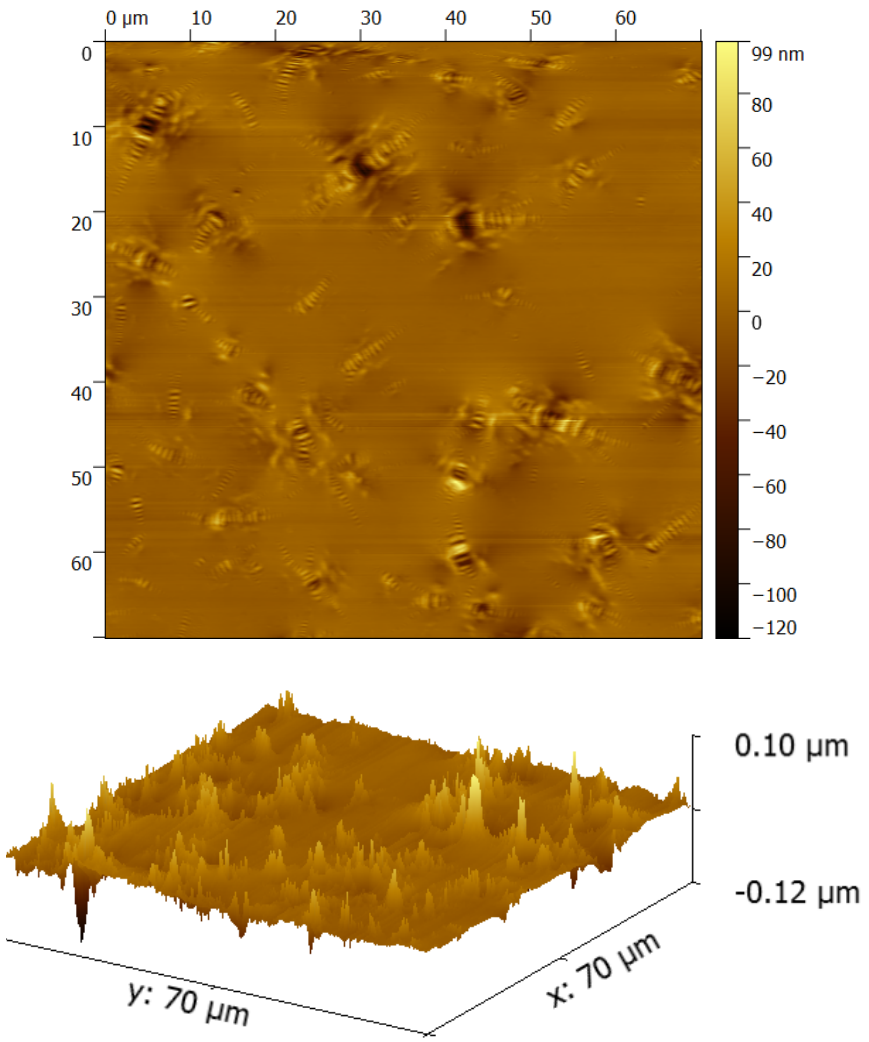

Figure 10: A representative surface of PG 58-22 asphalt binder substrate (scan size: 70 x 70 μm^2).

3.3.3 Cantilever deflection-Z position curves for adhesion measurements

The cantilever deflection-Z position curves in the SFM experiments were essential to the adhesion measurement. Fig.11 showed three representative deflection-Z position curves. Typically, a graph consisted of two curves, one for approaching as the tip was moving toward the sample surface, and the other one for retracting as the tip was moving away from the surface. When the tip was not in contact with the sample on approaching,

the detector signal was constant. After the contact, the signal increased linearly as the sample continued to push the tip. On retracting, the cantilever bending reduced so the signal decreased with the same slope, as expected. However, the tip did not disengage from the surface at the contact point. The adhesion between the tip and the sample made the tip to bend in the opposite direction. When the restoring force of the cantilever was large enough to overcome the adhesion, the tip snapped off the surface and the detector signal became constant again. The flat part at top left of these curves (Figs 11a to 11c) was instrumental, where the deflection signal was out of the range of the recording scope. Similarly, the lower flat part in Figs. 11b and 11c were due to the instrumental range limit on tip retracting. This would not affect the measurement of the adhesion force because the Z-position of the tip relative to the sample surface was still well within the range of the piezo scanner in the SFM core unit.

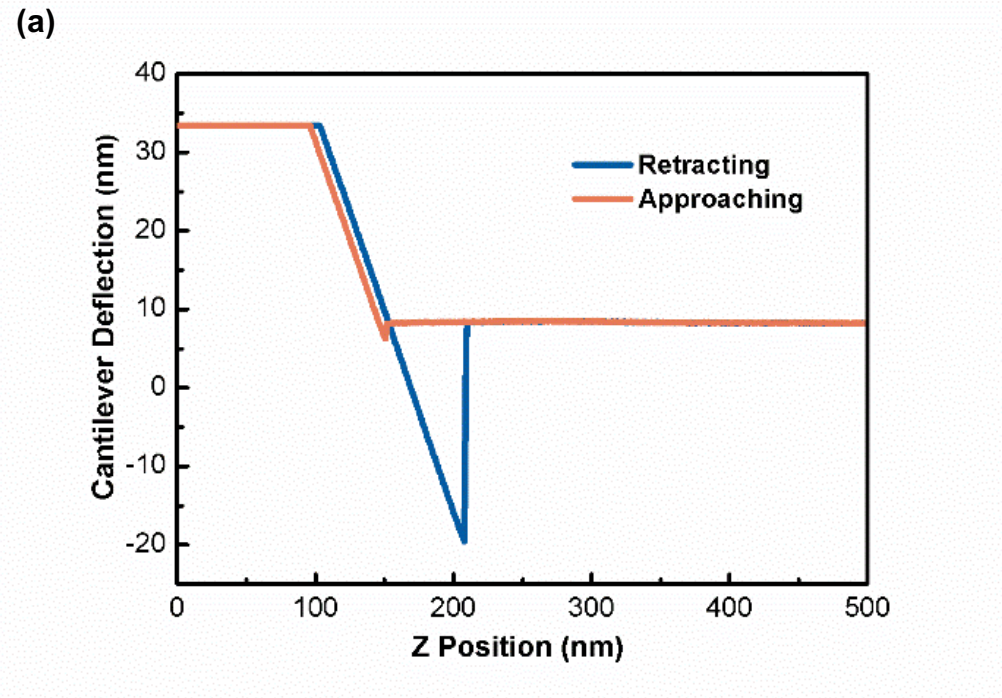

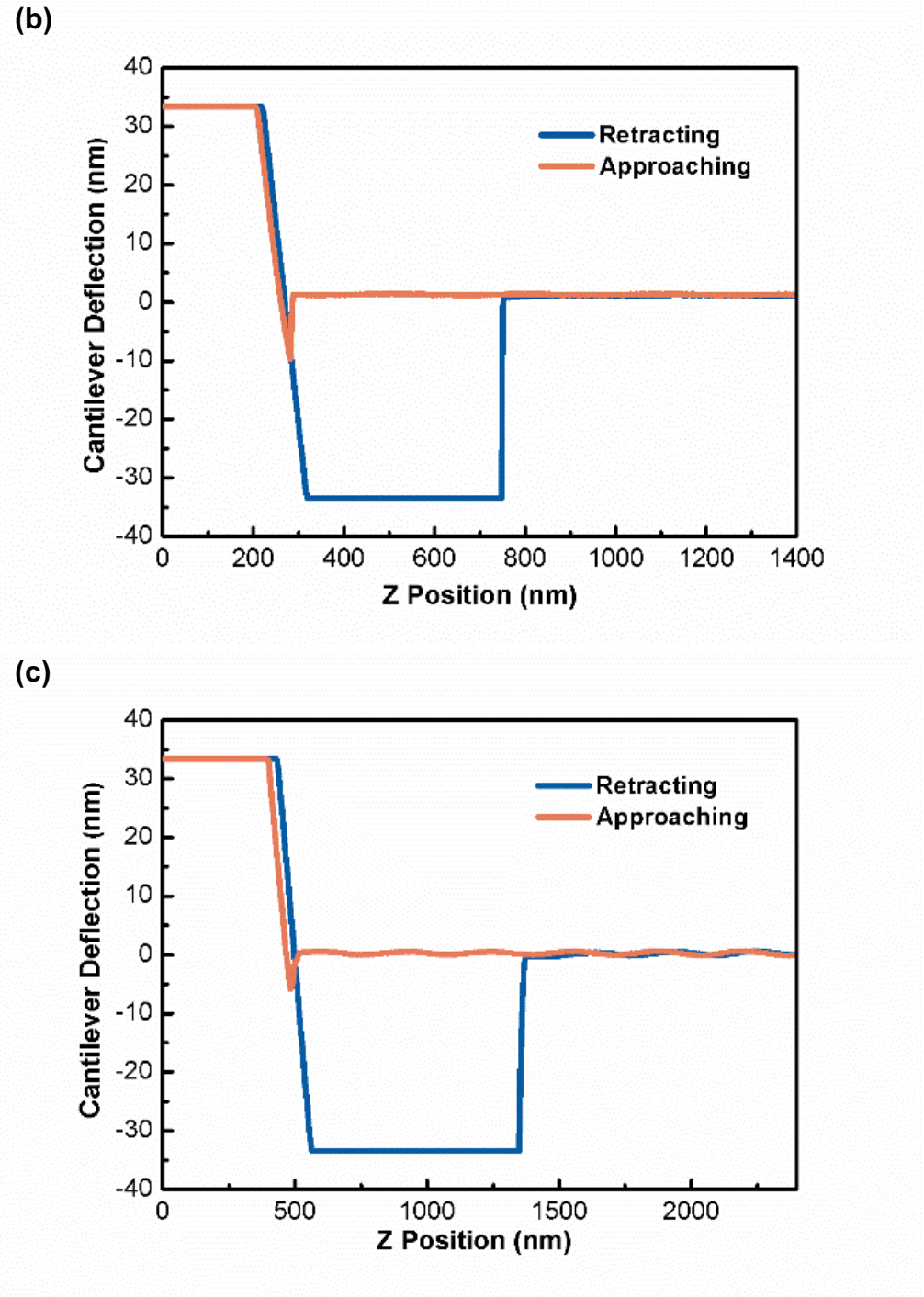

Figure 11: Representative of cantilever deflection-Z position curves for (a) the calcium carbonate-binder interface; (b) the silica-binder interface; and (c) the alumina-binder interface.

3.3.4 Surface energy

Surface energy per unit area, γ, has been used to characterize the adhesion of asphalt materials [107, 172]. In this study, the Derjaguin-Muller-Toporov (DMT) [173] model was used to calculate γ between the aggregates and binders. The DMT model assumed that deformed surface geometry remained the same as the Hertzian contact area [174], and Van der Waals acting along the contact area perimeter provided additional attractive interactions. The relationship between the adhesive force and the unit surface energy is obtained by

$$\gamma = \frac{F_{ad}}{4\pi R} \tag{5}$$

where Fad is the adhesive force between the particle and the substrate and R is the radius of the microsphere.

3.3.4.1 Adhesion between PG 64-22 and aggregate particles

The adhesive forces between a calcium carbonate particle and a PG 64-22 binder substrate were shown in Fig. 12a. The measured adhesive forces were on the order of micronewtons resulting from much larger contact areas between the mineral particles and the binder substrates compared to those between the bare SFM tips and substrates. Fig. 10b showed values of γ for three different particle-substrate pairs. For each particle-substrate pair, variations of the adhesion measurements were detected between different particle-substrate replicas. This was probably because the particles contacted different phases of the binders. The adhesion between the aggregate minerals and different binder phases will be explored in future work.

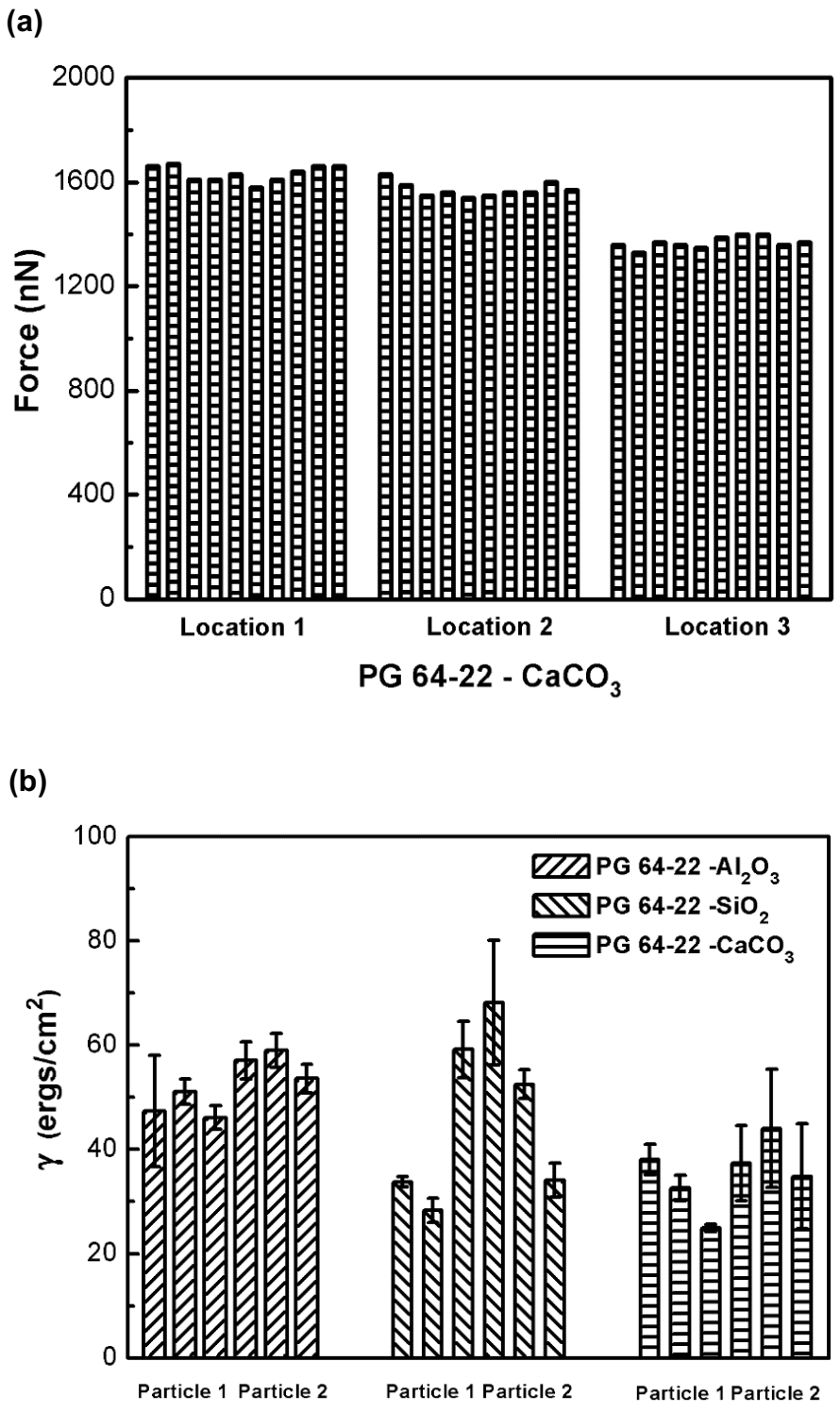

Figure 12: (a) adhesion between a calcium carbonate particle and different locations of one PG 64-22 binder substrate; (b) the unit surface energy measurements between different particle-substrate interfaces of one PG 64-22 binder substrate.

3.3.4.2 Adhesion between different asphalt binders and aggregate particles

The same approach was employed to investigate the adhesion between different asphalt binders and aggregate particles. Fig. 13a showed the unit surface energy among different particles and the PG 58-22, PG 64-22 and PG 70-22 binders, i.e., a binder series possessing the same minimum pavement design temperature. For each type of binder, consistent trends were obtained for the adhesion between mineral particles (silica, calcium carbonate and alumina particles) and the binder substrates. The alumina-binder pairs exhibited the largest adhesion, while silica-binder and calcium carbonate-binder pairs exhibited relatively smaller adhesion. Similar trends were observed for the adhesion between the PG 64-16, PG 64-22 and PG 64-28 binders and the mineral particles (Fig. 13b). When adhesion results were compared among different binders, the alumina-binder pairs exhibited a relatively clear trend. The alumina-binder adhesion decreased as the value of the maximum pavement design temperature increased (Fig. 13a), while the alumina-binder adhesion increased as the value of the minimum pavement design temperature decreased (Fig. 13b). The silica-binder and calcium carbonate-binder adhesion did not exhibit any monotonic trend.

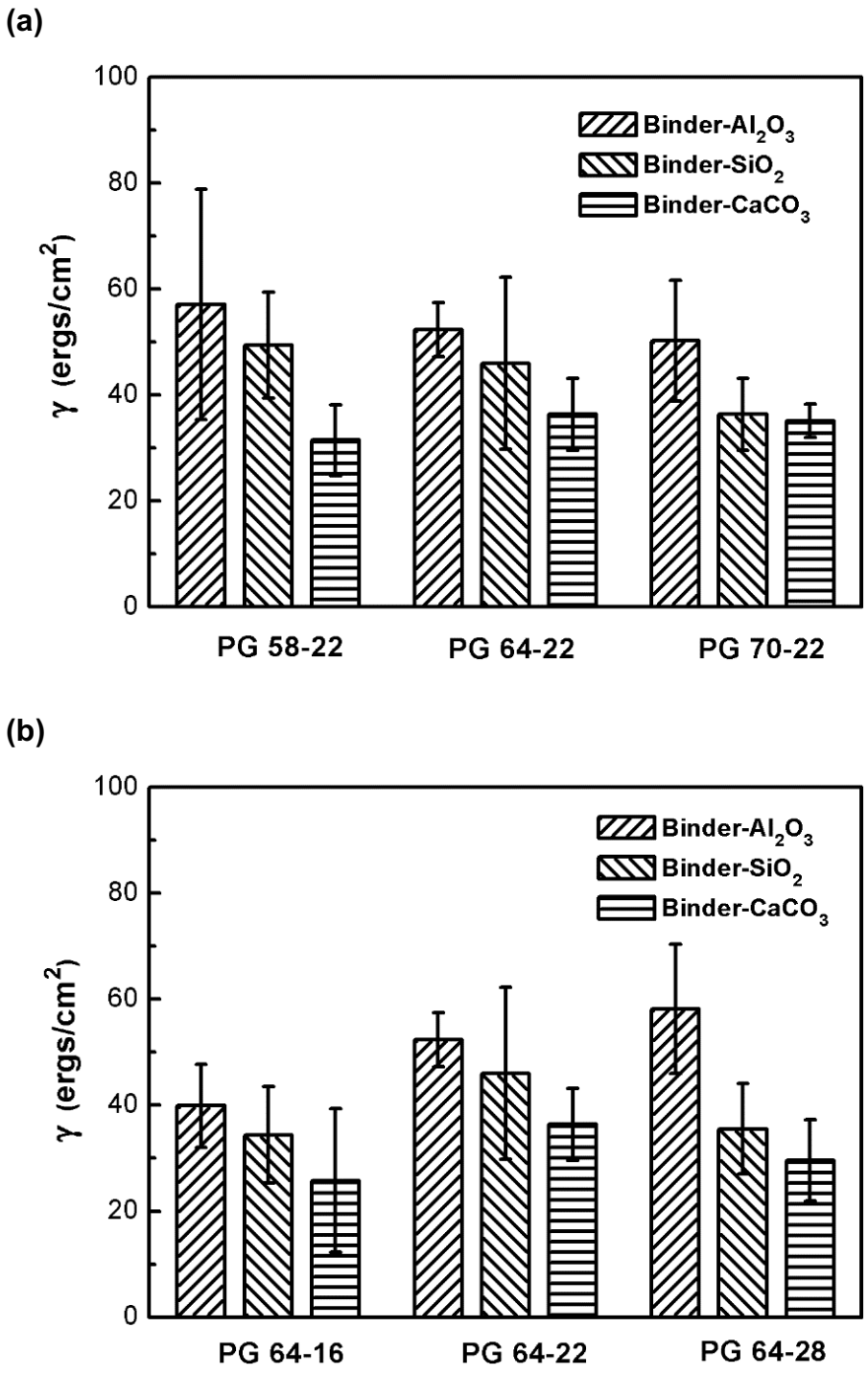

Figure 13: Average unit surface energy between different particles and (a) the binders included PG 58-22, PG 64-22, and PG 70-22; (b) the binders included PG 64-16, PG 64-22, and PG 64-28.

Measurement was also extended to PPA modified binders and the aggregate particles. Fig. 14 showed the unit surface energy γ between aggregate particles and the PPA modified PG 64-22 binders. Likewise, the alumina-binder pair showed the largest adhesion. As the PPA weight percentage increased, the adhesion of alumina-binder pairs increased accordingly. However, the adhesion of the silica- and calcium carbonate-binder pairs decreased generally. The results showed that the PPA did affect the adhesion between binders and the aggregate particles.

The adhesion differences can be attributed to the chemical properties of alumina, silica and calcium carbonate particles. Among these three, alumina is the most polar, and calcium carbonate and silica are less polar [175, 176]. Based on the SARA fraction of binders [6], it is known that a great portion of binders is resin, i.e., polar aromatic. Therefore, the interaction between the alumina particles and the asphalt binders lead to larger adhesion.

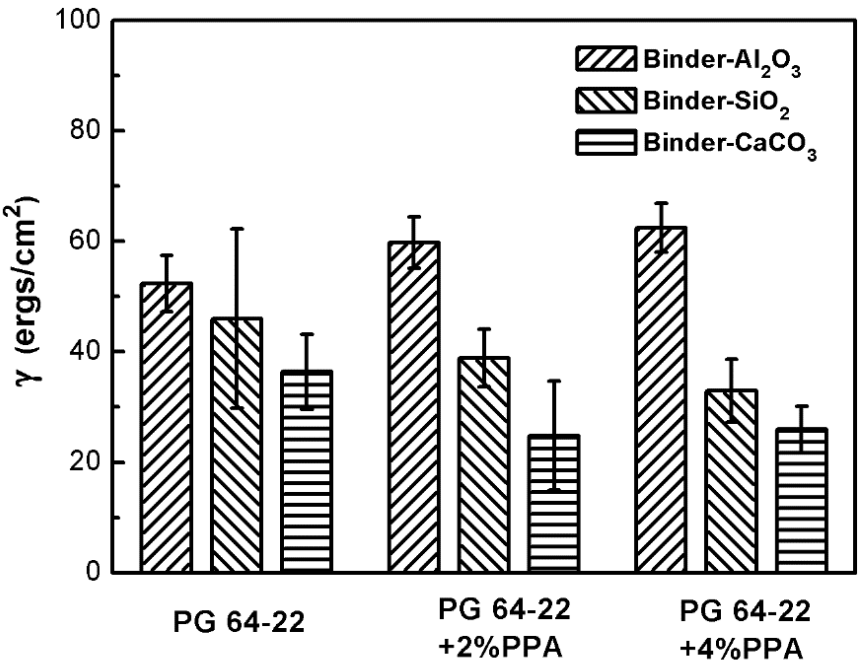

Figure 14: the average unit surface energy between different particle-substrate interfaces of PPA modified asphalt binders.

3.4 CONCLUSIONS

In this chapter, an experiment approach was present to measure the adhesion between the asphalt binders and different aggregate mineral particles (silica, calcium carbonate and alumina) at the microscopic scale using the particle-modified probes. Results showed that these modified SFM probes could effectively measure the adhesion between binders and aggregate minerals. In particular, these studies shine lights on the understanding of the crack mechanisms of asphalt mixtures at the microscopic level, a critical scale for the crack initiation and propagation [65]. Our results are consistent with general consensus that SFM techniques characterize the Lifshiz-van der Waals component

in adhesion [58]. This study does not investigate the adhesion by the Lewis acid-base component [172, 177] and the interlocking mechanism [71, 72].

Consistent adhesion measurements were obtained between different asphalt binders and aggregate mineral particles. Our results have shown that the alumina-binder pairs exhibit the largest adhesion, while the silica- and calcium carbonate-binder pairs exhibits relatively smaller adhesion. In addition, adding PPA to the plain PG 64-22 binder can affect the adhesion between the binder and aggregate particles.

CHAPTER 4: ADHESION BETWEEN MODIFIED ASPHALT BINDERS AND AGGREGATES

In this chapter, the adhesion between modified asphalt binders and the primary aggregate minerals was studied under ambient conditions using the PPSFM method. The objective of this study is to perform a comprehensive set of statistical analyses to quantify the effects of factors described above on the aggregate-binder adhesion measured using particle probe scanning force microscopes. The materials and methods are briefly introduced in the beginning, and the statistical analyses are detailed in following sections.

4.1 Results

4.1.1 Particle Probes Used for Scanning Force Microscopes

The fabricated particle probes were examined using a scanning electronic microscope (JEOL JSM 6060, Peabody, MA). In Fig. 15, two representative particle probes, made from a silica and a calcium carbonate microsphere, were shown in SEM images. Ideal contacts existed between microspheres and binder substrates. Spring constants of particle-modified cantilevers used in the study were summarized in Table 5 and Table 6, ranging from 1.0 to 5.7 N/m. Diameters of mineral spheres used in this study ranged from 5.9 to 13.0 μm (Table 7 & 8).

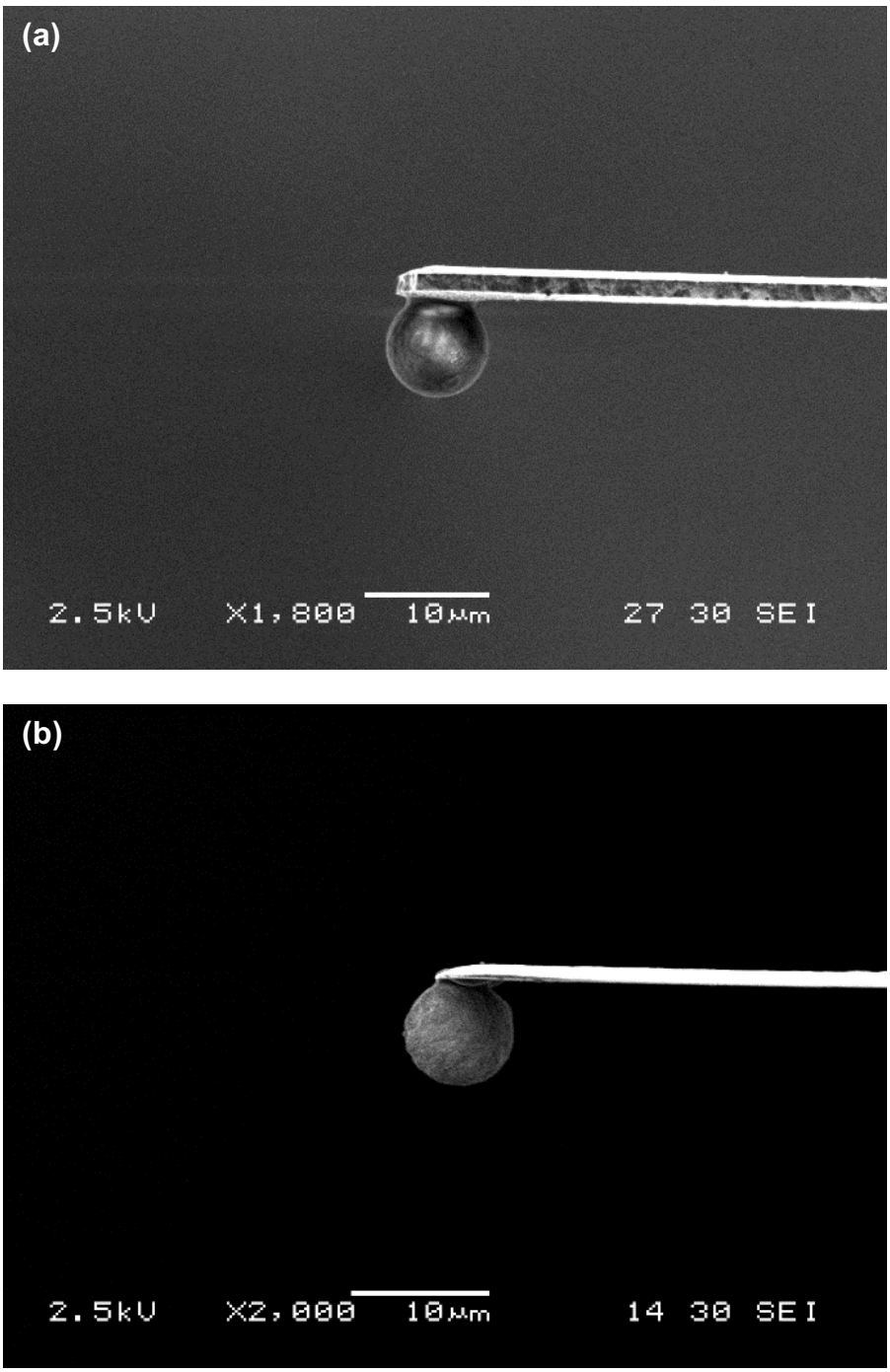

Figure 15: SEM images of particle probes, with (a) a silica microsphere; and (b) a calcium carbonate microsphere.

Table 5: Spring constants (N/m) of particle probes used for PG 58-22 series.

Binder substrates	Al_2O_3		SiO_2		$CaCO_3$	
	Particle 1	Particle 2	Particle 1	Particle 2	Particle 1	Particle 2
PG 58-22	4.1	5.7	3.8	3.1	3.7	1.8
PG 58-22+2%PPA	4.6	4.9	4.9	5.3	4.6	4.2
PG 58-22+4%PPA	4.8	3.5	4.8	4.6	3.8	4.5
PG 58-22+2%SBS	5.6	4.6	4.0	5.0	4.9	4.3
PG 58-22+4%SBS	4.7	5.0	3.9	4.5	4.5	4.1
PG 58-22+2%SBR	4.3	4.6	4.6	5.4	4.0	4.5
PG 58-22+4%SBR	5.4	5.0	5.3	5.3	4.8	5.0

Table 6: Spring constants (N/m) of particle probes used for PG 64-22 series.

Binder substrates	Al_2O_3		SiO_2		$CaCO_3$	
	Particle 1	Particle 2	Particle 1	Particle 2	Particle 1	Particle 2
PG 64-22	2.2	3.4	5.6	5.0	5.4	5.1
PG 64-22+2%PPA	3.3	2.8	2.9	2.8	2.8	1.0
PG 64-22+4%PPA	2.7	3.1	2.0	3.4	1.6	1.4
PG 64-22+2%SBS	5.1	4.3	4.4	5.5	4.8	4.4
PG 64-22+4%SBS	4.2	4.7	4.1	3.1	4.8	4.5
PG 64-22+2%SBR	1.5	2.7	1.4	2.9	1.5	3.1
PG 64-22+4%SBR	1.2	4.0	2.8	1.3	1.1	1.0

Table 7: Diameters (μm) of microspheres used for PG 58-22 series.

Binder substrates	Al_2O_3		SiO_2		$CaCO_3$	
	Particle 1	Particle 2	Particle 1	Particle 2	Particle 1	Particle 2
PG 58-22	13.0	10.4	8.0	7.9	8.1	6.9
PG 58-22+2%PPA	10.0	10.8	7.9	8.6	7.1	6.3
PG 58-22+4%PPA	8.3	8.5	7.8	7.4	5.9	6.5
PG 58-22+2%SBS	10.4	9.2	8.4	7.7	7.0	7.6
PG 58-22+4%SBS	9.6	7.5	7.9	6.5	7.3	7.0
PG 58-22+2%SBR	8.7	10.5	7.7	7.0	7.3	6.6
PG 58-22+4%SBR	10.8	10.4	7.5	7.6	6.9	7.6

Table 8: Diameters (μm) of microspheres used for PG 64-22 series.

Binder substrates	Al_2O_3		SiO_2		$CaCO_3$	
	Particle 1	Particle 2	Particle 1	Particle 2	Particle 1	Particle 2
PG 64-22	7.7	8.3	8.3	7.0	10.1	7.7
PG 64-22+2%PPA	7.6	7.3	10.1	8.5	7.2	8.2
PG 64-22+4%PPA	7.3	8.0	7.1	7.3	7.9	6.9
PG 64-22+2%SBS	8.4	8.7	8.1	8.0	6.0	7.0
PG 64-22+4%SBS	7.7	8.1	8.3	8.0	6.6	6.8
PG 64-22+2%SBR	9.3	6.6	7.4	8.1	7.2	9.0
PG 64-22+4%SBR	7.1	7.6	7.2	8.0	6.5	6.6

4.1.2 SFM force curves

A typical force curve between a silica microsphere probe and a PG 58-22 binder substrate was shown in Fig. 16. The vertical axis is a measure of the signal in the arbitrary unit and the horizontal axis is the z-travel of the tip in nm. In the beginning of the approaching segment (the red curve), the photodetector signal was constant since the probe was not in contact with the substrate. Once the probe contacted substrate and the cantilever was continuously driven forward, the defection signal increased linearly. In retracting, the cantilever bent reversely so the signal decreased with the same slope. The spherical probe did not disengage from substrate until the restoring force in the cantilever overcame the adhesion between the probe and substrate. After that, the deflection signal became flat again since the microsphere disengaged from the sample surface. Δx was the travel distance of probe between the contact and snap-off points. Note that the signal was flat at the bottom of the retracting curve since the deflection signals were beyond the instrumental range, but the measurement of Δx was not affected.

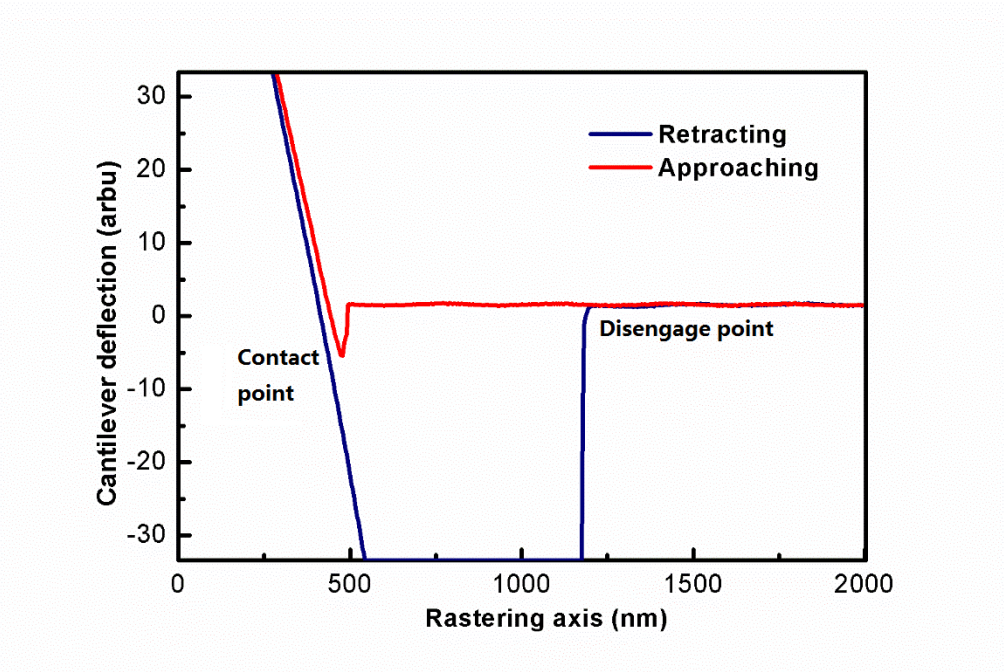

Figure 16: A representative force curve between a silica spherical probe and a PG 58-22 binder substrate.

4.1.3 Adhesive Forces between Aggregate Minerals and Binders

In Fig. 17, adhesive forces between a silica microsphere and three locations on a PG 58-22 binder substrate were illustrated. Note these data revealed the measured forces were in the range of micro-Newtons because much larger contact areas existed between microspheres and binder substrates compared to those obtained between plain SFM tips and substrates. It also showed that consistent force measurements were obtained between the silica microsphere and the binder substrate at different locations.

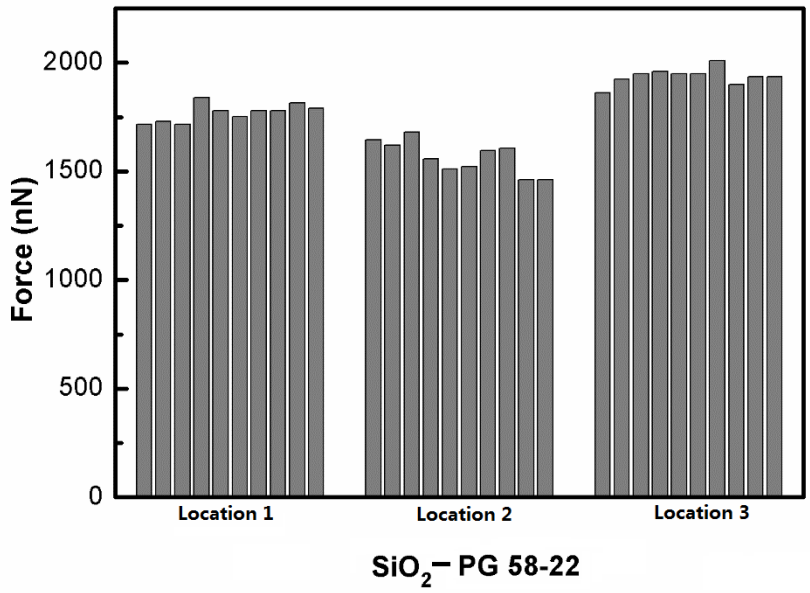

Figure 17: Adhesive forces between a silica microsphere and a PG 58-22 binder substrate.

4.1.4 Adhesion between asphalt binders and aggregate particles

In this study, surface energy per unit area was used to quantify the adhesion between mineral spheres and binder substrates. According to the Derjaguin-Muller-Toporov (DMT) model [173], deformed contact surface remained the same as the Hertzian contact [174], and Van der Waals acting along the contact area perimeter generated attractions. DMT model provided more realistic predictions for a hard sphere on a soft planar surface [178, 179], which has been used to quantify the adhesion of asphalt binders in prior studies [84, 107, 108, 180, 181].

Unit surface energies between aggregate particles and different binders are shown in Fig. 16. For each binder group containing three mineral-binder pairs, surface energies between alumina spheres and binder substrates are the largest. For control binders, i.e., PG

58-22 and PG 64-22, the alumina-binder adhesion generally increased as the binder softens, and more data variations were detected. However, no monotonic trends were observed between silica and calcium carbonate particles and control binders. For the same control binder, the alumina-binder adhesion increased as weight percentages of polymer modifiers (PPA, SBS, and SBR) increase (Figs 18a to 18c). The adhesion trends between silica particles and modified binders were relatively complicated. In PG 58-22 series, the silica-binder adhesion increased as weight percentages of SBR increases (Fig. 18b). However, in PG 64-22 series, the silica-binder adhesion decreased as the weight percentage of PPA increases (Fig. 18c), but similar trends were not observed in SBR and SBS modified PG 64-22 binders. Complex trends also existed between calcium carbonate particles and various binders. Generally, no monotonic trends were observed between silica and calcium carbonate particles and modified binders used in this study. These results showed that SBS, SBR, and PPA modifiers did affect the adhesion between binders and aggregate minerals.

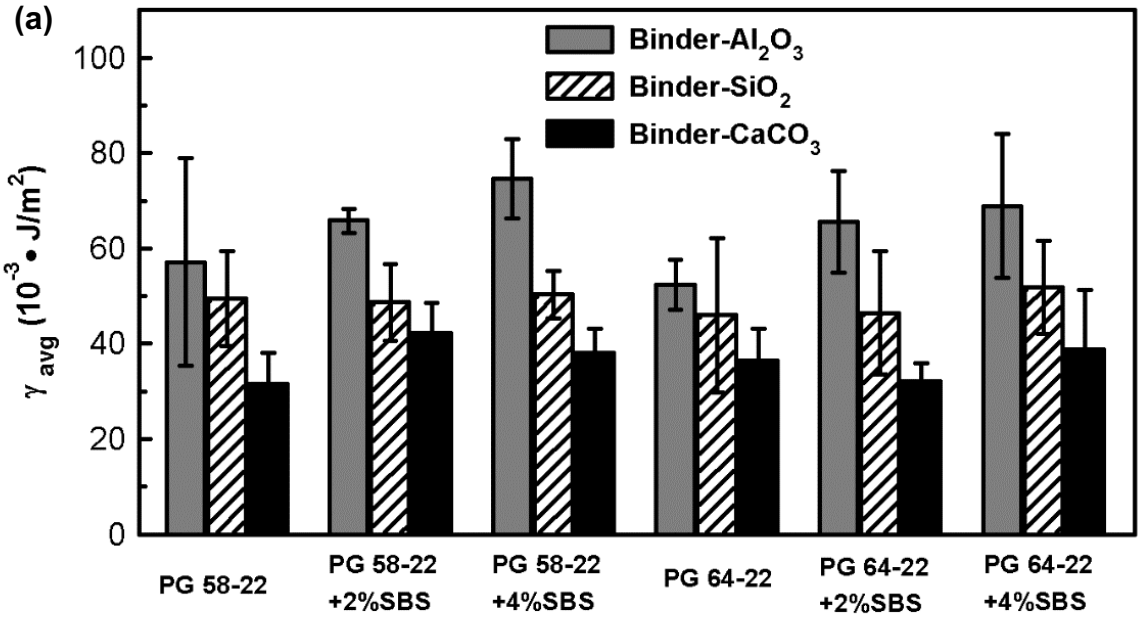

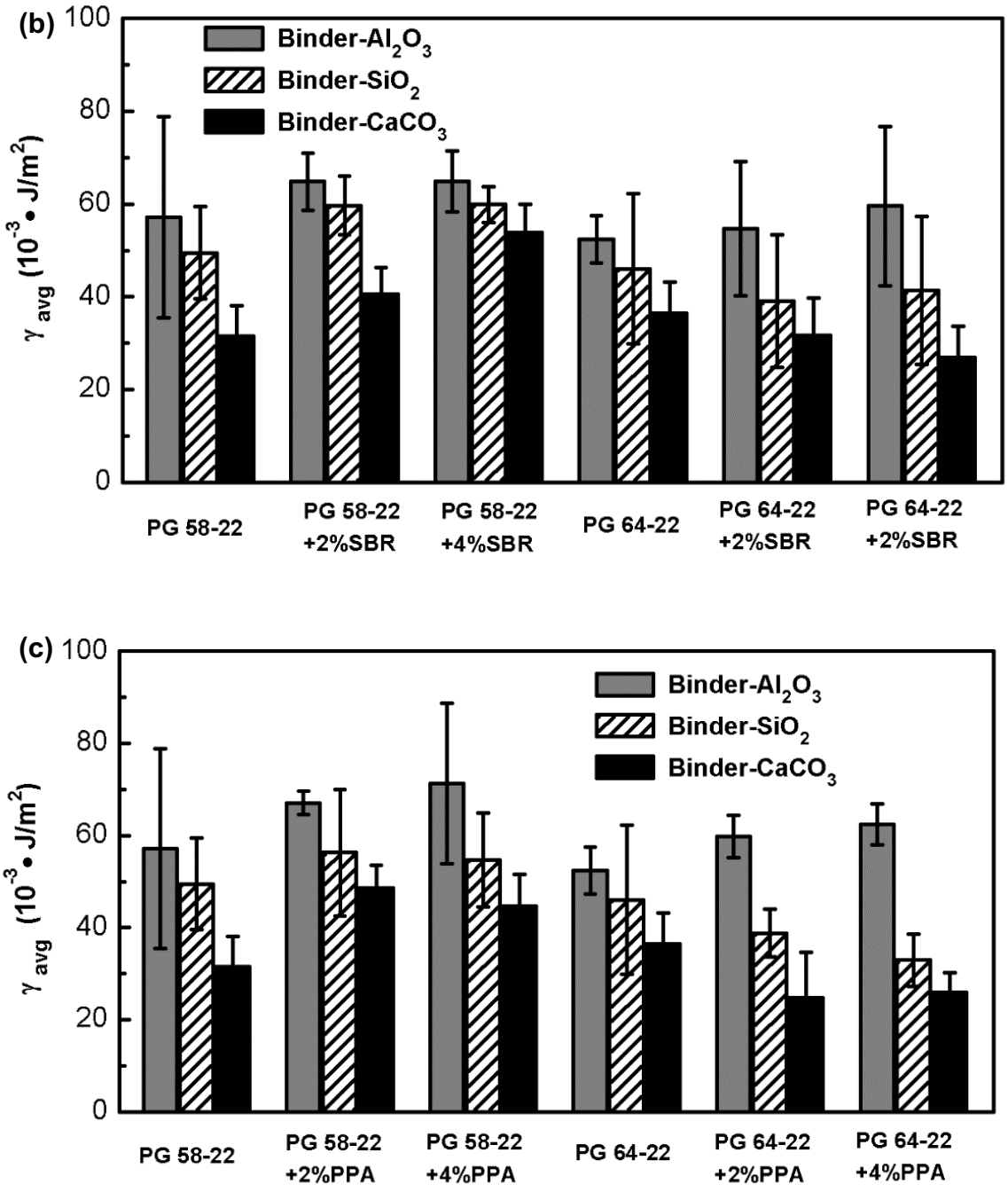

Figure 18: Unit surface energies of PG 58-22 and PG 64-22 binder series, (a) 2 and 4 wt.% SBS modifications; (b) 2 and 4 wt.% SBR modifications, and (c) 2 and 4 wt.% PPA modifications.

The surface energy differences between various aggregate mineral-binder pairs are attributed to chemical properties of alumina, silica, and calcium carbonate particles. Among these three, alumina spheres have the most polar constituents, while calcium carbonate and silica have less polar constituents [175]. According to the SARA classification in ASTM [7], a great portion of binder components are resins, which are polar aromatic substances. Therefore, larger adhesion is induced through stronger interactions between alumina particles and binders. These hypotheses will be examined in the future modeling work.

T-tests were conducted to evaluate the performance of particle probes in distinguishing binders based on the adhesion results. The evaluation focused primarily on the adhesion of modified binders used in this study. Based on the 95% confidence interval, T-tests results were summarized in Table 9 for various binder-aggregate pairs. For example, in the SBR modified PG 58 series, subscripts 0, 2 and 4 denoted the 0, 2 and 4 wt.% SBR modifications to the PG58-22 binder, respectively. Therefore, statistical differences between any two of the three were filled in the table accordingly. Based on these results, adhesion measurements using particle probes were different for most aggregate-binder pairs except for a few combinations. For example, similar adhesion results were obtained between alumina and silica particles and 2 and 4 wt.% SBR modified PG 58-22 binders. In the PG 64-22 series, adhesion measurements between several aggregate mineral-binder pairs were also close, such as pairs of silica particles and 0 and 2 wt.% SBS modifications, and pairs of calcium carbonate particles and 2 and 4 wt.% PPA modifications. Overall, the adhesion differences between various aggregate mineral-binders were successfully detected.

Table 9: T-test results of different binder-aggregate adhesion.

Particle	SBR modified PG58 series			SBR modified PG64 series		
	$P(SBR_{02})$	$P(SBR_{04})$	$P(SBR_{24})$	$P(SBR_{02})$	$P(SBR_{04})$	$P(SBR_{24})$
Al_2O_3	4.1E-5	2.4E-7	9.7E-1	2.9E-1	9.8E-5	7.7E-4
SiO_2	1.7E-21	1.5E-19	8.5E-1	5.1E-6	1.9E-2	2.2E-1
$CaCO_3$	5.9E-26	8.2E-62	9.0E-32	2.2E-10	1.2E-22	1.2E-8

Particle	PPA modified PG58 series			PPA modified PG64 series		
	$P(PPA_{02})$	$P(PPA_{04})$	$P(PPA_{24})$	$P(PPA_{02})$	$P(PPA_{04})$	$P(PPA_{24})$
Al_2O_3	5.8E-9	5.4E-7	1.3E-3	4.7E-10	1.5E-35	7.0E-3
SiO_2	2.2E-8	8.7E-9	2.5E-1	3.7E-6	1.7E-24	4.0E-8
$CaCO_3$	1.0E-42	4.6E-24	3.0E-4	1.5E-20	3.7E-30	1.7E-1

Particle	SBS modified PG58 series			SBS modified PG64 series		
	$P(SBS_{02})$	$P(SBS_{04})$	$P(SBS_{24})$	$P(SBS_{02})$	$P(SBS_{04})$	$P(SBS_{24})$
Al_2O_3	1.2E-7	1.4E-28	1.6E-16	1.6E-26	1.9E-23	1.6E-3
SiO_2	5.3E-1	3.7E-1	2.2E-2	7.7E-1	1.1E-4	1.2E-4
$CaCO_3$	7.3E-31	3.7E-13	1.8E-11	1.3E-6	8.9E-2	3.2E-9

Notes: SBR modified PG58 series: (0) PG58-22; (2) PG58-22+2%SBR; (4) PG58-22+4%SBR
PPA modified PG58 series: (0) PG58-22; (2) PG58-22+2%PPA; (4) PG58-22+4%PPA
SBS modified PG58 series: (0) PG58-22; (2) PG58-22+2%SBS; (4) PG58-22+4%SBS
SBR modified PG64 series: (0) PG64-22; (2) PG64-22+2%SBR; (4) PG64-22+4%SBR
PPA modified PG64 series: (0) PG64-22; (2) PG64-22+2%PPA; (4) PG64-22+4%PPA
SBS modified PG64 series: (0) PG64-22; (2) PG64-22+2%SBS; (4) PG64-22+4%SBS
The confidence interval is 95%.

4.2 Discussion

4.2.1 Distributions of the Δx Values

Parametric fitting was performed using the JMP software (SAS Institute Inc, Cary, NC) to characterize the distributions of Δx measurements. A representative data set consisting of 90 measurements between an alumina microsphere and a PG 64-22 binder substrate was shown in Fig.19. Four different distributions were employed to fit the data, including the normal, lognormal, Weibull and exponential distributions.

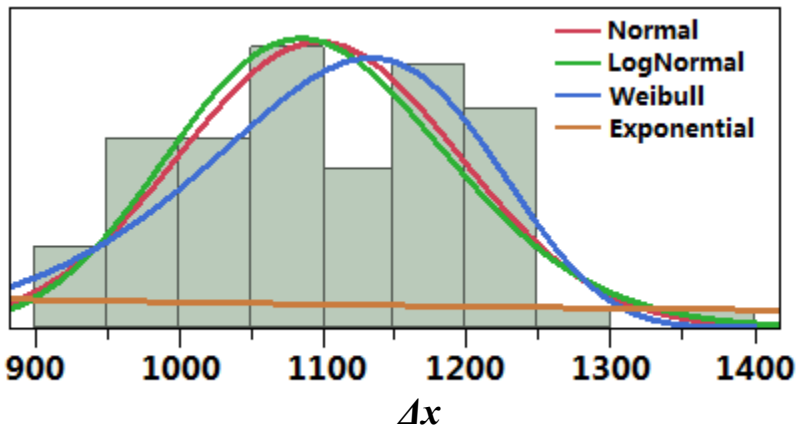

Figure 19: Representative fitting functions of Δx measurements between an alumina microsphere and a PG 64-22 binder substrate using normal, lognormal, Weibull and exponential distributions.

The results were summarized in Table 10 to illustrate the performance from these models. P-values greater than 0.05 were typically used as evidence that the parametric fit was effective. It shows that no parametric model exhibited better performance than others, meaning that no obvious distributions were observed for the Δx measurements using the particle probe scanning force microscopes. This was probably because the microspheres contacted different phases of the binder substrate, through which a generalized distribution of Δx measurements is difficult to achieve.

Table 10: p-value of PG 64-22 using different distribution fittings

Particle	Normal (Prob<W)	LogNormal (Prob>D)	Weibull (Prob<W^2)	Exponential (Prob>D)
Al_2O_3-I	0.0118	0.0351	0.0550	< 0.0100
Al_2O_3-II	0.0030	< 0.0100	< 0.0100	< 0.0100
SiO_2-I	<0.0001	< 0.0100	< 0.0100	< 0.0100
SiO_2-II	<0.0001	< 0.0100	< 0.0100	< 0.0100
$CaCO_3$-I	<0.0001	< 0.0100	< 0.0100	< 0.0100
$CaCO_3$-II	<0.0001	< 0.0100	< 0.0100	< 0.0100

Note: I and II are two microsphere replicas used in measuring one aggregate mineral-binder pair.

4.2.2 Effects of aggregate minerals on the aggregate-binder adhesion

For control binders with the same low temperatures performance grade (PG xx-22 binders), the alumina-binder adhesion slightly decreased as the maximum pavement design temperatures increased. The least square means of surface energy exhibited that adhesion differences were generally observed between various binders and the same type of minerals (Fig. 20a), except that similar adhesion results were detected between PG 64-22 and PG 70-22 binders when interacting with the calcium carbonate microspheres.

For control binders with the same high temperatures performance grade (Fig. 64-xx binders), the alumina-binder adhesion slightly increased as the minimum pavement design temperatures decreased. Similarly, the least square means of surface energy exhibited that adhesion differences were generally observed between various binders and the same type of minerals (Fig. 20b). One exception was observed when PG 64-16 and PG 64-28 binders interacted with the silica microspheres.

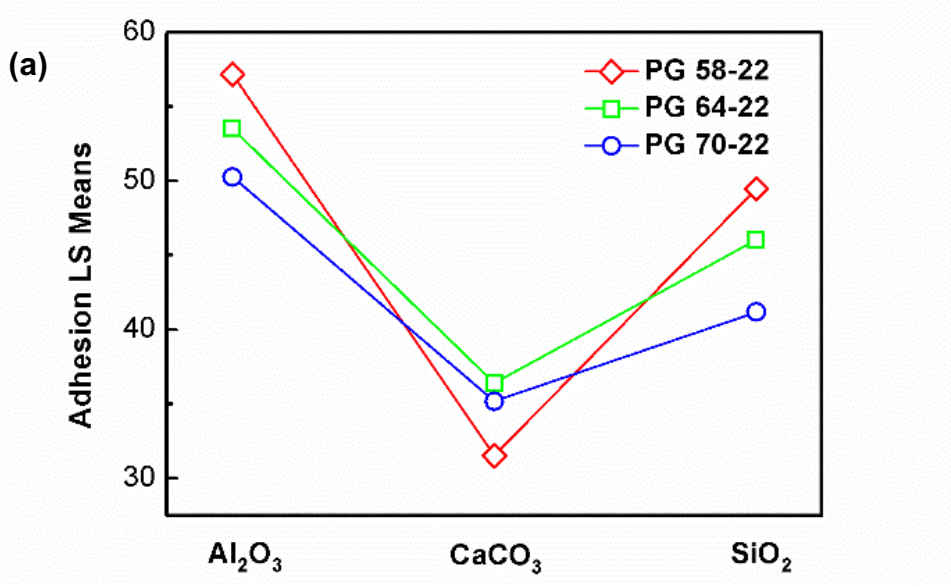

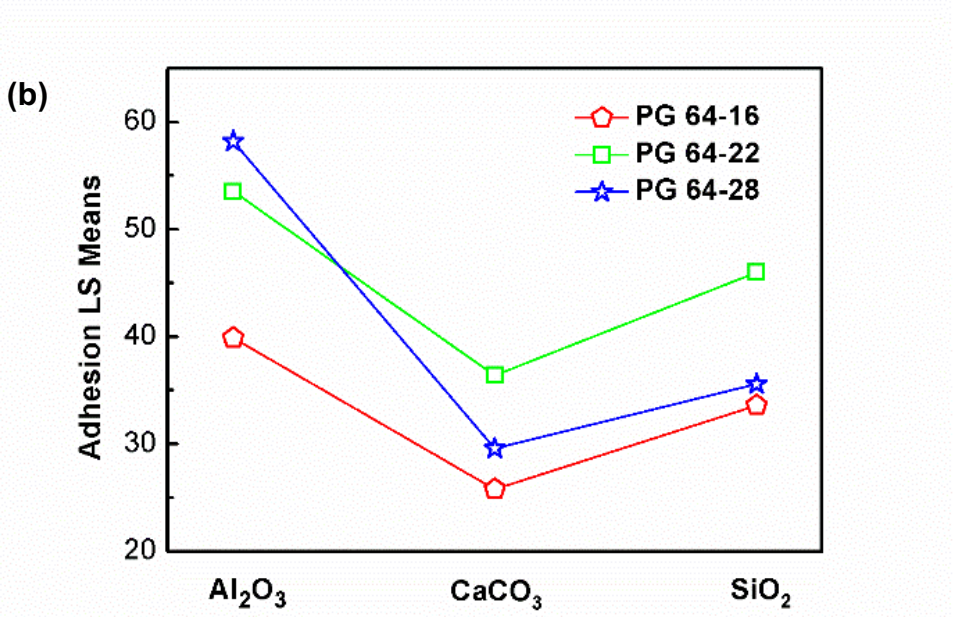

Figure 20: Least squares means of adhesion data between alumina, calcium carbonate and silica microspheres and (a) binders with the same low temperatures performance grade; (b) binders with the same high temperatures performance grade.

4.2.3 Effects of modifiers on the aggregate-binder adhesion

For SBR modified binders, the alumina-binder adhesion was the largest and increased as the SBR percentage increased (Fig. 18a). The least squares mean of adhesion (Fig 21a) exhibited that adhesion differences between modified PG 64-22 binders with different weight percentages of SBR were observed. One exception existed when the plain and 2 wt.% SBR modified PG 64-22 binders interacted with the alumina microspheres.

For SBS modified binders, the alumina-binder adhesion was the largest, and increased as the SBS percentage increased (Fig. 18b). The least squares mean of adhesion (Fig 21b) exhibited that aggregate-binder adhesion was generally different between modified PG 64-22 binders with different weight percentages of SBR. An exception was

observed when the plain and 2 wt.% SBS modified PG 64-22 binders interacted with the silica microspheres.

For PPA modified binders, the alumina-binder interfaces also exhibited the largest adhesion that increased as the weight percentages of PPA increased (Fig. 18c). The least squares mean of adhesion (Fig 21c) exhibited that aggregate-binder adhesion was different between aggregate minerals and PPA modified binders, except that similar adhesion was observed between calcium carbonate microspheres and 2 and 4 wt.% PPA modified PG 64-22 binders.

In general, the alumina-binder pairs exhibited the largest adhesion for plain and modified binders. For the same control binder, the alumina-binder adhesion increased as weight percentages of polymer modifiers (SBR, SBS, and PPA) increased, while no monotonic trends in silica- and alumina- binder pairs were observed. Similar trends were observed in PPA, SBS and SBR modified PG 58-22 binders.

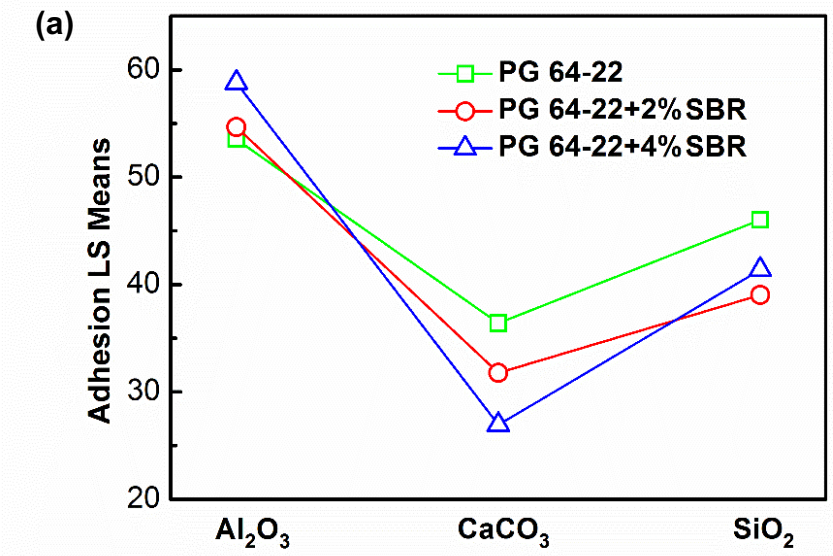
(a)
Adhesion LS Means
60
50
40
30
20
PG 64-22
PG 64-22+2%SBR
PG 64-22+4%SBR
Al2O3
CaCO3
SiO2

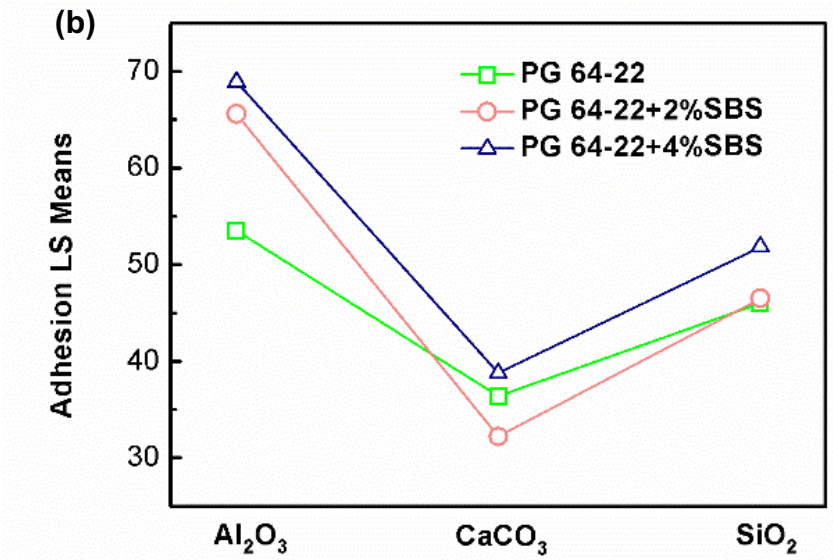
(b)
Adhesion LS Means
70
60
50
40
30
PG 64-22
PG 64-22+2%SBS
PG 64-22+4%SBS
Al2O3
CaCO3
SiO2

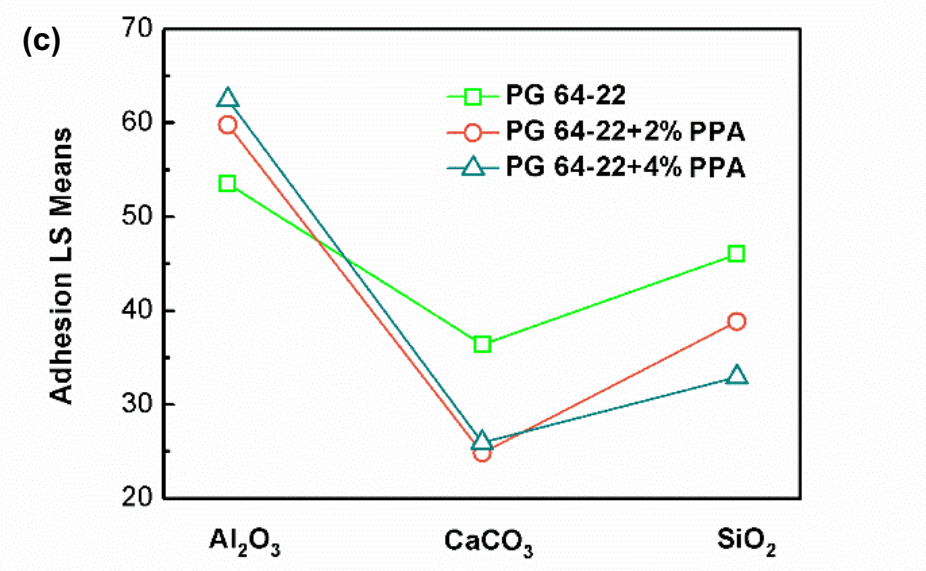

Figure 21: Least squares means of adhesion data between alumina, calcium carbonate and silica microspheres and modified PG 64-22 binders with (a) 2 and 4 wt.% SBR; (b) 2 and 4 wt.% SBS; (b) 2 and 4 wt.% PPA.

This method directly quantifies the adhesion between primary aggregate minerals and binders in microscale. By using this method, the production of asphalt binders can be more precisely controlled to improve aggregate-binder adhesion. The aging mechanisms of the aggregate-binder interfaces can be further studied under various conditions. The findings on interfacial adhesion can provide quantitative criterion of microscale crack initiation and propagation in asphalt mixtures, which could promote the development of multiscale asphalt mixture models.

4.2.3 Morphologies of Modified Binders

The SFM has been widely used to characterize the microstructure of different materials, or to measure the adhesion between nanoscale tips and substrates [77]. The tips are usually pyramids made from silicon or silicon nitride. The development of particle-

probe has inherited the cantilever idea, but microscale spheres are used to represent the primary chemical constituents of aggregates. The findings from particle-probe scanning force microscopes will provide essential clues for aggregate-binder adhesion in pavement materials.

Surface morphologies of control and modified binders were characterized using conventional SFM probes [82, 93, 182]. In Fig. 22, both height and amplitude traces were shown for the PG 58-22 binder (Figs. 22a and 22b), and 2 and 4 wt.% PPA modifications (Figs. 22c to 22f). Bee structures in the control PG 58-22 binder were clearly demonstrated by both height and amplitude traces (Figs. 22a and 22b), where alternating ripples were aligned along the longitudinal axis. In PPA modifications, bee structures were surrounded by flocculent wing structures (Figs. 22c to 22d). As weight percentages of PPA increased from 2 to 4 wt.%, the flocculent wings became more organized (Figs. 22e to 22f).

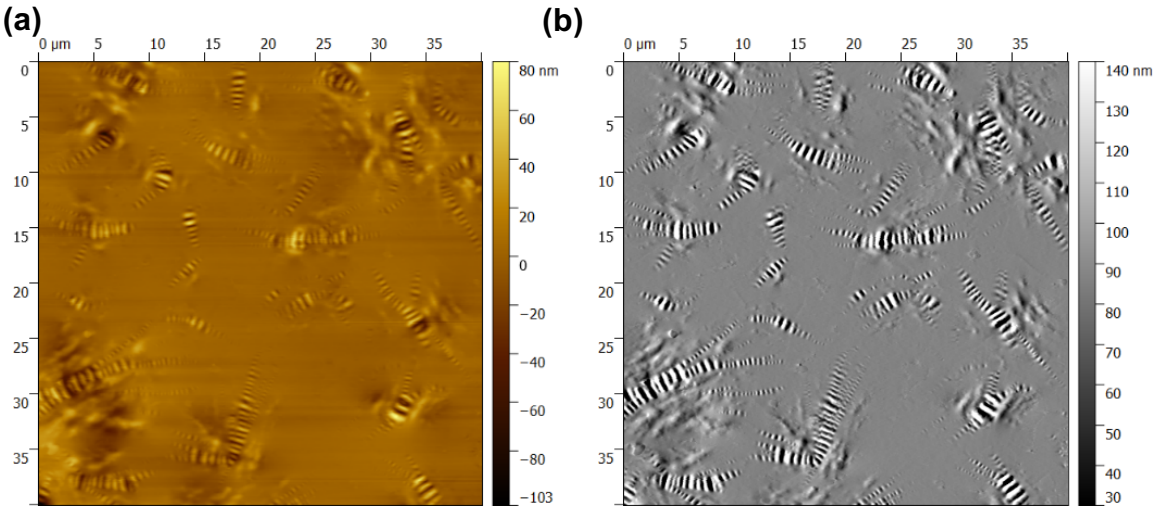

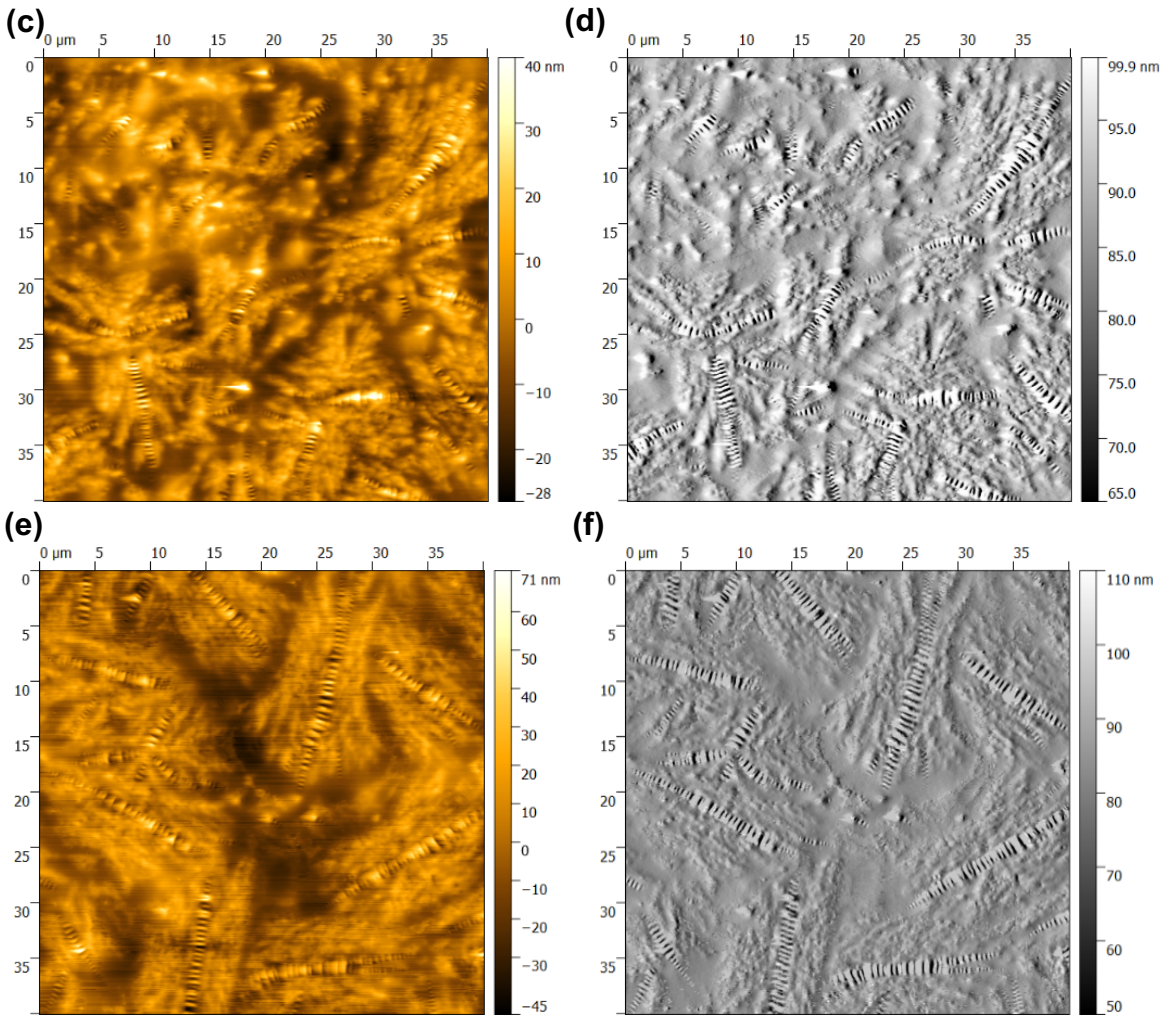

Figure 22: Height (left) and amplitude (right) scans (40 x 40 μm^2) of (a, b) control PG 58-22 binder; (c, d) 2 wt.% PPA modifications; and (e, f) 4 wt.% PPA modifications.

Heights and amplitude scans were also performed for SBS or SBR modified PG 58-22 binders in Fig. 23. As weight percentages of modifiers (SBS or SBR) increased from 2 to 4 wt.%, larger bee structures were detected with relatively sparse distributions (Figs. 23a to 23h). The microstructures of asphalt binders with SBS and SBR indicate that ‘‘bee structures” on sample surface tend to be changed in size and numbers, it may because adding SBS and SBR modifiers changed the microcrystalline wax.

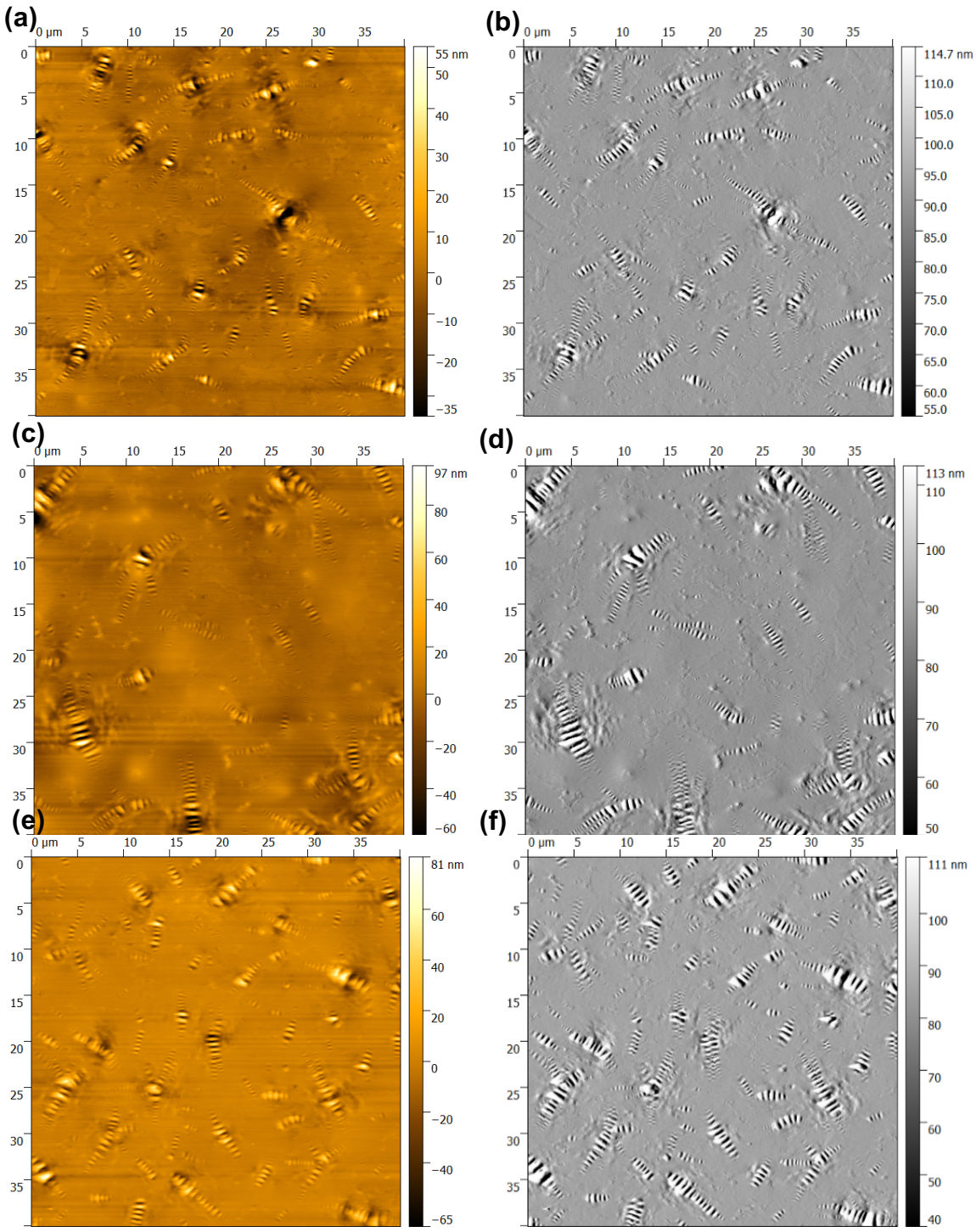
(a)
0 µm 5 10 15 20 25 30 35
0 5 10 15 20 25 30 35
55 nm 50 40 30 20 10 0 −10 −20 −35
(b)
0 µm 5 10 15 20 25 30 35
0 5 10 15 20 25 30 35
114.7 nm 110.0 105.0 100.0 95.0 90.0 85.0 80.0 75.0 70.0 65.0 60.0 55.0
(c)
0 µm 5 10 15 20 25 30 35
0 5 10 15 20 25 30 35
97 nm 80 60 40 20 0 −20 −40 −60
(d)
0 µm 5 10 15 20 25 30 35
0 5 10 15 20 25 30 35
113 nm 110 100 90 80 70 60 50
(e)
0 µm 5 10 15 20 25 30 35
0 5 10 15 20 25 30 35
81 nm 60 40 20 0 −20 −40 −65
(f)
0 µm 5 10 15 20 25 30 35
0 5 10 15 20 25 30 35
111 nm 100 90 80 70 60 50 40

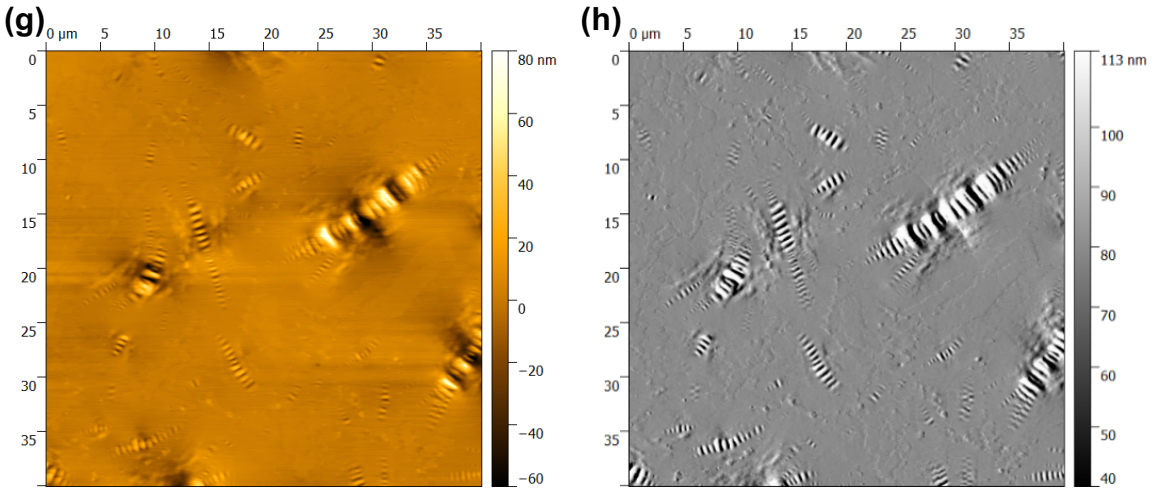

Figure 23: Height (left) and amplitude (right) scans (40 x 40 µm^2) of PG 58-22 binder: (a, b) 2 wt.% SBS modification; (c, d) 4 wt.% SBS modification; (e, f) 2 wt.% SBR modification SBR; (g, h) 4 wt.% SBR modification.

Similar morphologies were also observed in PG 64-22 modified series in Fig. 24 and Fig. 25. These results show that binder morphologies are affected by modifier types and weight percentages.

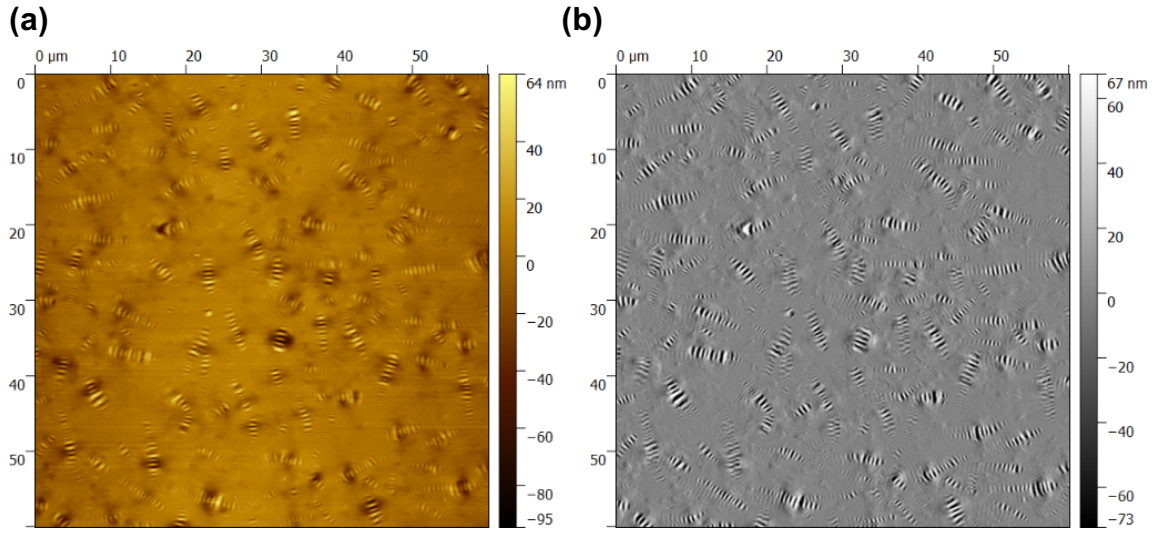

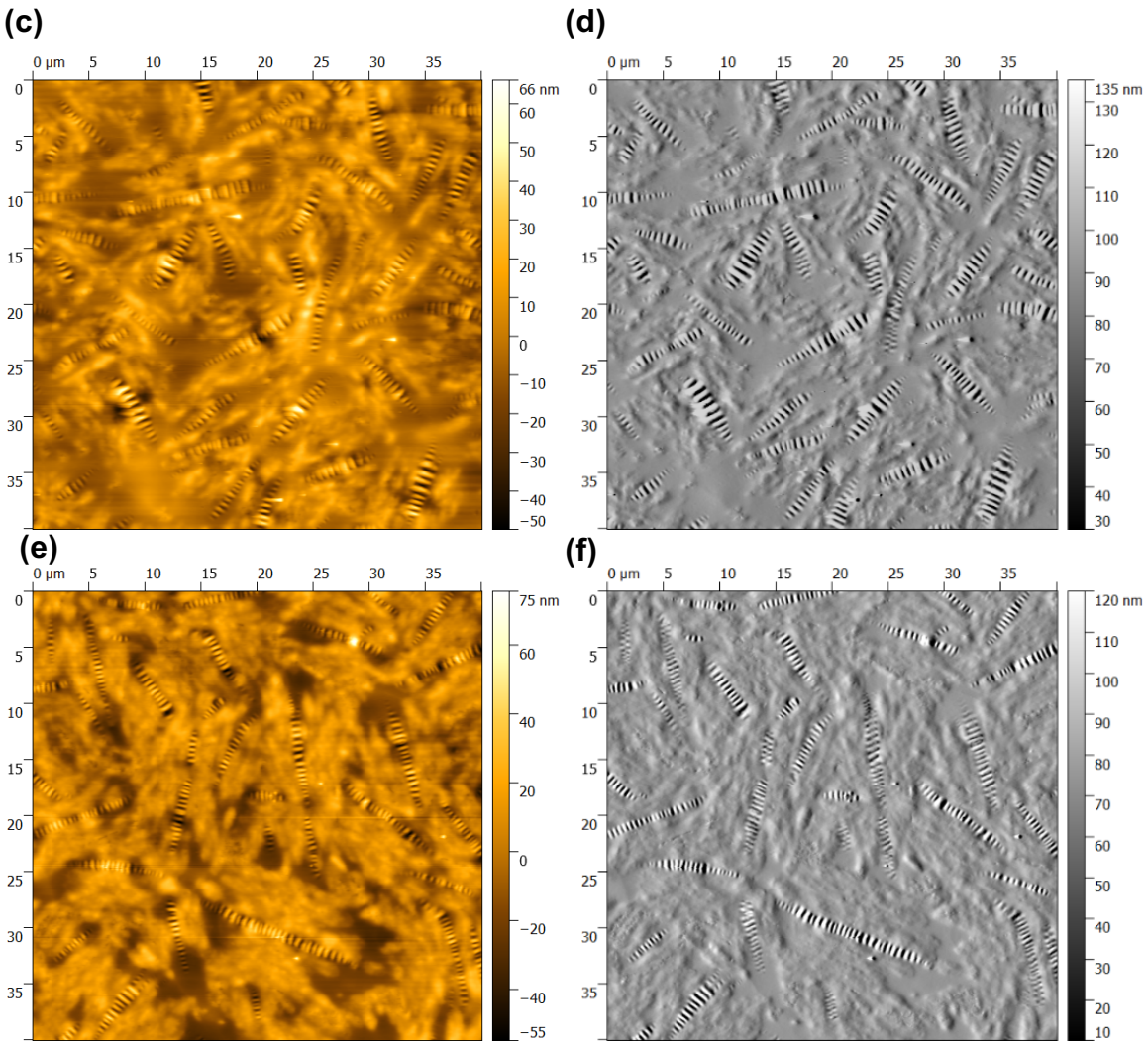

Figure 24: Height (left) and amplitude (right) scans (40 x 40 µm^2) of (a, b) control PG 64-22 binder; (c, d) 2 wt.% PPA modifications; and (e, f) 4 wt.% PPA modifications.

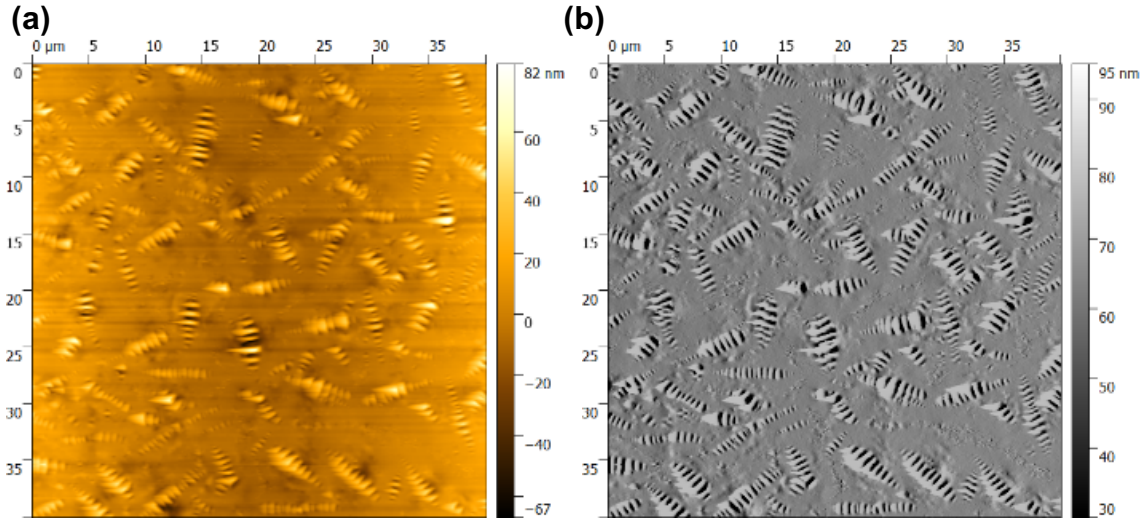

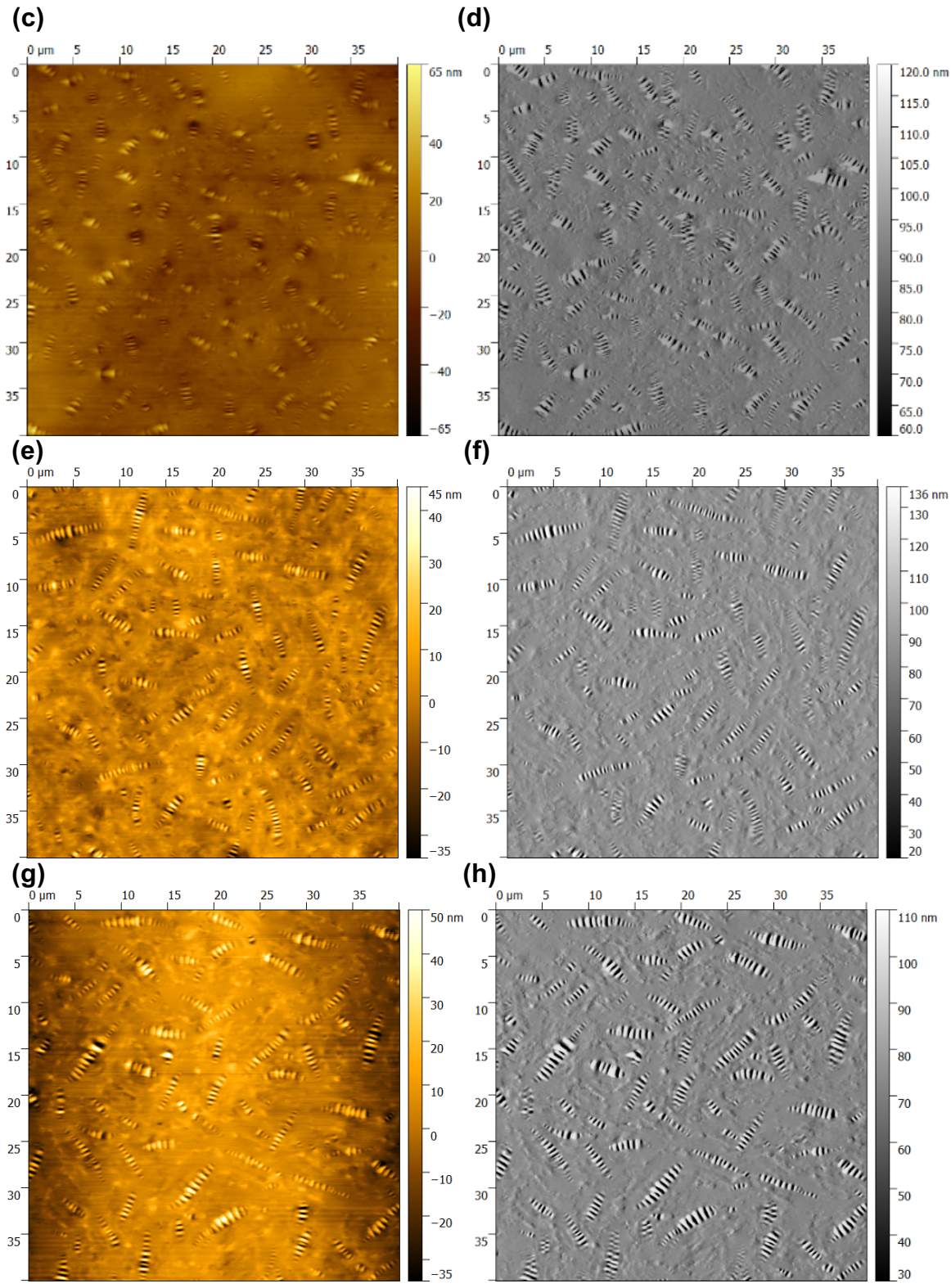

Figure 25: Height (left) and amplitude (right) scans (40 x 40 µm^2) of PG 64-22 binder: (a, b) 2 wt.% SBS modification; (c, d) 4 wt.% SBS modification; (e, f) 2 wt.% SBR modification SBR; (g, h) 4 wt.% SBR modification.

4.3 Conclusions

In this chapter, particle probe scanning force microscopes were used to measure the adhesion between aggregate minerals and different binders. Three types of particle probes were created using microspheres representing the primary chemical constituents of aggregates, i.e., silica, calcium carbonate and alumina. PG 58-22 and PG 64-22 binders were used as control binders. The surface energies between microspherical probes and binder substrates of various aggregate-binder pairs were measured with sufficient statistical consistency. The results showed that alumina-binder pairs exhibit the highest adhesion compared to silica- or calcium carbonate-binder pairs. Higher alumina-binder adhesion occurs as the binder became softer and as weight percentages of modifiers (PPA, SBS, and SBR) used in this study increased. Due to the stronger polarity of alumina particles, stronger interactions occur within alumina-binder pairs than within silica- and calcium carbonate-binder pairs. Meanwhile, morphologies of different modified binders clearly demonstrated microstructural variations in these binders. As weight percentages of modifiers increased, more organized flocculent wings occurred around bee structures in PPA modified binders. In SBS and SBR modified binders, larger bee structures occurred with more sparse distributions. These studies showed the correlation between the binder-aggregate adhesion and binder microstructures.

CHAPTER 5: ADHESION BETWEEN STEEL AND EARLY- HYDRATED CEMENT

Scanning Force Microscopy (SFM) has been used to measure different material properties, such as mechanical, magnetic and electrical properties [58] of bi-material interfaces. Conventional SFM probes are pyramids usually made from silicon or silicon nitride that include sharp radii on the order of nanometers. If adhesion tests were performed using these probes and cement substrates, the resulting measurements are not adhesion between the steel and cement. For example, Lomboy et al. [155] studied the adhesive forces between conventional silicon nitride SFM probes and cementitious substrates. Also, conventional SFM probes interacted locally to the substrates because of their sharp probe radii, making it difficult to link the nanoscale adhesion results to engineering applications. However, if a steel microsphere is used to replace the pyramid, the SFM can be used to measure the interactions between the microscale steel spheres and cement substrates. In this study, the adhesion between steel particles and early-hydrated cement (new) were measured in saturated calcium hydrate water using particle modified scanning force microscopy.

5.1 Materials and methods

5.1.1 Cement Paste Substrates

The cement substrates were prepared at the water:cement ratio of 0.5 using ordinary Type I/II Portland cement(The Quikerete, Atlanta, GA). The compositions were estimated by averaging the component percentages of Type I and II cements, i.e., C_3S (~55%), C_2S (~18%), C_3A (~10%) and C_4AF (~8%) by weight [183]. After mixing the cement powders

uniformly with water in a plastic cylinder with the diameter of 75 mm, the cement block was cured at ambient temperature for 24 hours. The cylinder was stored at saturated lime water for four weeks before small pieces were isolated to prepare the new cement specimens. The demolded cement cylinder was cut into cubes of 10 mm × 10 mm × 2 mm. The old cement specimens were prepared using the same cylinder that was stored in air for another five months. A series of polishing steps were employed to smooth the substrate surfaces before adhesive force measurements. The specimens were first polished using sand papers (3M, Maplewood, MN) with different grades (400, 800, 1200, 3000, 5000 and 7000 grits), and then polished using the cloth (Buehler, Norwood, MA) oil-based diamond suspensions (14000, 50000, 100000 grits) (Reentel International Inc., Westmont, IL). The polished substrates were cleaned by the ultrasonic machine using acetone for ~15 min. The substrate surfaces were imaged using the conventional SFM probes (NanoAndMore Corp., Watsonville, CA). The root mean square (RMS) of the surface roughness was ~60 nm at an area of 20 μm × 20 μm, which was smooth enough for contact between steel microspheres and cement substrates. Asylum MFP-3D-BIO scanning force microscope with commercial probes (NanoAndMore, Watsonville, CA) was used to characterize the morphology of polished cement substrates in AC mode at the frequency of ~300 kHz.

5.1.2 Steel microsphere probes

Steel particle probes were fabricated using stainless steel microspheres and silicon microcantilevers. The diameters of steel microspheres (Cospheric LLC, CA) were ~10 μm. The NSC microcantilevers (NanoAndMore Corp., Watsonville, CA) were bare rectangular bars sized in 90 μm (length) × 32.5 μm (width) × 1.0 μm (thickness). Spring constants of

the plain cantilevers ranged from 0.06 to 2.7 N/m. The attachment of a steel microsphere to a cantilever with epoxy was guided by an optical microscope as described in chapter 3. The movement of the cantilever using a high resolution microtranslation AD-100 system (Newport, Irvine, CA) was guided by an optical microscope (Nikon, Minato, Tokyo). First, the tip was dipped into a liquid epoxy on a glass slide. Then, it was moved to touch a target steel microsphere, also on the same glass slide. After that, the steel microsphere probes were left in air for 24 hours before measurements. The thermal tuning method [163, 164] was used to measure the spring constants of the particle probes as described in section 3.2.3. Commercial silicon SFM probes (NanoAndMore, Watsonville, CA) with nanoscale tip radii were also used to measure the adhesion. The spring constants of these commerical SFM probes ranged from 0.1 to 2.7 N/m.

5.1.3 Particle modified Scanning Force Microscope in liquid

A schematic of the scanning force microscopy used in this study is shown in Fig. 26. The SFM fluid cell, sealed by an O-ring, is filled with saturated lime water. In force probing, a microcantilever is driven by a piezoelectronic scanner over the substrate surface. The interactions between the probe at the free end of the cantilever and the substrate cause the cantilever to deflect, which is sensed by a laser beam on the cantilever back. Commercial SFM probes are mostly nanoscale pyramids. In this study, steel particle probes were created to measure the adhesive forces of bituminous and cementitious materials at microscale in air or in saturated lime water. As the cantilever approaches the cement substrate, the steel microsphere will contact the cement substrate surface. As the cantilever moves away from the substrate after making the contact, the cement paste and steel

microsphere will stick together until the restoring force of the deflected cantilever overcomes the adhesion between them. The cantilever is strong enough so that the deflection is linear elastic, in which the adhesive force calculated from Hooke's law。

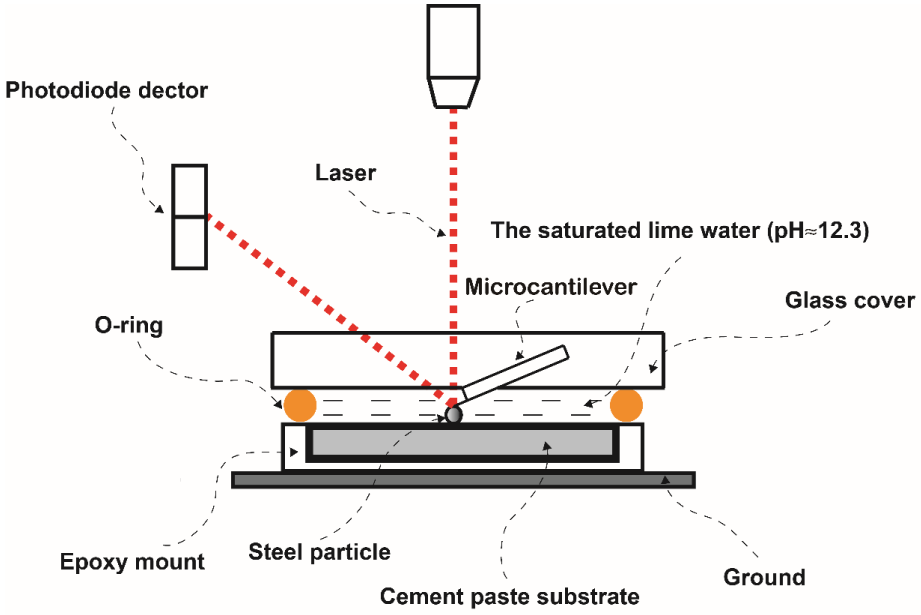

Figure 26: A schematic of particle probe scanning force microscopy in saturated limewater with major parts labeled.

5.1.4 Experimental design

In this study, adhesive forces between steel microspheres and early-hydrated cement substrates were measured using Nanoscope E (Bruker Inc., Santa Barbara, CA). All adhesion measurements were collected within 14 days after polishing the substrates. Adhesion measurements were collected in mapping matrices of 10 point × 10 point at the spacing of 15μm. The spacing was large enough to host the microsphere between adjacent grid points so that neighbor measurements were not affected by each other. Five force curves were collected at each point. Therefore, 500 measurements were collected between

one particle probe and one matrix. One matrix, i.e., 500 measurements, was obtained between the conventional SFM probe and the cement substrate in air, between the conventional SFM probe and cement substrate in saturated lime water, and between the particle probe and the cement substrate in air. To measure adhesion between the particle probes and the cement pastes in saturated lime water, three matrices, i.e., 1500 in total, were collected by interacting three particle probes with different locations of the same cement substrate. All data were measured at ~25.7 °C and ~30% relative humidity.

5.1.5 XRD analysis

XRD analysis was performed to elucidate the compositions of new and old cement specimens. Based on our facilities and time schedule, we prepared the new cement specimens using the solvent exchange method [184-186]. First, small cement pieces with weights of ~10 g were separated from the major cement bulk. New cement powders were placed in isopropanol for 2 days at ambient temperature followed by oven drying at 40˚C for 24h. Dried samples were carefully ground before X-ray diffraction analysis. Control specimens were also prepared by grinding new and old specimens directly. Powder diffraction patterns were collected on the MiniflexII Powder Diffractometer (Rigaku, The Woodlands, TX) with CuKα radiation. Scans were carried out from 5 to 90° (2θ) at 1° per minute. Experimental diffraction patterns were analyzed with the PDXL software (Rigaku, The Woodlands, TX).

5.1.6 Iceland spar specimens

As a comparison, adhesive forces were collected between steel and high purity calcium carbonate specimens. Some natural materials were made of calcium carbonate, such as sea shells [187-189] (aragonite and calcite) and Iceland spar (calcite) [190]. In this study, Iceland spar was selected since calcite was also found in the hydrated products of cement [191, 192]. The substrates of Iceland spar were prepared using the same procedure as those for cement substrates. Adhesive forces were collected between steel microspheres and Iceland spar substrates in saturated lime water, which were compared with those between steel and different hydrated products.

5.1.7 Synthesis of C-S-H

Adhesive forces were also collected between steel and synthetic C-S-H gels in saturated lime water. Synthetic C-S-H gels [193, 194] were prepared by reacting calcium oxide and silica in the aqueous phase in a nitrogen environment. The calcium oxide was obtained from Sigma (Sigma-Aldrich, St. Louis, MO). The suspension of colloidal silica in water from Sigma (Sigma-Aldrich, St. Louis, MO) possessed a nominal silica content of 50%. The actual silica content of the suspension was measured as 58.5 wt% based on the weight loss by drying at 120˚C. The synthetic C-S-H gels were prepared at two different Ca/Si ratios of 0.8 and 1.4, the details of which were summarized in Table 11.

Table 11: Synthesis of C-S-H gels.

Mass of CaO (g)	Mass of silica suspension (g)	Estimated H2O content (g)	Ca/Si in gel
30.0	68.6	19.3	0.8
30.0	39.2	19.3	1.4

C-S-H specimens were stored in the nitrogen atmosphere for three months before adhesive force measurements. We understand that there are differences between the synthetic C-S-H gels and the C-S-H formed in the cement hydration. Adhesive forces collected between steel and synthetic gels were used to compare with those between steel and different hydrated products.

5.1.8 Electron probe microanalysis

Electron probe microanalysis [195, 196] is a method to analyze the chemical compositions of samples at the location where the electron beam is irradiated by collecting the wavelength and intensity of the characteristic X-rays. A Cameca SX 100 electron microprobe operated at 15 kV was used to collected composition data from the samples, including Na_2O, MgO, SiO_2, SO_2, K_2O, CaO, FeO, and Al_2O_3. Both new and old samples were impregnated with resin, polished to 250 nm finish and carbon-coated before measurements. Maps of 200 μm × 200 μm were obtained at the fixed step of 2 μm, whereas the analyzed spot diameter was 5 μm. Wavelength dispersive spectroscopic (WDS) maps of MgO, SiO_2, CaO, FeO, and Al_2O_3 were collected, whereas energy dispersive spectroscopic (EDS) maps of Na_2O, SO_2, K_2O were collected. For each sample, a grid of 8 × 8 at the spacing of 10 μm, i.e., 64 points in total, were scanned to collect the weight percentages of different compositions, which were used to estimate the fractions of different phases in the cement specimens. The scan of each grid took approximate two hours.

5.2 Modeling

For the data of adhesion between cement and steel, the mixed Gaussian model and hydration model were used to analyzed.

5.2.1 Mixed Gaussian models

Heterogeneous populations of different phases in the cement paste could complicate the interpretation of adhesion measurements. Adhesive force measurements between steel and cement substrates are highly dependent on the hydrated phases in the cement substrate. Thus, it is crucial to separate different phases to obtain their own adhesive forces. In the mixed Gaussian model [197, 198], it is assumed that the frequency densities of adhesive forces could be described by a superimposed Gaussian distribution consisting of independent normal distributions for each phase. The force distribution of each phase R is approximated by:

$$p_R(x) = \frac{1}{\sqrt{2\pi S_R^2}} \exp\left(-\frac{(x-\mu_R)^2}{2S_R^2}\right) \tag{5}$$

where x is the set of adhesive forces measured between steel microspheres and cement substrates, μ_R and S_R are the arithmetic mean and standard deviation of adhesive forces in each phases, respectively. In this study, the best fit is achieved when the standard error between the experimental measurements and predictions is minimized within the area constraints, given by

$$min \sum_{i=1}^{m} \frac{(P_i - P(x_i))^2}{m} \quad \text{s.t.:} \sum_{R=1}^{n} f_R = 1 \tag{6}$$

where P_i is the measured frequency density of adhesive forces, $P(x_i) = \sum_{R=1}^{n} f_R p_R(x_i)$ is the summed value of the theoretical probability densities at point x_i. m is the number of bins in the histograms. N_R is the number of measurements for each phase, and $f_R = N_R/N$ is the area fraction of phase R in the measurement matrices.

5.2.2 The cement hydration model

Different models on the cement hydration have been proposed to reveal the hydration mechanisms [199-203]. In this study, the hydration model based on the stoichiometry equations [199, 200] was used to roughly estimate the area fractions of different hydrated products. It should be noted that this hydration model only assumes the homogenous nucleation and growth, and isotropic morphologies of the hydrated products. The reactants are alite (Ca_3SiO_5: C_3S), belite (Ca_2SiO_4: C_2S), tricalcium aluminate ($Ca_3Al_2O_6$: C_3A) and ferrite ($Ca_4Al_2Fe_2O_{10}$: C_4AF). The hydrated products are separated into five groups, including the low-density calcium silicate hydrate (LD C-S-H), the high-density calcium silicate hydrate (HD C-S-H), other hydrated products [ettringite ($C_6A\bar{S}_3H_{32}$), AFm ($C_4A\bar{S}H_{12}$), hydrogarnet ($C_3(A,F)H_6$), and calcium aluminate hydrate (C_4AH_{13})], calcium hydroxide (CH), and unreacted components. Fig. 27 shows the relationship between the degree of hydration and relative volume of phases as predicted by the hydration model with water/cement ration is 0.5.

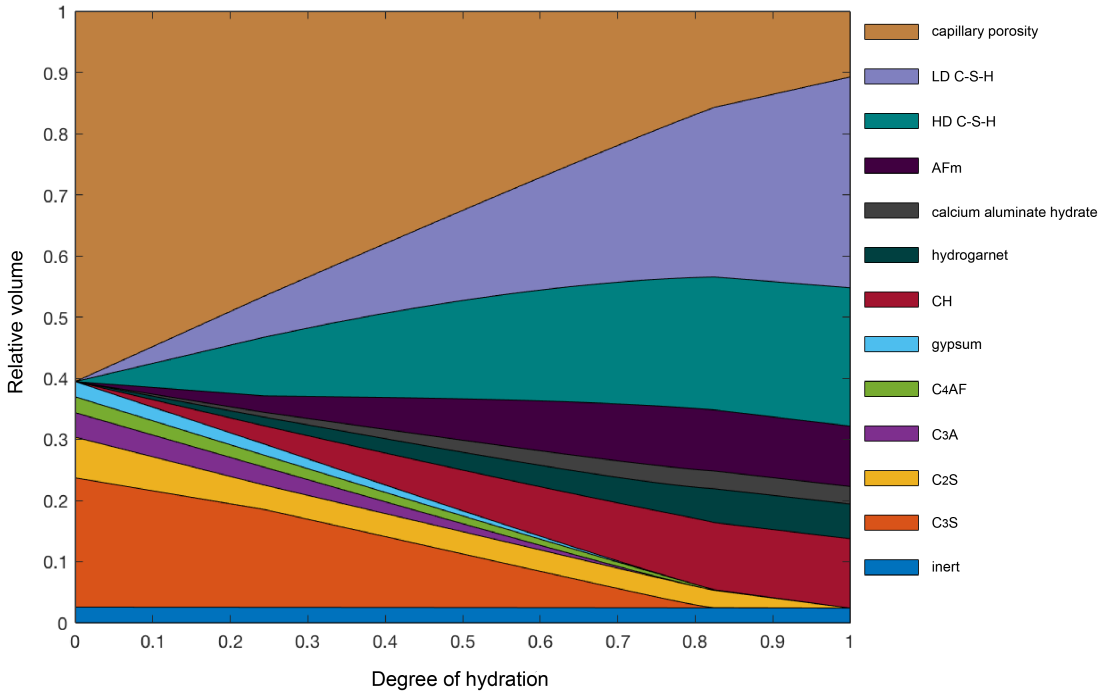

Figure 27: Relative volume of phases (as predicted by the hydration model) as a function of the degree of hydration (water/cement ratio of 0.50).

Given the type I/II cement and the water:cement ratio, the area fractions of different hydrated products were determined using the chemical and kinetic equations. The weight percentages of different reactants were C_3S (55%), C_2S (18%), C_3A (10%) and C_4AF (8%) [183]. The hydration equations [200] are given by

$$2C_3S + 10.6H \rightarrow C_{3.4} - S_2 - H_8 + 2.6CH \quad (7)$$

$$2C_2S + 8.6H \rightarrow C_{3.4} - S_2 - H_8 + 0.6CH \quad (8)$$

$$C_3A + 3C\bar{S}H_2 + 26H \rightarrow C_6A\bar{S}_3H_{32} \quad (9)$$

$$2C_3A + C_6A\bar{S}_3H_{32} + 4H \rightarrow 3C_4A\bar{S}H_{12} \quad (10)$$

$$C_3A + CH + 12H \rightarrow C_4AH_{13} \quad (11)$$

$$C_4AF + 2CH + 10H \rightarrow 2C_3(A,F)H_6 \quad (12)$$

For the kinetic equations, the reaction rates are estimated by the Avrami equations [204]

$$\alpha_j = 1 - \exp\left[-a_j\left(t - b_j\right)^{c_j}\right] \quad (13)$$

where α_j is the degree of hydration of compound j at time t (in days); a_j, b_j, and c_j are constants obtained using a specific Portland cement [191, 204]. Fig. 28 shows the relationship between aging time and degree of reactions for reactants, including C_3S, C_2S, C_3A and C_4AF.

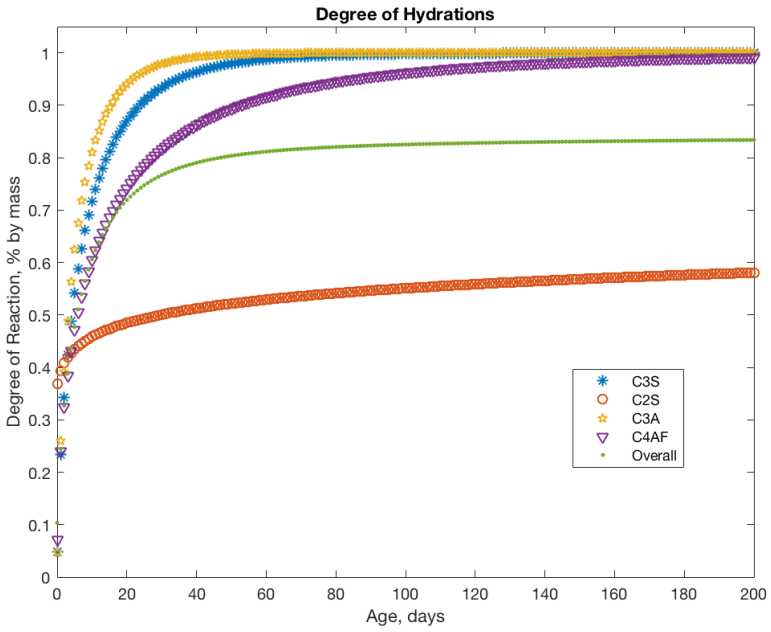

Figure 28: Relationship between aging time (days) and degree of reactions (% by mass).

The constants of reaction rates used in this study are summarized in Table 12. The materials properties of various hydrated products are summarized in Table 13.

Table 12: Constants used in the Avarmi equations [185, 198].

Compound *i*	*a*	*b*	*c*
C_3S	0.25	0.70	0.90
C_2S	0.46	0.12	0
C_3A	0.28	0.77	0.90
C_4AF	0.26	0.55	0.90

Table 13: Material properties used in the cement hydration model [199].

Compound	Nominal formula	Density (kg/m^3)	Molecular weight (kg/mol)
Alite	C_3S	3150	0.228
Belite	C_2S	3280	0.172
Aluminate	C_3A	3030	0.270
Ferrite	C_4AF	3730	0.486
Water	H_2O	998	0.018
Gypsum	$C\bar{S}H_2$	2320	0.172
Calcium hydroxide	CH	2240	0.074
Hydrogarnet	$C_3(A,F)H_6$	2670	0.407
AFm, saturated	$3C_4A\bar{S}H_{12}$	1990	0.623
AFt , saturated	$C_6A\bar{S}_3H_{32}$	1750	1.255
Calcium aluminate hydrate	C_4AH_{13}	2050	0.560
LD C-S-H, dried	$C_{3.4}S_2H_3$	1440	0.365
HD C-S-H, dried	$C_{3.4}S_2H_3$	1750	0.365

Capillary pores are important to mechanical properties of the hydrated products. In this study, capillary pores were assumed to be evenly distributed among five different groups of hydrated products based on the area fractions. In the meantime, the mass ratio between LD C-S-H and HD C-S-H is critical to the hydrated products. The ratio, i.e., M_r, is an average based on the regressive models proposed in prior studies [199, 200], given by

$$M_r = \frac{1}{2}\left(M_{r1} + M_{r2}\right) \tag{14}$$

Where

$$M_{r1} = 3.017\left(\frac{w}{c}\right)\alpha - 1.347\alpha + 0.538 \quad (15)$$

$$M_{r2} = 2.2096\left(\frac{w}{c}\right)\alpha - 0.6683\left(\frac{w}{c}\right) - 0.7607\alpha + 0.4031 \quad (16)$$

M_{r1} and M_{r2} are progressive models in the references [199, 200], *w/c* is the water:cement ratio, and α is the total degree of hydration.

5.3 Results and discussion

5.3.1 Steel particle probes for scanning force microscopy

The particle probes were examined using a scanning electronic microscope (JEOL JSM 6060, Peabody, MA) to ensure their quality. A representative steel particle probe is shown in Fig. 29a, in which the steel microsphere is well attached on the free end of the cantilever. The diameters of steel microspheres measured through the SEM image analysis were 12.94 ± 1.28 μm (Table 14). Spring constants of the particle probes measured using the thermal tuning method [163, 164] were 1.60 ± 0.01 N/m (Table 15). A commercial silicon based SFM probe (NanoAndMore, Watsonville, CA) is shown in Fig. 29b. The sharp radius of the pyramid probes exhibit a substantially smaller contact area compared to that of the steel microsphere probe.

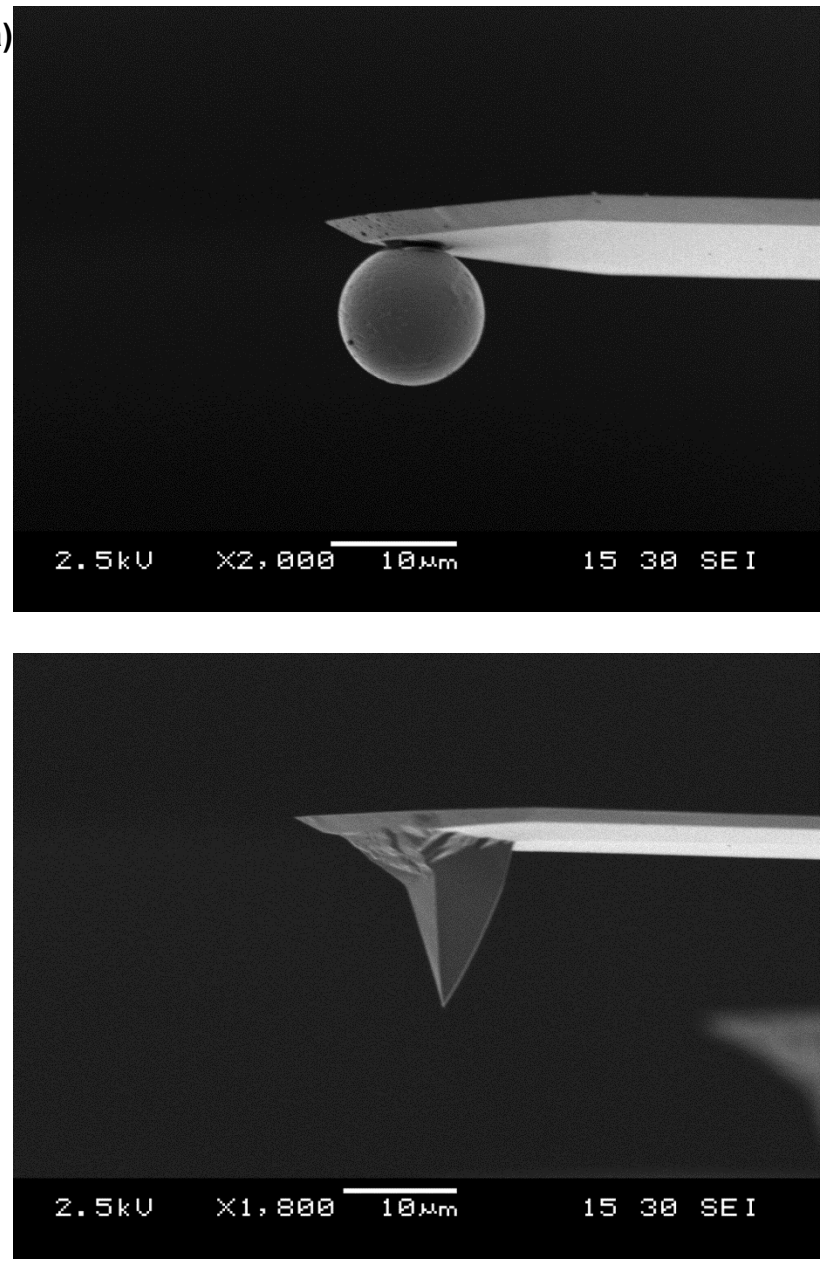

Figure 29: SEM images of (a) a microcantilever with a steel microsphere fabricated in this study (particle tip). (b) A commercial silicon SFM probe with nanoscale radius (bare tip).

Table 14: Summary of spring constants and spherical diameters used in this study.

	Bare probe		**Particle probe**			
	Air	Lime water	Air	Lime water Sphere 1	Lime water Sphere 2	Lime water Sphere 3
Spring constant (N/m)	0.65	0.65	1.60	1.59	1.60	1.62
Diameter (μm)	-	-	11.20	13.58	12.82	14.15

5.3.2 Cement paste substrates

The surface morphology of the polished cement paste is characterized by conventional SFM probes. A representative scanner surface of 20μm × 20μm is shown in Fig. 30. The surface is flat with evenly distributed grain patterns, for which the root mean square (RMS) of the substrate surface roughness was ~60 nm. Therefore, the surface is smooth enough to enable good contact between the steel microspheres and the cement substrates at microscale.

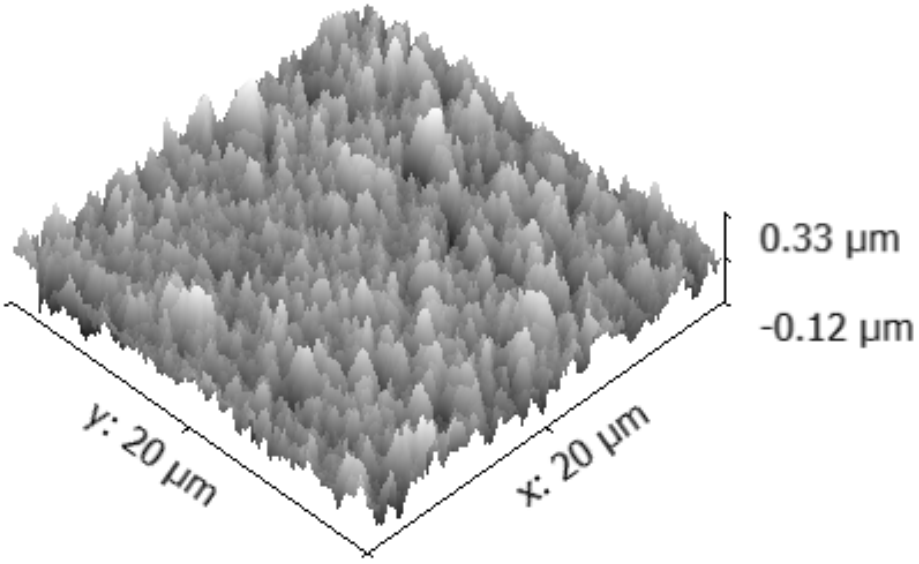

Figure 30: The surface morphology of a representative polished cement paste substrate.

5.3.3 Force curves

A representative force curve between a steel microsphere and an early-hydrated cement substrate in saturated lime water is shown in Fig. 31. The vertical axis was a measure of the reflected signal from the back of cantilever in arbitrary unit, and the horizontal axis was the z-travel of the tip in nm. As the tip approached surface (the red curve), the curve was initially flat since the microsphere did not contact the substrate. Once the probe contacted the substrate, the reflected signal increased linearly when the cantilever was continuously driven forward. In retracting, the cantilever bent reversely after the contact point so the signal decreased with the same slope. The microsphere did not disengage from the substrate until the restoring force of the cantilever overcame the adhesion between the steel microsphere and the cement substrate. After that, the signal became flat again since the microsphere disengaged from the substrate surface. Δx was the travel distance of probe between the contact point and the disengage point.

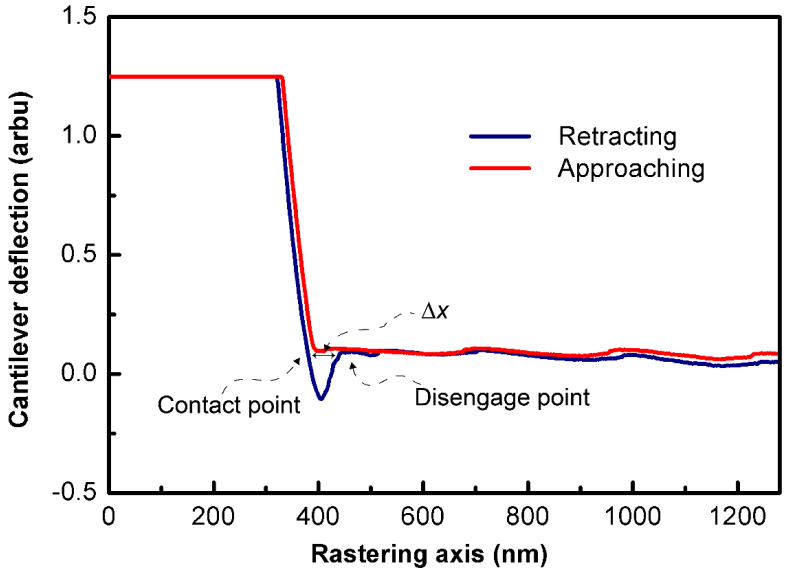

Figure 31: A representative force curve between a steel microsphere and an early-hydrated cement substrate in saturated lime water. The rastering axis is the traveling axis along which the microcantilever moves.

5.3.4 Adhesion between steel microspheres and early-hydrated cement substrates

Since conventional SFM probes made from silicon or silicon nitride possess nanoscale radii, the steel particle probes are more suitable to investigate microscale interactions between steel and cement phases. As a comparison, it is of interest to the adhesive forces measured using conventional SFM probes in air and in saturated lime water. Statistical results of adhesive forces measured at different conditions were summarized in Fig. 32a, including the bare tip in air, the bare tip in lime water, the steel particle probe in air and the steel particle probe in lime water. Each box included 500 measurements in one 10 × 10 matrix described in the prior section. Thus, the steel microsphere in lime water included 1500 measurements obtained from three matrices. Diamond symbols were outliers beyond the upper fence, i.e. 1.0 times the interquartile range.

In general, adhesive forces measured between bare tips and cement substrates are smaller than those measured between steel microspheres and cement substrates in both air and lime water. This is because contact areas between steel microspheres and cement substrates are larger than the contact areas between bare tips and substrates. For measurements using bare tips, adhesive forces in air are slightly larger than those measured in lime water. Similar trends exist for measurements between steel microspheres and cement substrates. This is probably because the capillary bridges formed by water meniscus [205, 206] contributed to the adhesive forces between the probe and substrate in air, while they do not exist when operating SFM in lime water. The average values of adhesion measurements (Fig. 32b) further consolidated these trends. The mean value of adhesive forces between steel microsphere and cement substrates is ~35 nN in saturated lime water. For measurements using steel microspheres, consistent adhesive forces are measured for all matrices (Fig. 32b), proving that the particle probe method is reliable in quantifying adhesive forces under hydrated conditions.

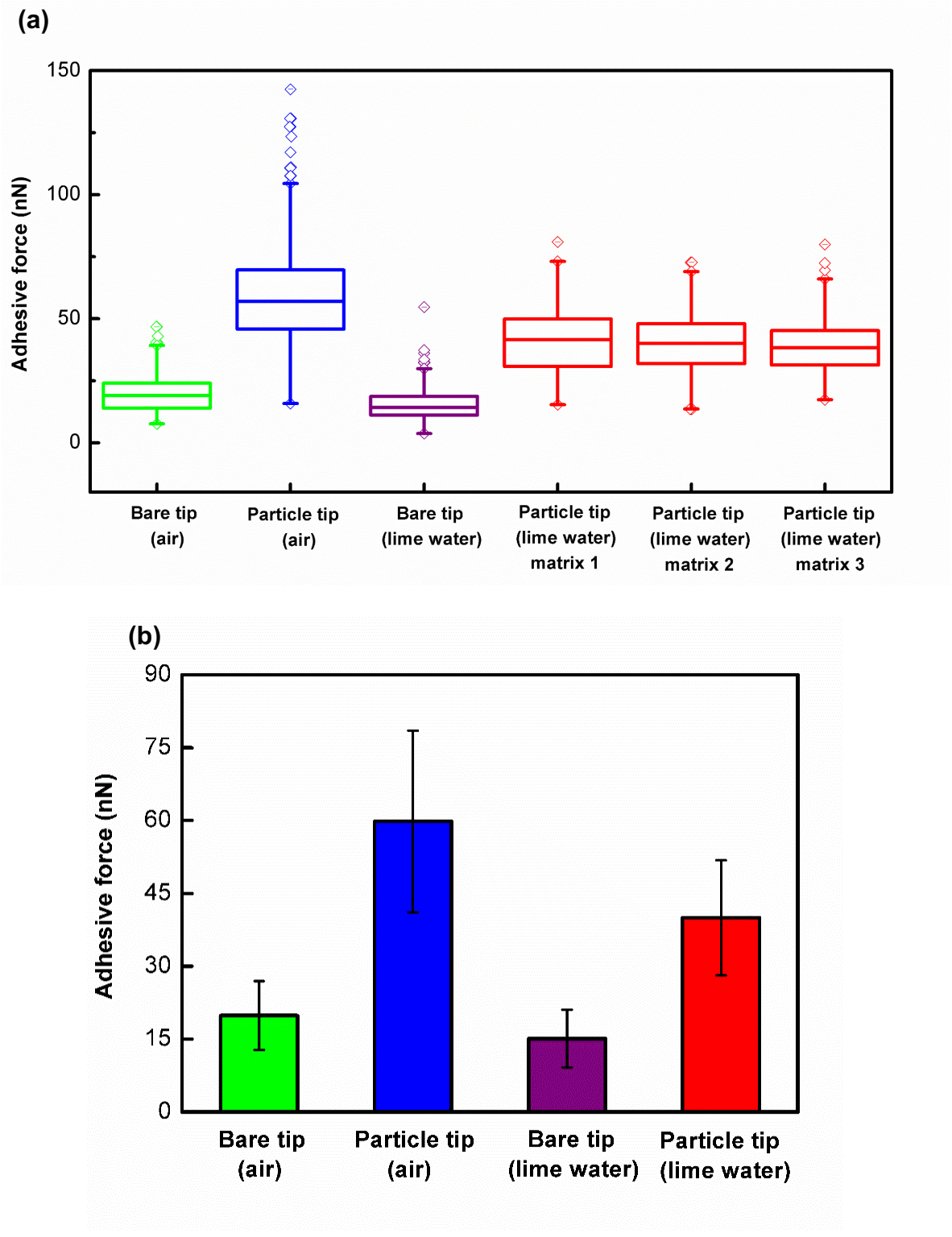

Figure 32: Adhesive forces of different interaction pairs: (a) Box plots with whiskers in which diamonds are outliers. (b) Average values with error bars.

5.3.5 Adhesion contours

2D-contours of adhesion measurements between steel microspheres and cement pastes in satureated lime water are shown in Fig.33. Results demonstrated that consistent adhesive force contours were obtained for all matrices. Most areas exhibit adhesion values between 30 to 60 nN. For areas with adhesion values smaller than 30 nN, i.e., the black areas, both islands and continuous strips were found within the matrices. However, areas with adhesion values larger than 60 nN distributed only as islands in all three matrices.

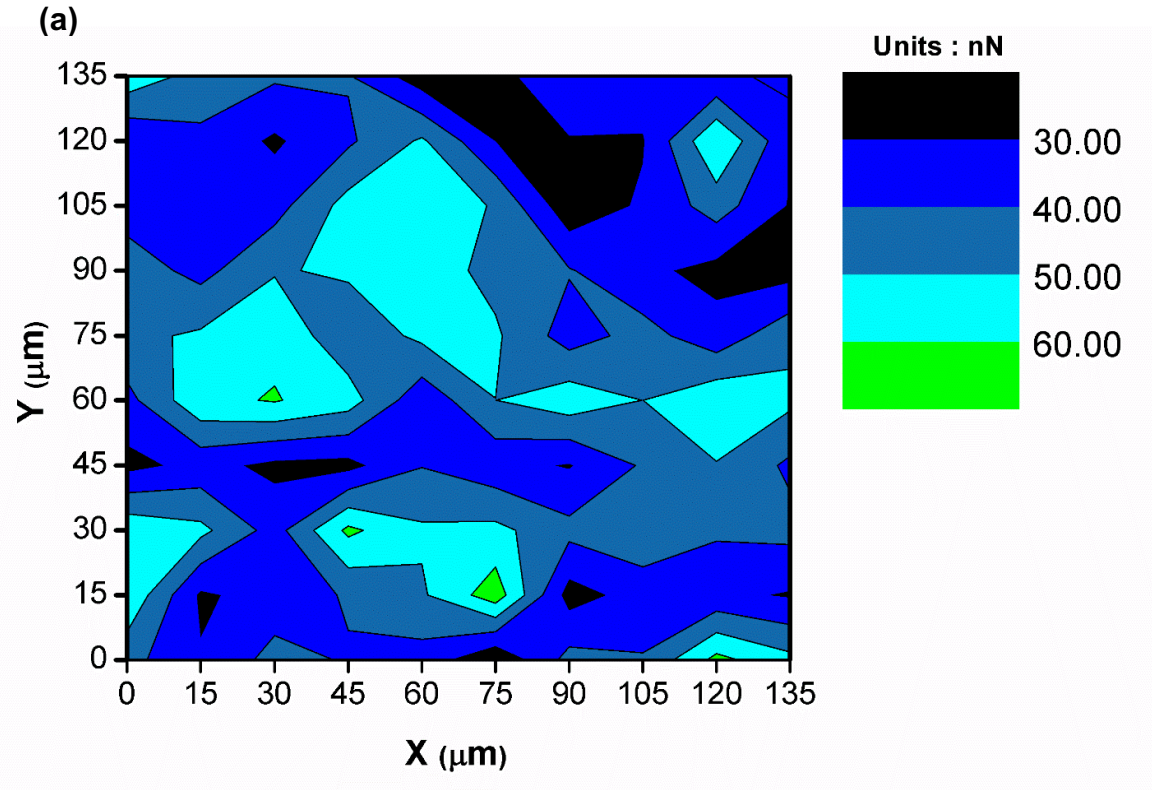

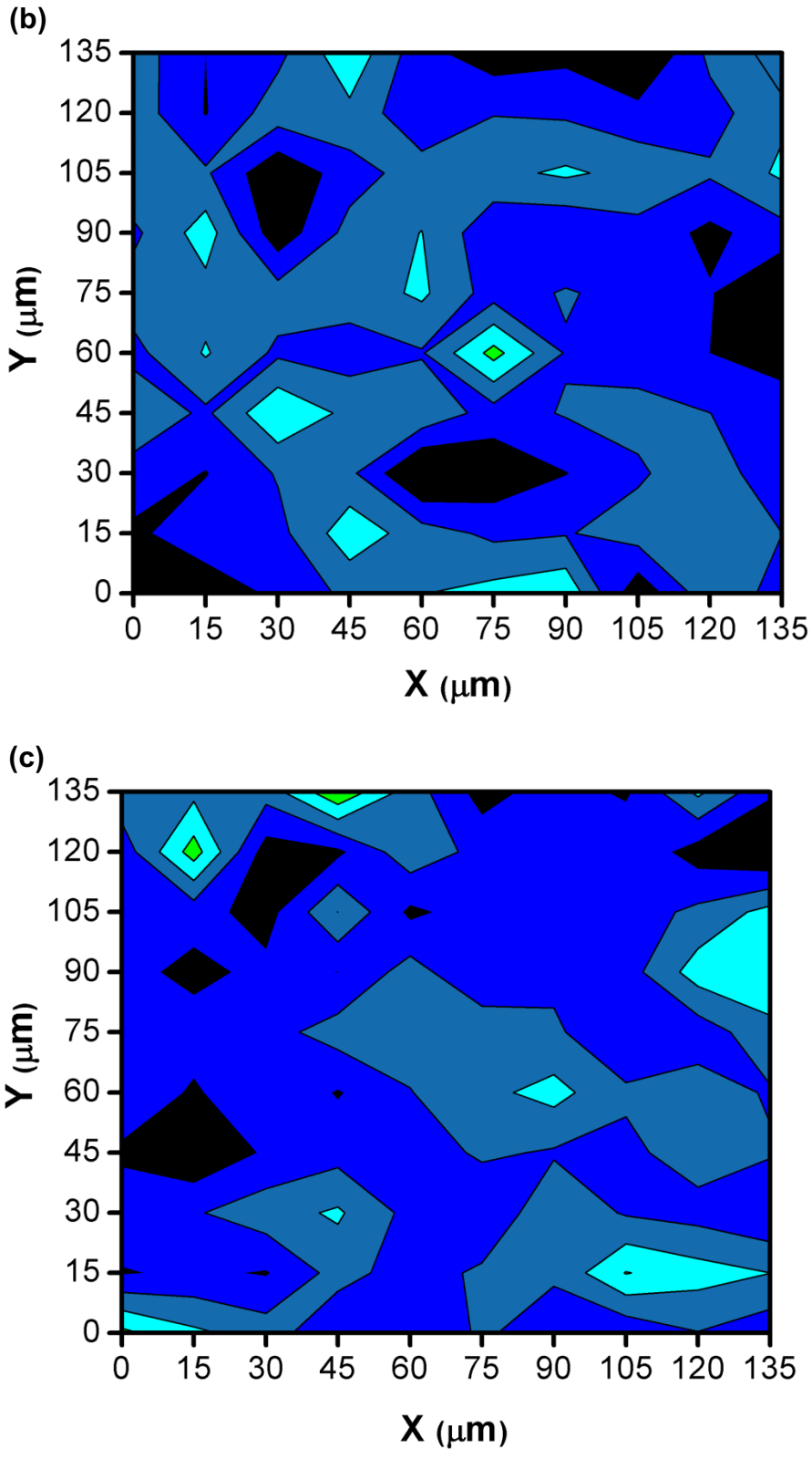

Figure 33: Contours of adhesion measurements (a) Matrix 1. (b) Matrix 2. (c) Matrix 3.

To characterize the elemental distributions on the cement substrate surface, Energy-dispersive X-ray spectroscopic (EDS) analysis was performed. The results were summarized in Fig. 34. It can be seen that the distributions of oxygen, calcium and silicon elements (Figs. 34a, 34b and 34c) are widely spread over the entire matrix. However, the aluminum elements (Fig. 34d) exhibit localized distributions with relatively higher intensity.

(a)

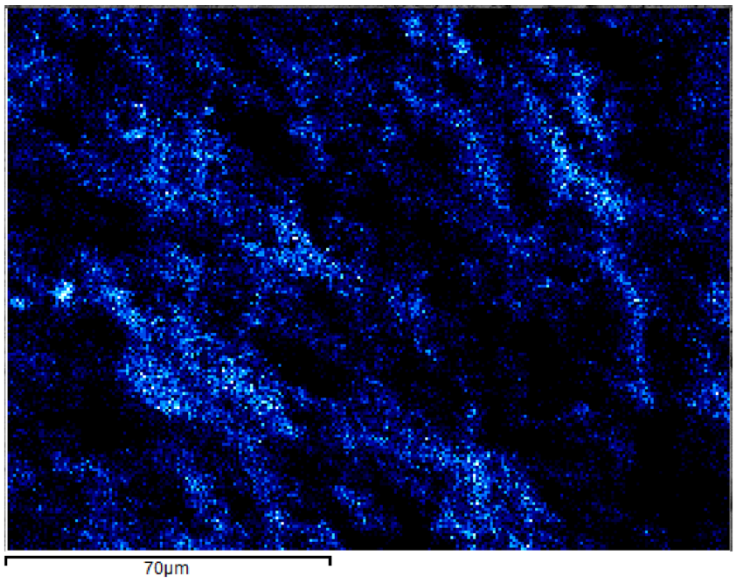

(b)

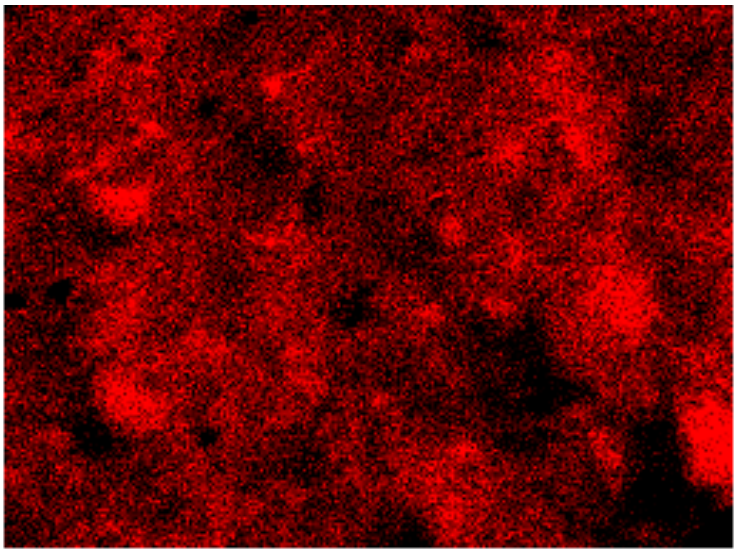

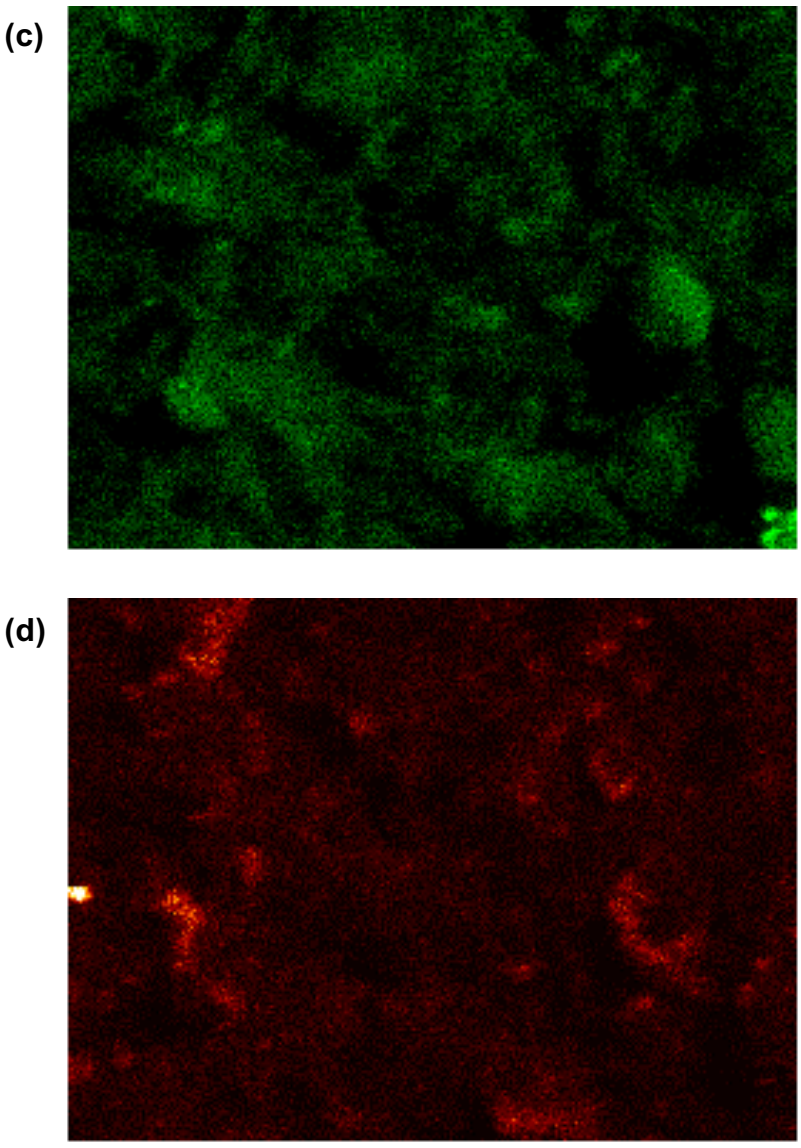

Figure 34: Element distributions of (a) Oxygen. (b) Calcium. (c) Silicon. (d) Aluminum.

5.3.6 Mixed Gaussian distributions of adhesion measurements

Adhesion measurements in the three matrices between steel microspheres and cement substrates in saturated lime water were further analyzed using the mixed Gaussian models. Histograms of frequency densities measured experimentally from the 500 adhesion measurements in each matrix were shown in Figs. 35a to 35c. Then, the total of

1500 measurements in three matrices were plot together in Fig. 35d. The bin size of 17 was used for all plots. Mixed Gaussian distributions were extracted based on the collections of five one-dimensional normal distributions. Each peak represented one phase through which the corresponding adhesive force is determined. The combination of five Gaussians curves agreed well with the experimental frequency densities of adhesive forces.

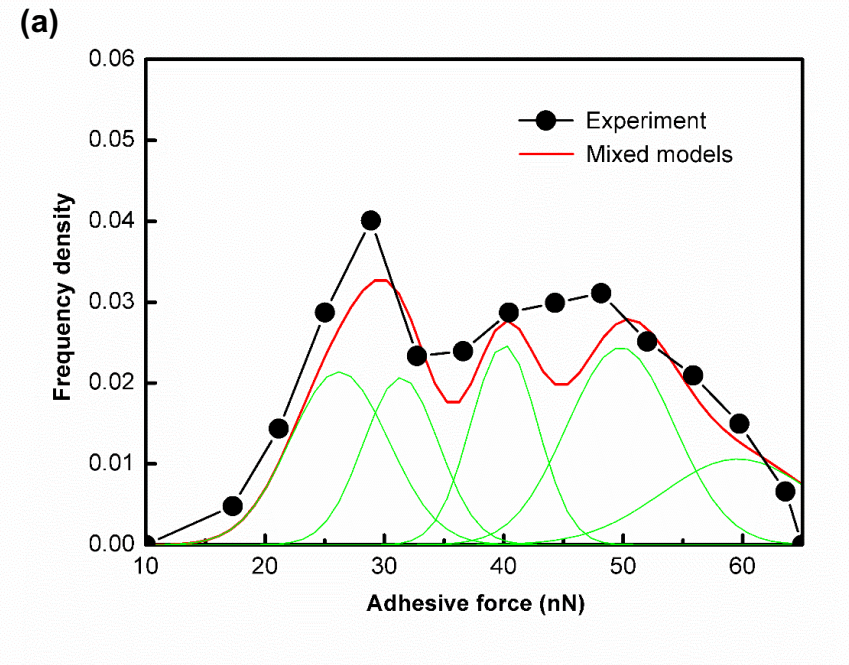

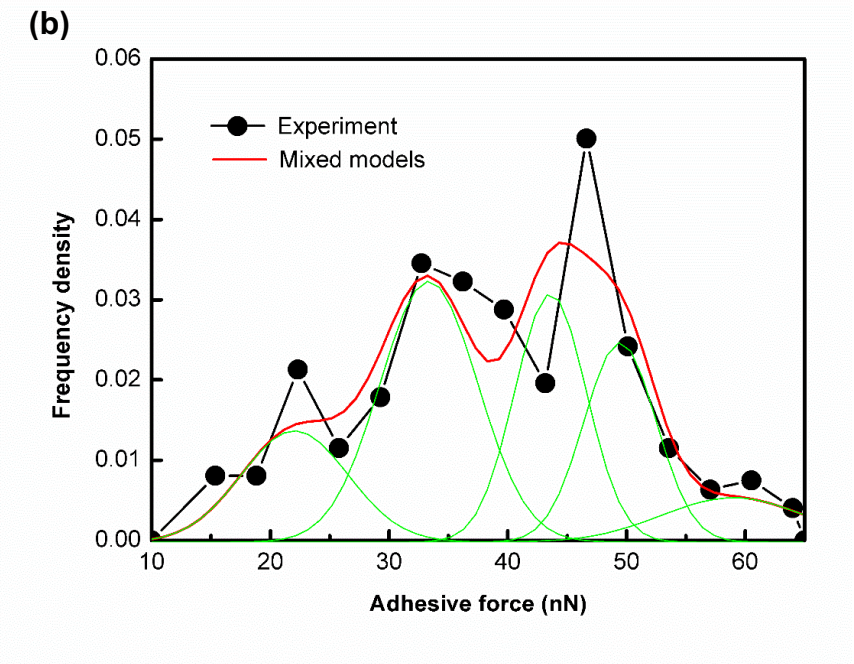
(b)
Experiment
Mixed models
Frequency density
Adhesive force (nN)
0.00
0.01
0.02
0.03
0.04
0.05
0.06
10
20
30
40
50
60

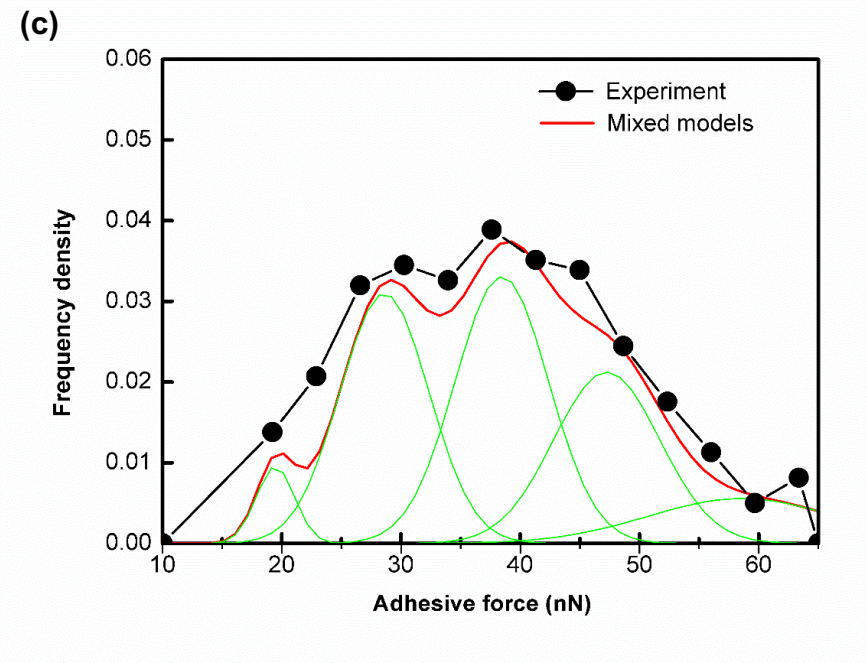
(c)
Experiment
Mixed models
Frequency density
Adhesive force (nN)
0.00
0.01
0.02
0.03
0.04
0.05
0.06
10
20
30
40
50
60

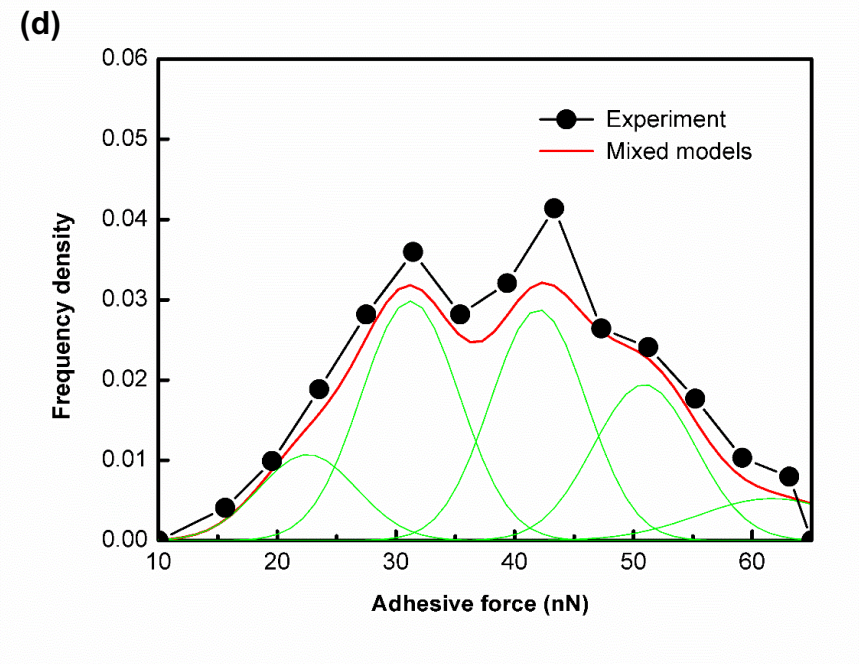

Figure 35: Frequency densities and mixed Gaussian modeling of adhesion measurements between steel microspheres and cement substrates in saturated lime water (a) Matrix 1. (b) Matrix 2. (c) Matrix 3. (d) Three matrices combined.

The parameters of mixed Gaussian distributions were summarized in Table 15, including mean values, standard deviations and weights of five phases. In general, the mean values of adhesive forces are consistent among different matrices. However, the weight percentages varied substantially from matrix to matrix. This is because locations of matrices affect the adhesion distributions. In this study, adhesion measurements of three matrices were combined to further elucidate the phase distributions of the cement substrate. Overall, cement pastes were composed of five phases with local variations of weight percentages.

Table 15: Summary of predictions by the mixed Gaussian models.

	Phase	CH	LD C-S-H	HD C-S-H	Others	Unreacted
Matrix 1	μ_i (nN)	26.2	31.4	40.0	49.8	59.6
	σ_i (nN)	4.1	3.2	2.8	4.5	6.3
	f_i (%)	22.0	16.4	17.3	27.4	16.8
Matrix 2	μ_i (nN)	22.0	33.3	43.6	49.5	59.0
	σ_i (nN)	4.5	4.1	3.0	3.0	6.0
	f_i (%)	15.6	33.6	23.4	19	8.4
Matrix 3	μ_i (nN)	19.5	28.6	38.5	47.3	58.5
	σ_i (nN)	1.6	3.7	3.9	4.4	7.9
	f_i (%)	3.8	29.0	32.5	23.7	11.0
All	μ_i (nN)	22.6	31.2	42	50.9	61.7
	σ_i (nN)	4.1	4.1	4.0	4.3	6.2
	f_i (%)	11.0	31.0	29.0	20.9	8.1

5.3.7 Comparison between experimental data and hydration modeling

To determine the phase types, volume fractions of different hydrated products were compared with predictions from the hydration model. In Fig. 36, volume fractions were listed based on groups defined in section 5.2.2, i.e., LD C-S-H, others, HD C-S-H, CH and the unreacted components. Two sets of experiment data were included in the plot. The first set in circular symbols was based on adhesion measurements between steel microspheres and early-hydrate cement (type I/II) collected in this study. The second set in diamond symbols was based on modulus and hardness measurements using nanoindentation in references [198, 207, 208]. The hydration model predicts a spectrum of volume fractions based on the degree of hydration ranging from 0.6 to 0.9. As the hydration degree increases, the volume fraction of the unreacted components decreases substantially.

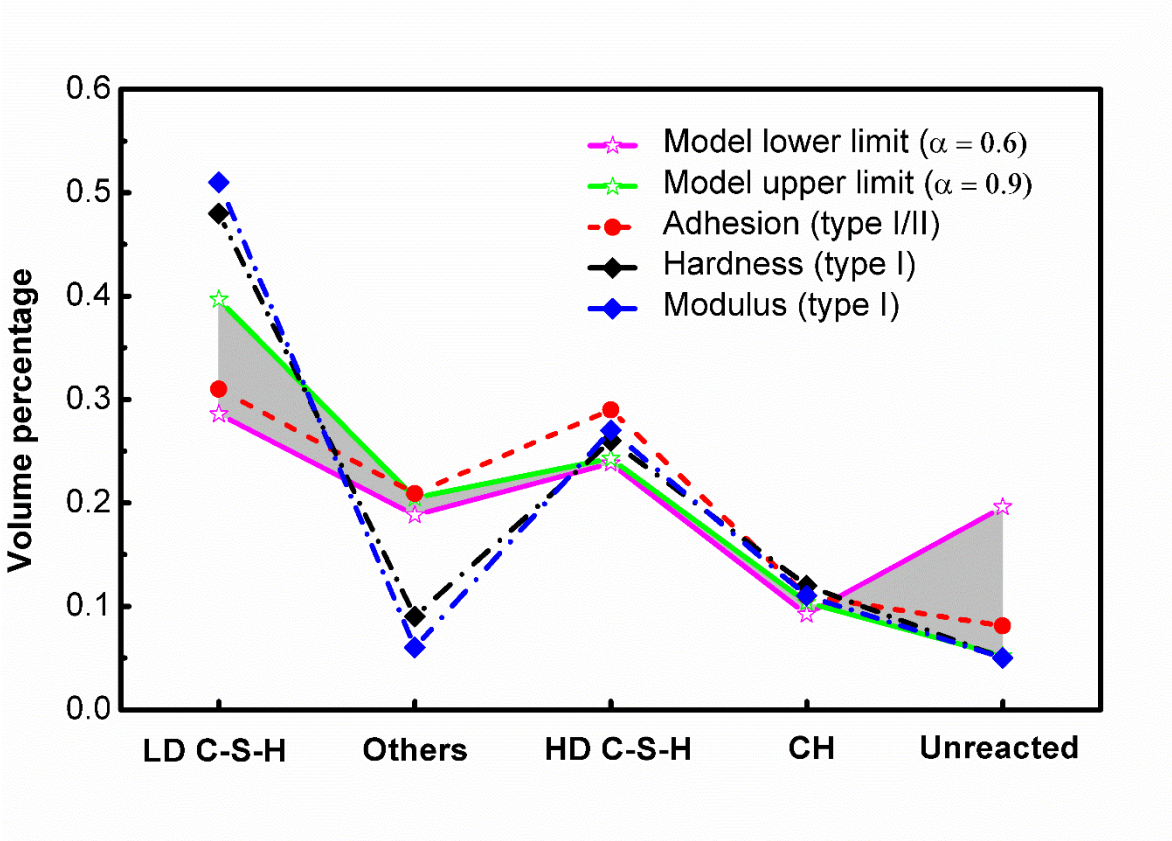

Figure 36: Comparison between the experimental data and predictions from the hydration model. The degree of hydration, α, ranges from 0.6 to 0.9. Adhesion data were based on early-hydrated type I/II cement substrates. Hardness and modulus data were collected on six-month old substrates from type I cement [198].

Consistent correlations were obtained between adhesion measurements and predictions from the hydration model for LD C-S-H, others, CH and unreacted components. For the HD C-S-H group, predictions from the hydrations model were smaller than experimental results based on adhesion measurements since the estimated HD C-S-H volume depends on the mass ratio between the LD C-S-H and HD C-S-H. Meanwhile, experimental data based on nanoindentation results [198, 207, 208] agreed well with predictions from the hydration model for the HD C-S-H, CH and unreacted components. Different volume fractions are obtained for LD C-S-H and others between the adhesion

tests and nanoindentations. This is probably because four-week old type I/II cement specimens were used for the adhesion tests, whereas six-month old type I cement specimens were used to collect the nanodentation data [198]. In general, consistent correlations were obtained for volume fractions between the adhesion measurements and estimations from the hydration model.

5.3.8 Adhesion of different early-hydrated products

Adhesive forces between steel and different phases of the early-hydrated cement paste were shown in Fig. 37. Adhesive forces between steel microspheres and the groups of LD C-S-H, HD C-S-H and other hydrated products are intermediate, ranging from 30 to 50 nN (mean values). This is consistent with the 2D-contours of adhesive forces shown in prior, in which large areas exhibit adhesive forces ranging from 30 to 60 nN (lower and upper bounds). This is because the total volume of LD C-S-H, HD C-S-H and other hydrated products occupies a signification portion (~71%) of the matrix areas. LD C-S-H exhibited slightly smaller adhesive forces than those of HD C-S-H. This is probably because the more porous microstructure of LD C-S-H [201] leads to less effective contact areas to steel microspheres, resulting in smaller adhesion than that of HD C-S-H.

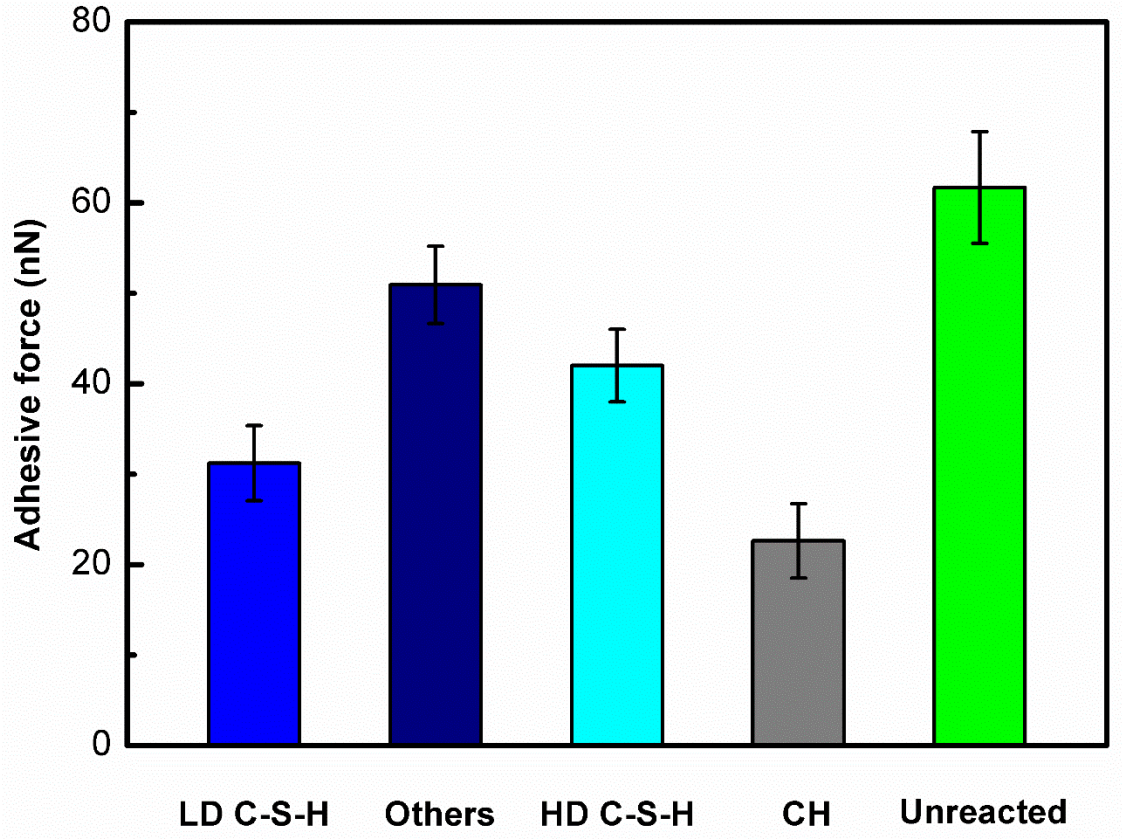

Figure 37: Adhesive forces of different phases in the early-hydrated cement.

The adhesion between CH and steel microspheres (~22 nN) is smallest among all groups. According to the reference [209], it can be assumed that steel is oxidized and hydrolyzed to some extent, and oxygens might be free to form hydrogen bonds with the hydrogen end groups of CH phase, but ferrous surface may favor acid-based bonding. Also because of the discontinuous nature of cement and imperfection in crystal. The hexagonal lamellar structure of CH phase is possible reason for smallest adhesive forces. The unreacted cement, which is less than 10% in volume fraction, exhibit the largest adhesion (~ 61 nN) to the steel microspheres. We postulate that these spots are related to the clinker liquid phase. In the burning zone, 20-30% liquid forms for most commercial clinkers. Their high surface tension helps bind the particles together, which is critical to nodule formation

and clinker quality [209]. As illustrated in the contours, spots exhibiting large adhesion (>60 nN) are distributed as isolated areas. Thus, small clusters that are rich in the cooled and solidified liquid phase may still preserve amorphous constituents exhibiting high adhesion to steel microspheres. Future research is needed to elucidate these high adhesion areas in early-hydrated cement.

5.4 Conclusions

In this chapter, particle probe scanning force microscopy was used to measure the adhesion between steel microspheres and the early-hydrated cement. First, steel particle probes were fabricated by attaching steel microspheres to the free ends of microcantilivers. The adhesive forces between steel microspheres and cement pastes were measured in air and in saturated lime water. As a comparison, conventional silicon SFM probes were used to measure the adhesive forces to cement paste in corresponding conditions. In general, adhesive forces measured using the particle probes are larger than those measured using SFM probe. This is because larger contact areas between the steel microspheres and cement substrates lead to greater adhesive forces. Due to the capillary bridges, adhesive forces measured in air are greater than those measured in lime water for both particle and conventional probes.

Consistent contours were obtained for all matrices between steel microspheres and cement substrates in saturated lime water. Adhesive forces mostly range from 30 to 60 nN. Some islands exhibit adhesive forces greater than 60 nN; while other areas exhibit adhesive forces less than 30 nN. The estimated volume fractions from the hydration model reasonably capture the data trends in the adhesion tests. Based on these results, several

groups were deconvoluted, i.e., LD C-S-H, HD C-S-H, CH, other hydrated products and the unreacted components. Results showed that LD C-S-H, HD C-S-H and other hydrated products exhibit intermediate adhesive forces among all groups. LD C-S-H exhibit slightly smaller adhesion than HD C-S-H possibly because its more porous microstructures do not enable contact to steel microspheres as effectively as that of HD C-S-H. CH exhibits the smallest adhesive forces showing that the irregular sheets in the microstructure did not promote their contact to steel microspheres. The unreacted components exhibit the largest adhesive forces. It is postulated that the isolated adhesive peaks are related to the solidified liquid clinker phases with high surface tension. More work is needed to elucidate the areas with large adhesive forces.

CHAPTER 6: COMPARISON OF ADHESION BETWEEN STEEL AND EARYLY-HYDRATED / SIX-MONTH CURED CEMENT

This chapter summarized the experimental results for six-month cured cement (old) using PPSFM and EPMA and deconvolution results using mixed Gaussian distributions.

6.1 Results

6.1.1 Steel particle probes for scanning force microscopy

It is important to ensure good steel particle probes are created before collecting adhesive forces between cement substrates and probes. A representative microspherical steel probe for six-month cured cement is shown in Fig. 38a. The steel microsphere is well attached to the free end of the bare microcantilever, enabling a good contact between the microsphere and the substrate surface. As a comparison, a conventional SFM silicon nitride probe was shown in Fig. 38b, in which the pyramid probe has a nanoscale radius. A summary of the spring constants and the spherical diameters are summarized in Table 16. It can be seen that different particle probes have consistent spring constants and particle diameters.

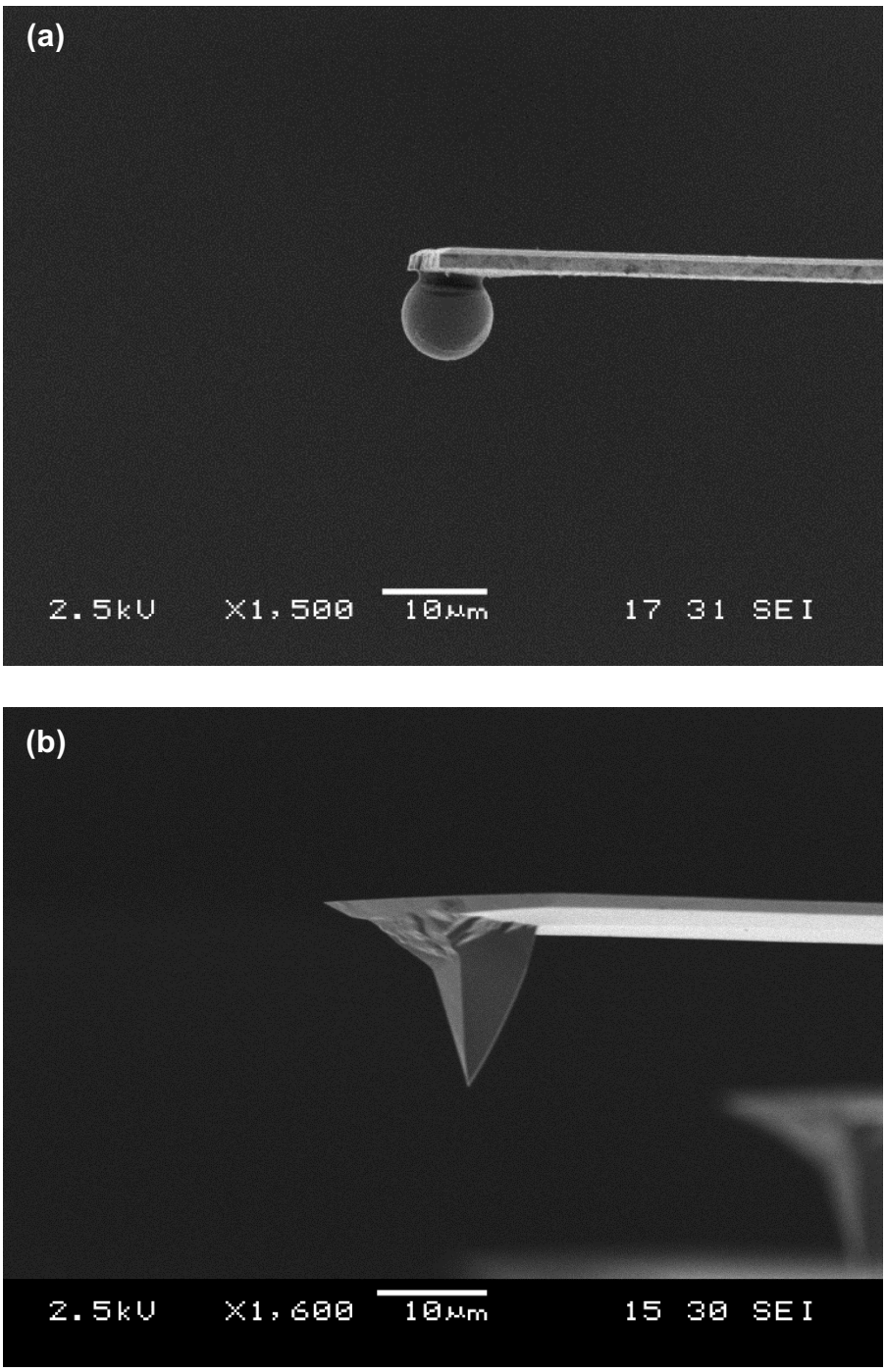

Figure 38: SEM images of (a) a particle probe with a steel microsphere attached to the free end of a microcantilever (particle probe). (b) A conventional silicon nitride SFM probe with a nanoscale radius (bare probe).

Table 16: Summary of spring constants and probe diameters used in the adhesive measurements.

Properties	**Bare probe (Si_3N_4)**		**Particle probe (Steel)**			
	Air	Lime water	Air	Lime water Sphere 1	Lime water Sphere 2	Lime water Sphere 3
Spring constant (N/m)	0.61	0.61	1.78	1.38	1.52	1.60
Diameter (μm)	-	-	12.02	10.31	9.52	11.60

6.1.2 SFM force curves

Adhesive forces are measured from force curves that record the microsphere-substrate interactions. A representative force curve is shown in Fig. 39. In the approaching period, the signal is initially flat because the steel sphere does not contact the substrate surface. After the steel microsphere contacts the cement substrate, the cantilever is continuously driven downward so that the deflection signal increases linearly. In the retracting stage, the cantilever bends reversely as the as driven upward, thus decreasing the deflection signal with the same slope. The steel microsphere stays in contact with the cement substrate until the restoring force of the cantilever exceeds the adhesive forces between the microsphere and the substrate. After that, the deflection signal becomes flat again since the microsphere disengages from the substrate surface.

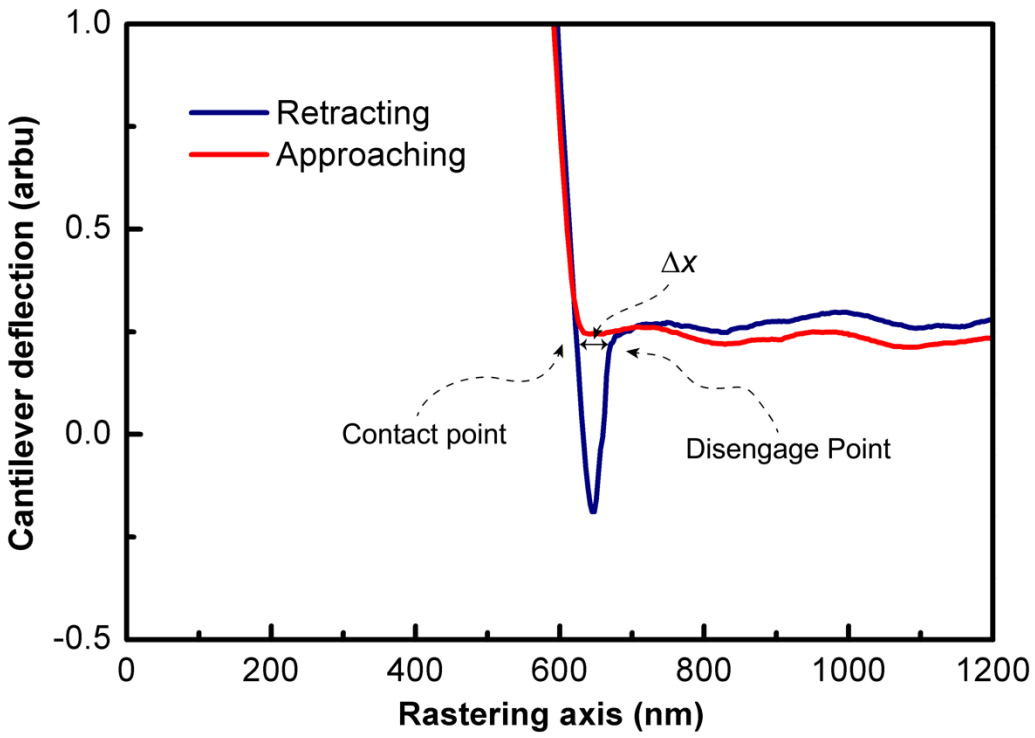

Figure 39: A representative force curve between a steel microspherical probe and an old hydrated cement substrate in saturated lime water.

6.1.3 Adhesion measurements between steel and different cement substrates

Adhesion measurements between steel and old cement in air and in saturated limewater are summarized in Fig. 40. For each 10×10 matrix, the adhesive forces are summarized in a boxplot, and the whisker length is 1.5 times of the box length. One box was for adhesion measurements between the bare probe and cement substrates in air and in saturated lime water, respectively. One box was for adhesion measurements between the steel microsphere and cement substrates in air. Three boxes were collected for adhesion measurements between the steel microsphere and cement substrates in saturated lime water. Similar plots created for adhesives between steel and new cement are not shown here.

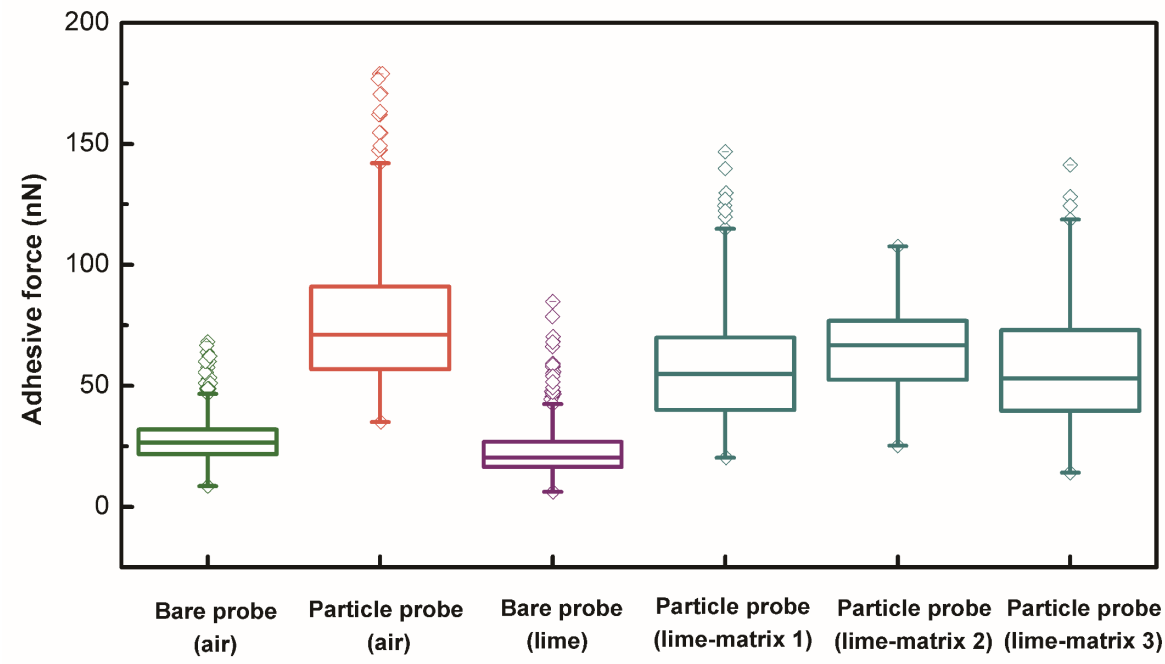

Figure 40: Boxplots of adhesive forces between old cement substrates and the steel microspheres and conventional probes. Measurements in air and in saturated lime water are both included.

To get an overview of adhesion measurements, we summarized average adhesive forces by probe types and measuring conditions in Fig. 41. The mean values and standard deviations are calculated from the 500 data for three groups, i.e., the bare probe in air, the bare probe in saturated lime water, and the microspherical steel probes in air. However, the mean values and standard deviations are calculated from the 1500 data for the group of steel microspheres in saturated lime water. It is shown that average adhesive forces between steel microspheres and cement substrates are larger than those between bare probes and cement substrates. Because the radius of the microsphere (~5μm) is much larger than that of the conventional bare probe (on the order of nm), a larger contact area exists between the particle probe and the cement substrate, and results in larger greater adhesive forces between them. For the same type of probes, larger adhesive forces are measured

between the probe and cement substrates in air than those in saturate lime water. This is because the meniscus [205, 206] formed between the probe and substrates in air provides extra capillary force to increase the adhesion. In addition, the adhesive forces measured using the new cement are generally smaller than those measured using the old cement in the same condition. For example, for measurements using the particle probe in saturated lime water, adhesive forces using the old cement specimens are larger than those measured using new cement specimens. Although the average adhesive forces do not elucidate all the details of adhesion in different hydrated phases, we can still obtain some information by comparing the results with prior findings. For example, it was found that the pullout strength between concrete and steel rods increases with age at least up to six months [124]. If the mechanical contribution of the bond strength maintains almost at the same level, these findings suggest that an increase in adhesion between steel and cement, which agrees with the trend disclosed in Fig. 40 using particle probe scanning force microscopy.

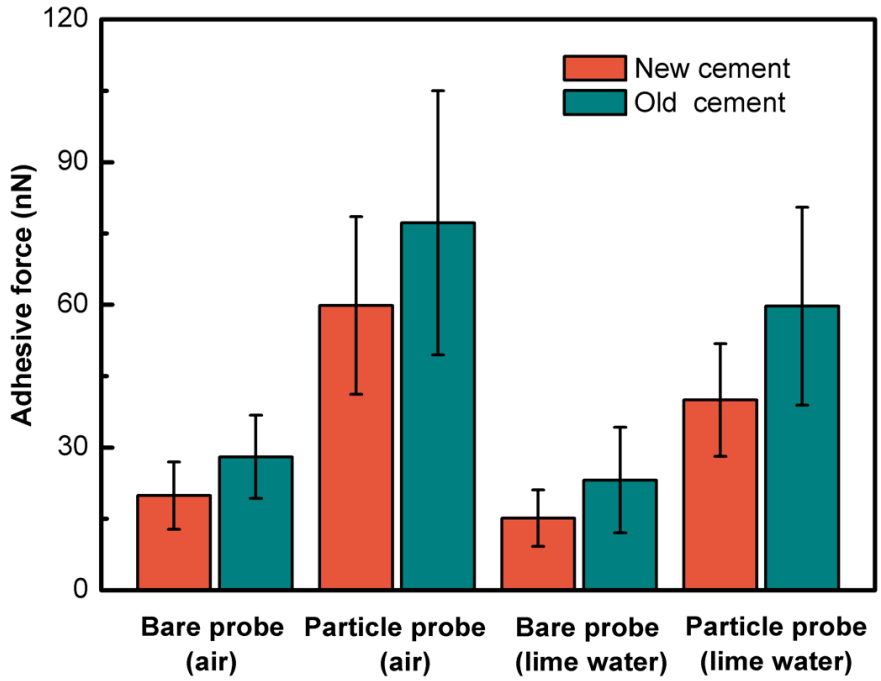

Figure 41: Average adhesive forces with standard deviations between steel and cement substrates measured in air and in saturated lime water.

6.1.4 Adhesion contours between aged hydrated cement substrate and probes

Contour plots of adhesive forces are shown to illustrate force distributions over the measurement matrices. In Fig. 42a to 42c, adhesive force contours between steel microspheres and old cement substrates in saturated lime water are shown because these measurements are collected in the simulated working condition [66-69]. The particle probe is able to characterize the adhesion differences between different hydrated products. For all plots, adhesive force varies between 30 and 110 nN over the matrices. It can be seen that adhesion contours vary from Fig. 42a to Fig. 42c because these measurements were collected at different regions of the cement substrate. For example, green areas (60-70 nN) distribute widely in the measurement matrix in Fig. 42b, whereas blue areas (40-50 nN)

cover the middle of matrix in Fig. 42c. For areas with larger adhesive forces (>100 nN), isolated red areas are found in all three matrices.

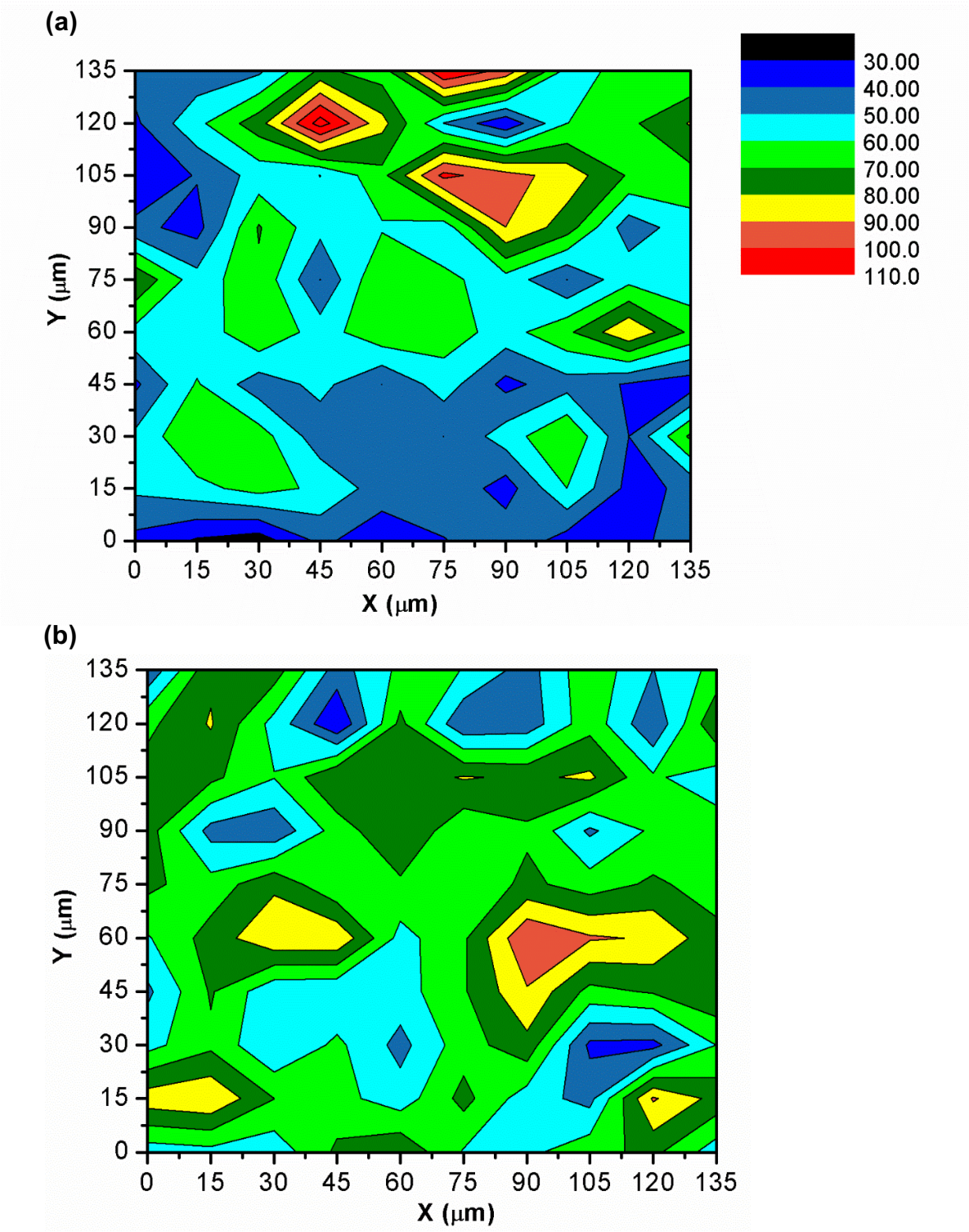

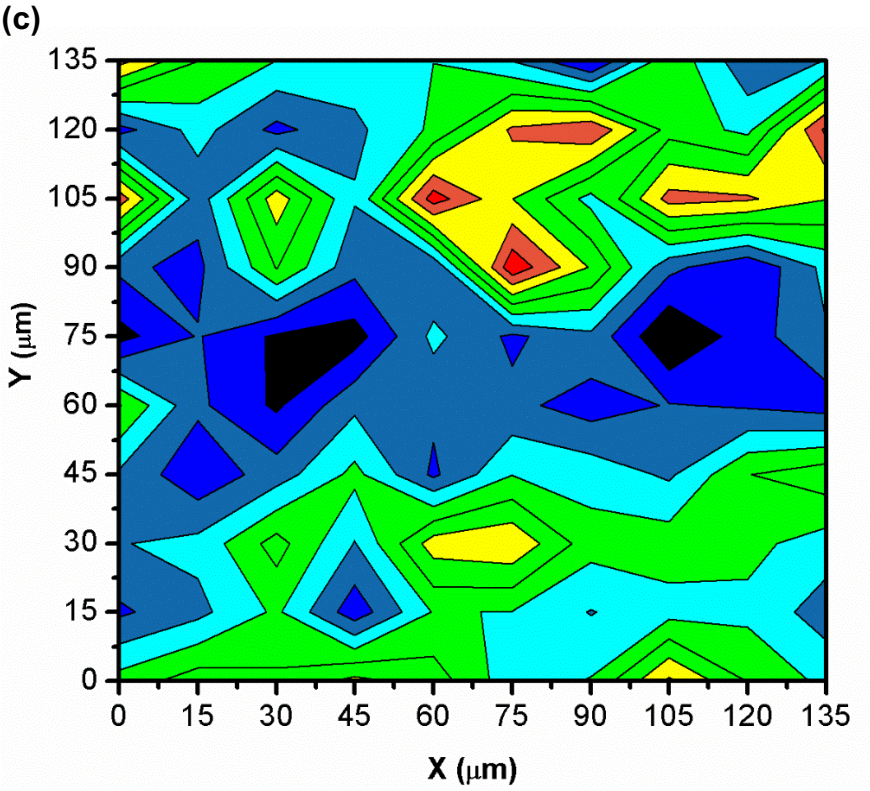

Figure 42: Contour plots of adhesive forces between steel microspheres and cement substrates measured in saturated lime water for (a) Matrix 1. (b) Matrix 2. (c) Matrix 3.

6.1.5 Decoupled distributions of adhesive forces using the mixed Gaussian model

Mixed Gaussian models were used to decouple the distributions of adhesive forces between steel and different hydrated products of old cement in saturated lime water. The frequency densities obtained from three measurement matrices were plot against the magnitudes of adhesive forces using the bin size of 23. An independent one-dimensional normal distribution is assumed for each phase, i.e., LD C-S-H, HD C-S-H, other hydrated products, CH, and unreacted components. The five distributions were created by minimizing the error between the experimental data and model predictions.

In Figs. 43a-43c, the decoupled force distributions were obtained from data in matrix 1 to 3, respectively. Fig. 43 d shows the decoupled force distributions based on the

combined data from the three matrices, i.e., 1500 measurements in total. The adhesive forces between steel and different hydrated products of old cement using the decoupled mixed Gaussian model are summarized in Table 17. It can be seen that the mean values, standard deviations and area fractions vary from matrix to matrix depending on the matrix locations. For example, the standard deviations of the unreacted components vary significantly between matrix 1 and 2. In addition, the area fractions of CH vary significantly between matrix 1 and 3. Similar trends exist in adhesive forces between steel and new cement, which are shown in chapter 5.

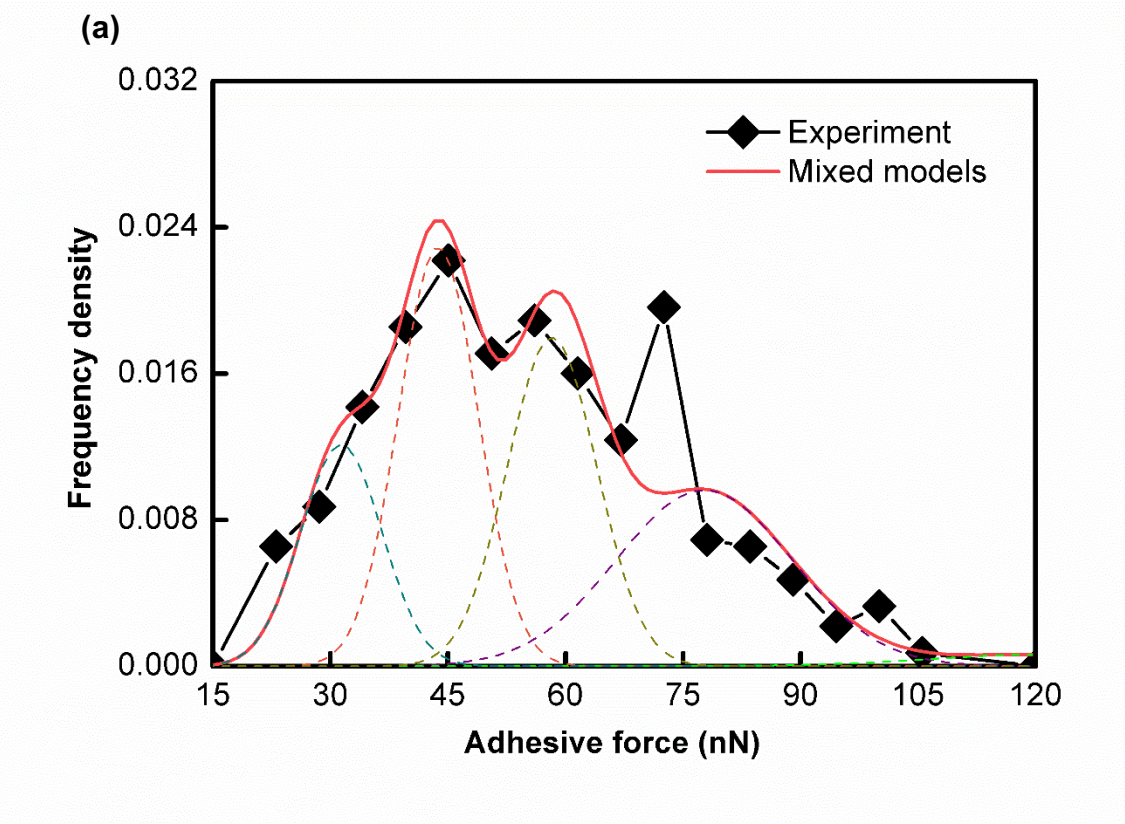

(b)

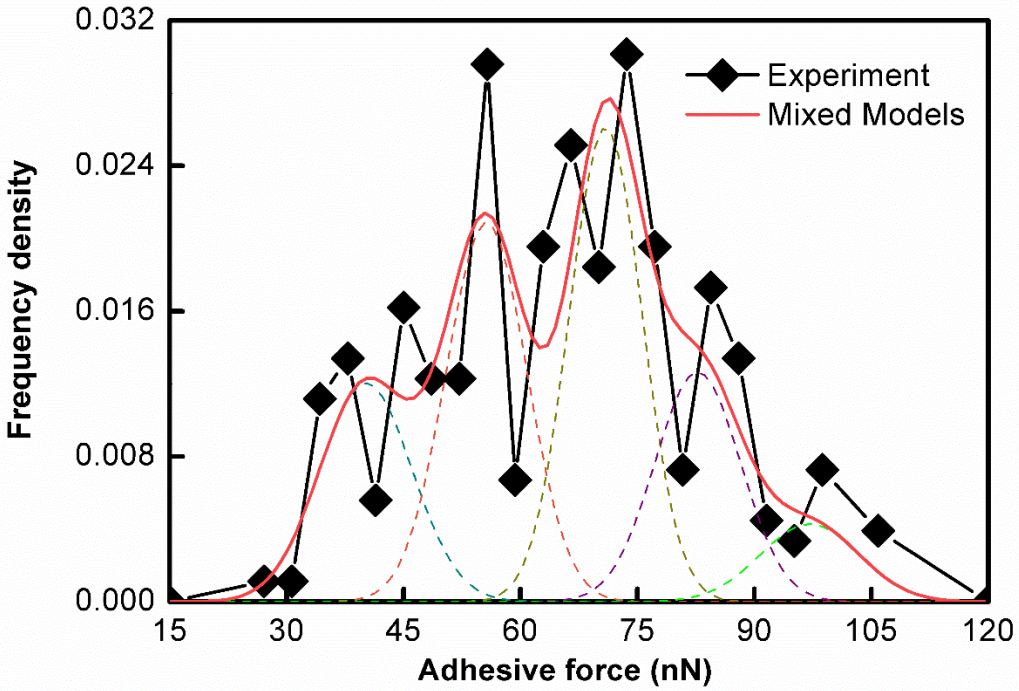
0.032
0.024
0.016
0.008
0.000
Frequency density
15
30
45
60
75
90
105
120
Adhesive force (nN)
Experiment
Mixed Models

(c)

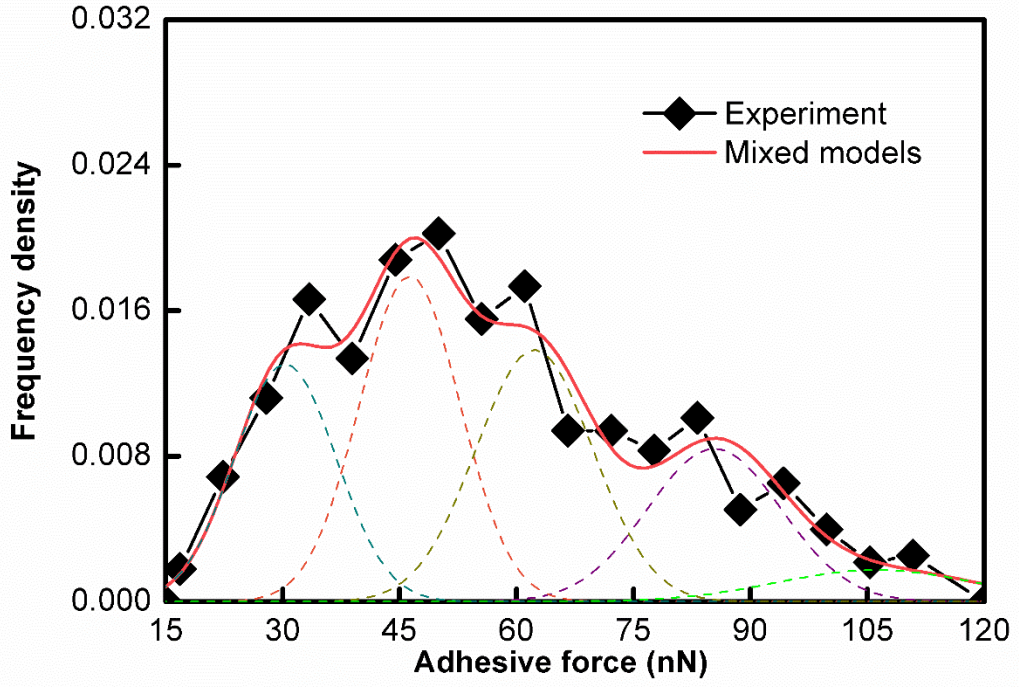
0.032
0.024
0.016
0.008
0.000
Frequency density
15
30
45
60
75
90
105
120
Adhesive force (nN)
Experiment
Mixed models

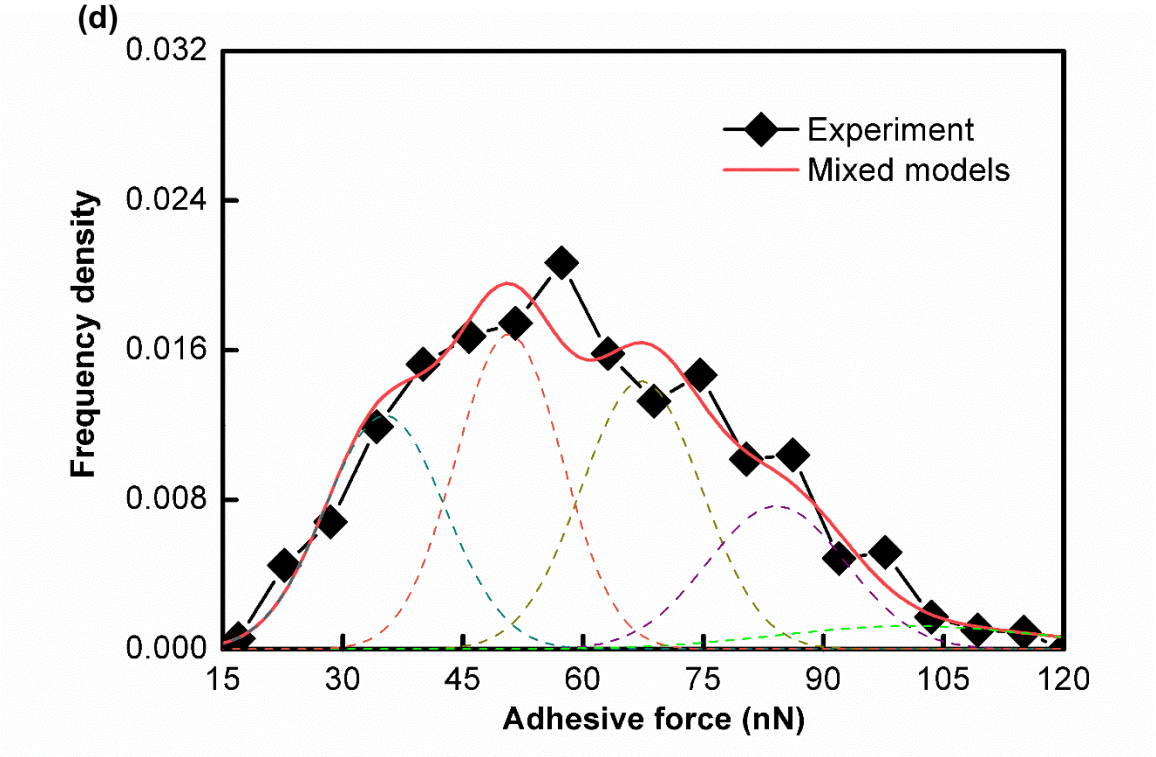

Figure 43: Frequency densities of adhesive forces between steel and old cement in (a) Matrix 1. (b) Matrix 2. (c) Matrix 3. (d) Three matrices combined.

Table 17: Summary of adhesive forces between steel and old cement decoupled using the mixed Gaussian models.

Matrix	*Phase R*	*Others*	*LD C-S-H*	*HD C-S-H*	*CH*	*Unreacted*
Matrix 1	μ_i (nN)	31.4	43.8	58.3	77.7	120.8
	σ_i (nN)	5.2	5.1	5.7	11.2	14.5
	f_i (%)	15.8	29.1	25.8	27.0	2.3
Matrix 2	μ_i (nN)	40.2	55.6	70.9	82.7	97.1
	σ_i (nN)	5.9	5.2	4.7	5.5	6.3
	f_i (%)	17.9	27.3	30.6	17.4	6.8
Matrix 3	μ_i (nN)	30.3	46.3	62.3	85.4	106.2
	σ_i (nN)	6.5	6.5	7.5	8.6	12.8
	f_i (%)	21.4	29.0	26.0	18.0	5.6
All	μ_i (nN)	35.3	50.7	67.3	84.2	101.0
	σ_i (nN)	7.5	6.6	7.4	8.6	16.5
	f_i (%)	23.4	28.0	26.8	16.6	5.2

6.1.6 XRD results

The diffraction patterns for the three samples are shown in Fig. 44. Peaks are labeled by their phases, i.e., Calcite ($CaCO_3$), C-S-H, Portlandite (CH), Ettringite (AFt), Alite (C_3S), Belite (C_2S) and Brownmillerite (C_4AF). For example, the peak at ~38° of the old cement shows less reactants (C_3S and C_2S) than those of the new cement, probably due to the continuous hydration during the six months. Conversely, the peak at ~18° of the old cement illustrates that the increase of the hydrated products, such as Aft and C-S-H, generate higher peaks than those of the new cement specimens. Calcium carbonate is found in new and old cement because of the carbonation between CH or C-S-H and the atmospheric carbon dioxide [210-213]. It can be seen that there are hump regions (pointed by arrows) in the curves for both new and old cement. This denotes that amorphous materials exist in these specimens.

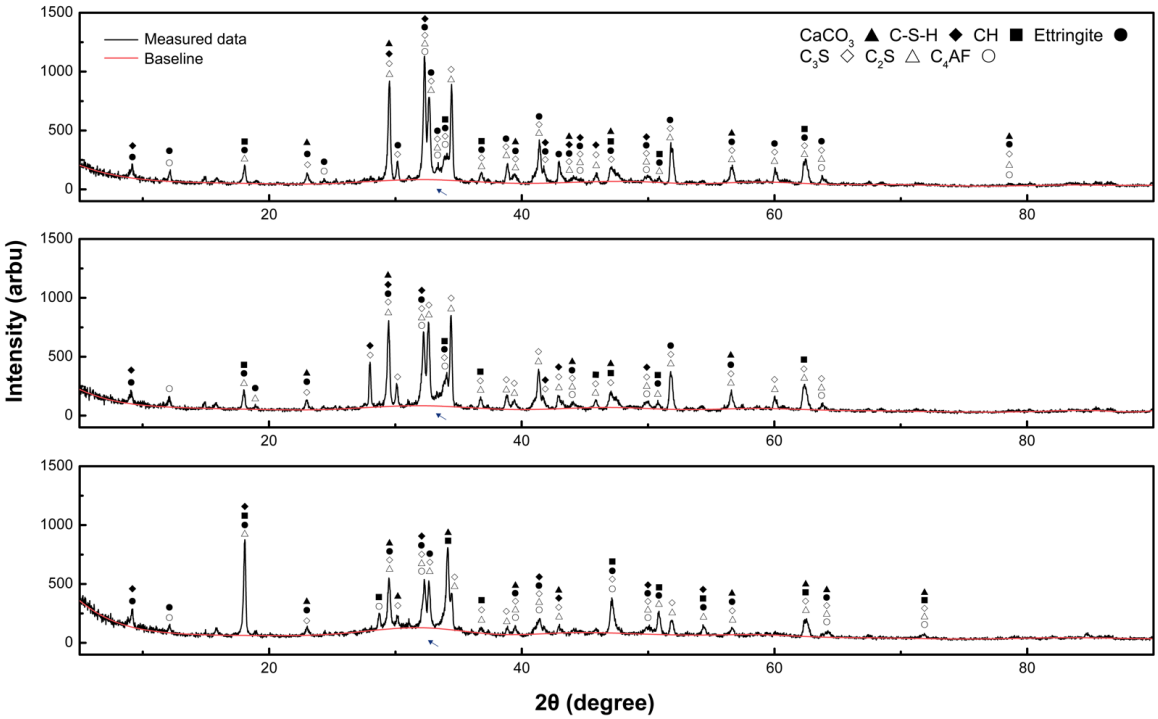

Figure 44: XRD results of (a) new cement. (b) new cement using the isopropanol exchange method. (c) old cement.

6.1.7 Electron probe microanalysis

The elemental mapping of calcium, silicon, aluminum and iron in the early hydrated and old cement specimens was shown in Fig. 45. These distributions are consistent with the primary elements in the hydrated cement. The elemental mapping of sodium, sulfur, potassium and magnesium were not included.

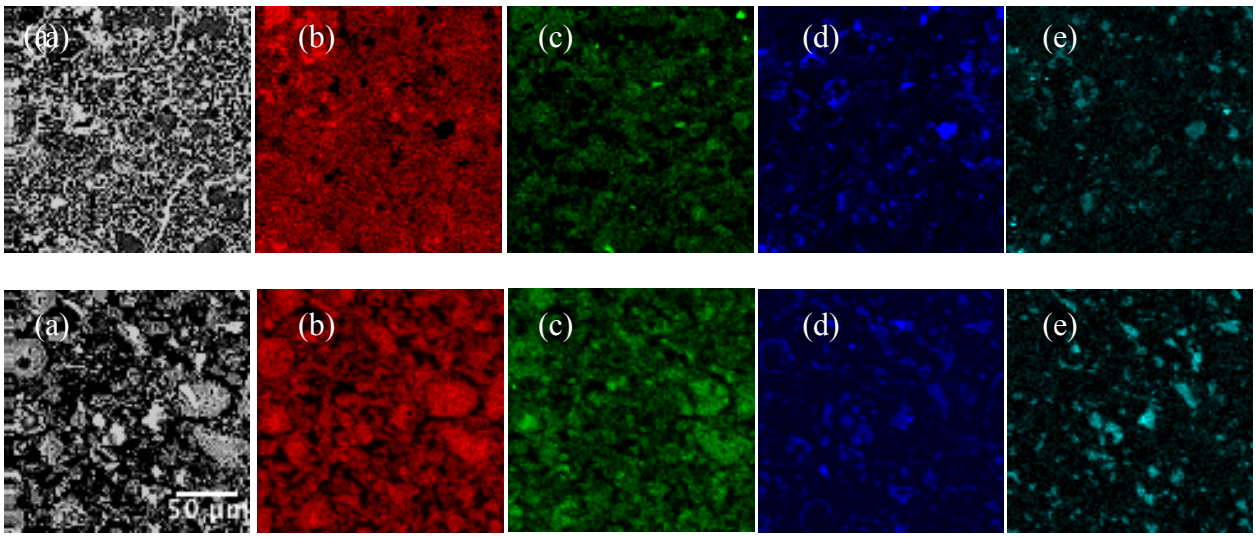

Figure 45: EPMA results of early-hydrated cement (up) and old cement (down): (a) A Back-scattered electron (BSE) image of the old cement used in the EPMA analysis. Elemental mappings of (b) Calcium (Ca). (c) Silicon (Si). (d) Aluminum (Al). (e) Iron (Fe).

6.2 Discussion

6.2.1 Adhesive forces between steel and control materials

Adhesive forces measured between steel and Iceland spar were compared with those measured between steel and different hydrated products (Fig. 46a). The adhesive forces between steel microspheres and Iceland spar substrates were 77.2 ± 16.3 nN, which was close to the adhesive forces (84.2 ± 8.6 nN) between steel and the decoupled "CH" phases of the old cement substrates. Because the old cement substrates were exposed in air for several months before measurements, the calcium hydroxide and C-S-H reacted with carbon dioxide in air to form calcium carbonate in corresponding locations.

In addition, adhesive forces between steel and synthetic C-S-H were compared with those measured between steel and the decoupled LD C-S-H and HD C-S-H (Fig. 40b). The adhesive forces between steel and the synthetic C-S-H gel (Ca/Si = 0.8) were 43.8 ± 18.9

nN, whereas the adhesive forces between steel and the other C-S-H gel (Ca/Si = 1.4) were 39.8 ± 17.1 nN. The mean values of adhesive forces between steel and the synthetic C-S-H gels were similar to those between steel and the decoupled LD C-S-H (31.2 ± 4.2 nN), and those between steel and the decoupled HD C-S-H (42.0 ± 4.0 nN). The larger standard deviations of adhesive forces may be related to the heterogeneous microstructures of the synthetic materials.

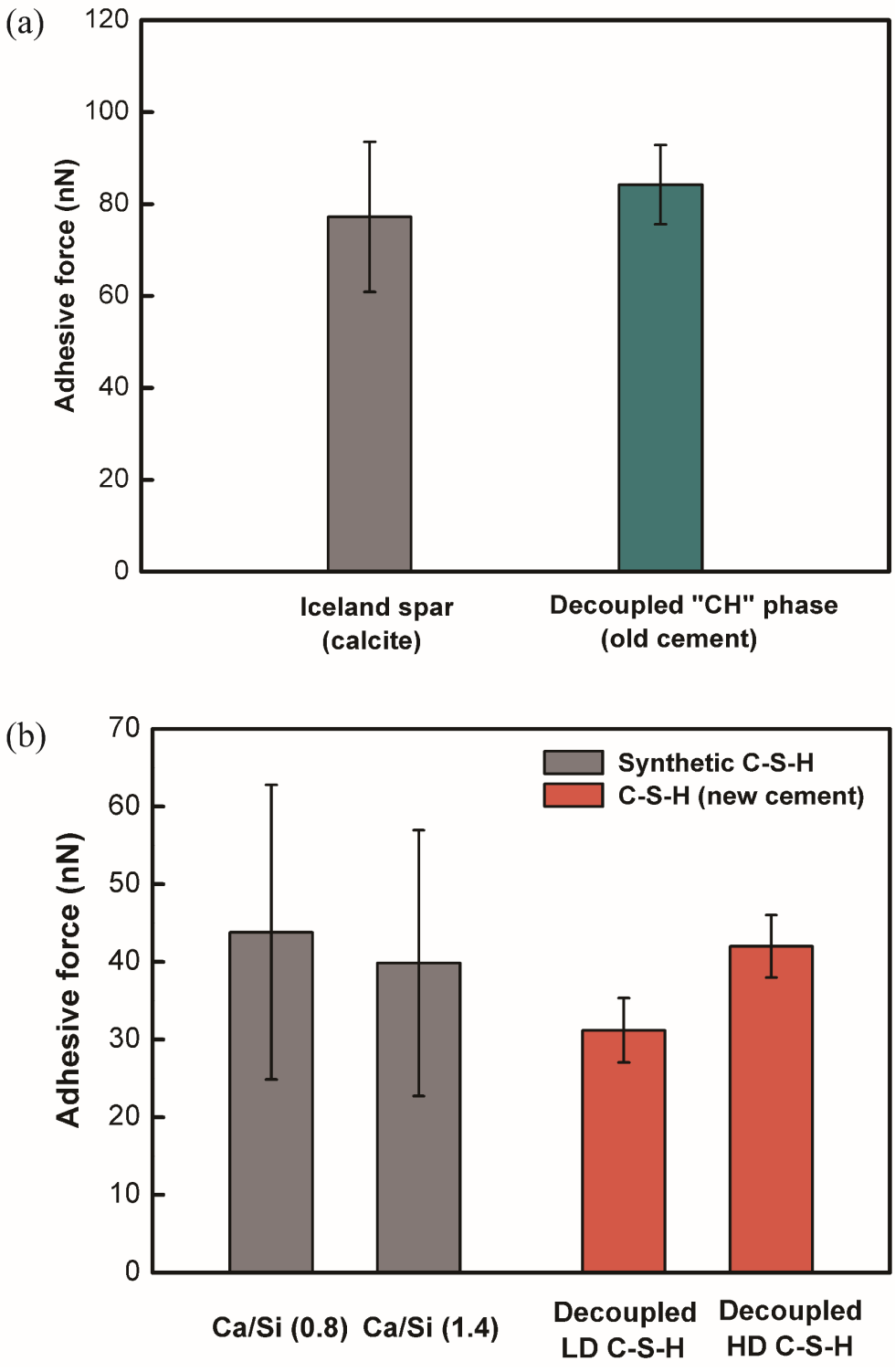

Figure 46: (a) Adhesive forces between steel and Iceland spar, between steel and the decoupled "CH" in the old cement; part of CH and C-S-H turned into calcium carbonate in the old cement. (b) Adhesive forces between steel and synthetic C-S-H gels, between steel and the decoupled LD C-S-H and HD C-S-H in the new cement.

6.2.2 Area fractions from adhesion experiments and the hydration models.

In this study, area fractions of the hydrated products are estimated using the hydration model at hydration degrees varying from 0.70 to 0.95. In Fig. 47, the connected triangles denote the estimated area fractions at 95% hydration, whereas the connected diamonds denote the estimated area fractions at 70% hydration. It is shown that area fractions of the unreacted components decoupled from the Gaussian models are the smallest among the five groups. The corresponding estimations of these fractions decrease substantially as the hydration degree increases from 0.70 to 0.95.

The area fractions of CH are the second lowest among the five groups. A good agreement of is achieved between estimations from the hydration model and the decoupled data for the new cement. As shown in Fig. 47, adhesive forces between steel and "CH" of the old cement are very similar to those measured between steel and calcium carbonate, indicating that a large portion of CH on the substrate surface turns into calcium carbonate during the carbonation. Since C-S-H also reacts with carbon dioxide in the air, the total area fractions of calcium carbonate in the old cement exceed those of CH in the new cement.

Even though the area fractions of LD C-S-H and HD C-S-H vary with their mass ratio (M_r), the decoupled area fractions generally agree with the estimations from the hydration model. It can be seen that the area fractions of LD C-S-H in the new cement are larger than those in the old cement, and similar results were observed for HD C-S-H. The reduction of C-S-H in the old cement maybe because part of C-S-H was transformed to calcium carbonate due to carbonation.

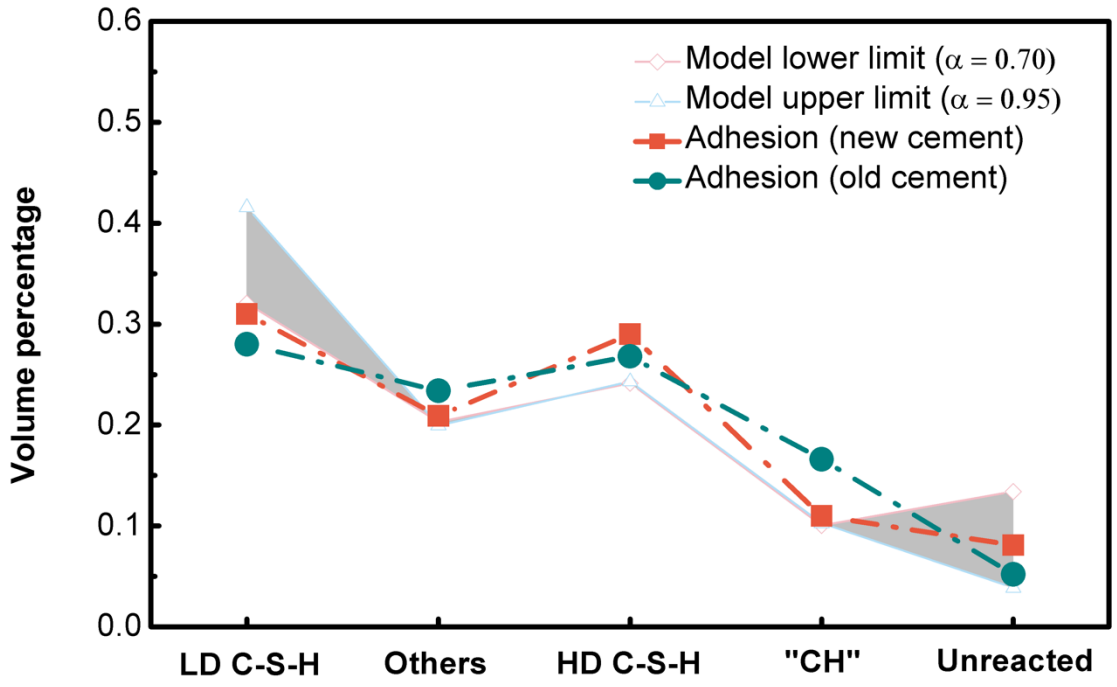

Figure 47: Comparison of area fractions between decoupled data and model estimations for the hydration degree ranging from 0.70 to 0.95. Part of CH and C-S-H turn into calcium carbonate in the old cement.

6.2.3 Area fractions from adhesion experiments and EPMA data analysis.

In this study, area fractions of different hydrated products were estimated from both the adhesion measurements and the EPMA analysis. The estimated fractions from adhesion measurements were based on the mixed Gaussian models, in which the fractions were listed in Table 17. In the microscopic analysis, we found that sub-micron phases existed in the hydrated cement samples. Because the minimum resolution of the EPMA analyzer used in this study was 1μm, it was extremely difficult to isolate the sub-micron phases. On the other hand, we used the beam with the diameter of 5μm to analyze the weight percentages

of different oxides at microscale. It was assumed that the phase groups, i.e., LD C-S-H, HD C-S-H, CH, other hydrated products and unreacted components, contributed collectively to these oxides. For each point analyzed, the weight percentages of the primary oxides, i.e., calcium oxide, silicon oxide and aluminum oxide, were best fit by combining the phase groups at various ratios. Two possible combinations were collected, from which the area fractions were calculated from the average of these two combinations. The ratios between LD C-S-H and HD C-S-H were estimated based on equation 14 in chapter 5. The area fractions of different hydrated products estimated from the EPMA analysis were plot in Fig. 48. Large, overlapped error bars of areas fractions occurred in EPMA estimations indicating the variability of the combined phases. However, a general trend of area fractions estimated from EPMA analysis appeared across different hydrated products.

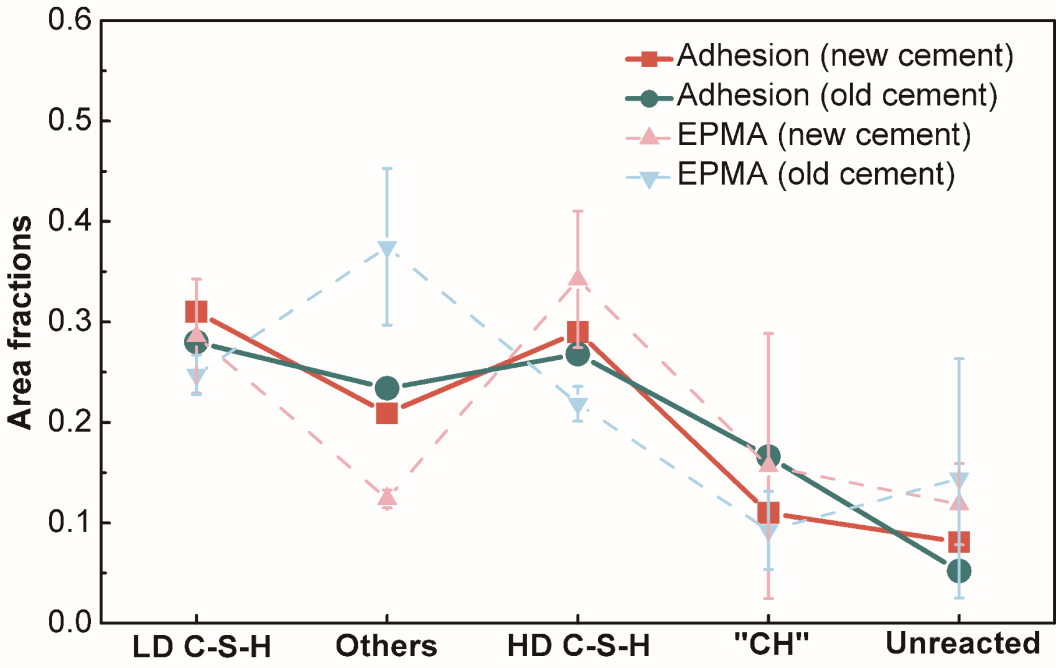

Figure 48: Comparison of area fractions between decoupled Gaussian distributions and EPMA analysis. Part of CH and C-S-H turned into calcium carbonate in the old cement.

As shown in Fig. 48, area fractions of the unreacted components were the smallest among the five groups. The area fractions of CH were the second lowest among the five groups. As shown in Fig. 46a, adhesive forces between steel and "CH" of the old cement were similar to those measured between steel and calcium carbonate, indicating that a large portion of CH on the substrate surface turned into calcium carbonate during the carbonation. Since C-S-H also reacted with carbon dioxide in air, the total area fractions of calcium carbonate in the old cement exceeded those of CH in the new cement, which was consistent with results from the adhesion measurements.

It is shown that the area fractions of LD C-S-H in the new cement were larger than those in the old cement, and similar results were observed for HD C-S-H. The reduction of C-S-H in the old cement maybe because part of C-S-H was transformed to calcium carbonate during carbonation. In adhesion measurements, similar area fractions of the other hydrated products were obtained between new and old cement. However, due to the complicated components inside the group, area fractions estimated for the other hydrated products varied substantially in the EPMA analysis.

6.2.4 Adhesive forces of different hydrated products

Based on the decoupled data, the adhesive forces of different hydrated products are listed in Fig. 49. For the new cement, the adhesive forces of LD C-S-H, Other products and HD C-S-H were intermediate, i.e., 30 to 50 nN (mean values). Lower adhesive forces in LD C-S-H was probably because the low packing density makes the microstructure of LD C-S-H more porous [204, 214], resulting in less effective contact to steel microspheres than

those of HD C-S-H. For the old cement, carbonation was essential to the adhesive properties of different hydrate products. Carbonation led to a reduction of porosity in general [215]. The original C-S-H, i.e., LD and HD C-S-H, were converted to a calcium-modified silica gel and calcium carbonate [211]. Once the calcium carbonate crystals nucleated on the HD C-S-H gel fibrils, they grew by attracting calcium from the nearby LD C-S-H [211]. Thus, the microstructure of LD C-S-H became relatively more porous than those of HD C-S-H due to the removal of calcium ions. The hybrid C-S-H and calcium carbonate led to an increase in the adhesive forces in corresponding locations. However, the adhesive forces of LD C-S-H were still lower than those of HD C-S-H in the old cement.

For the new cement, the adhesive forces between steel and CH were the smallest among the five groups. It is known that CH microstructures contain various sheets oriented randomly, which on average do not favor contact to steel microspheres. For the old cement, CH were transferred to calcium carbonate so that larger adhesive forces were obtained in corresponding locations. The summed areas of LD C-S-H, HD C-S-H and others occupy substantial portions of the matrices, which were consistent with the contour plots in Figs. 42a-42c.

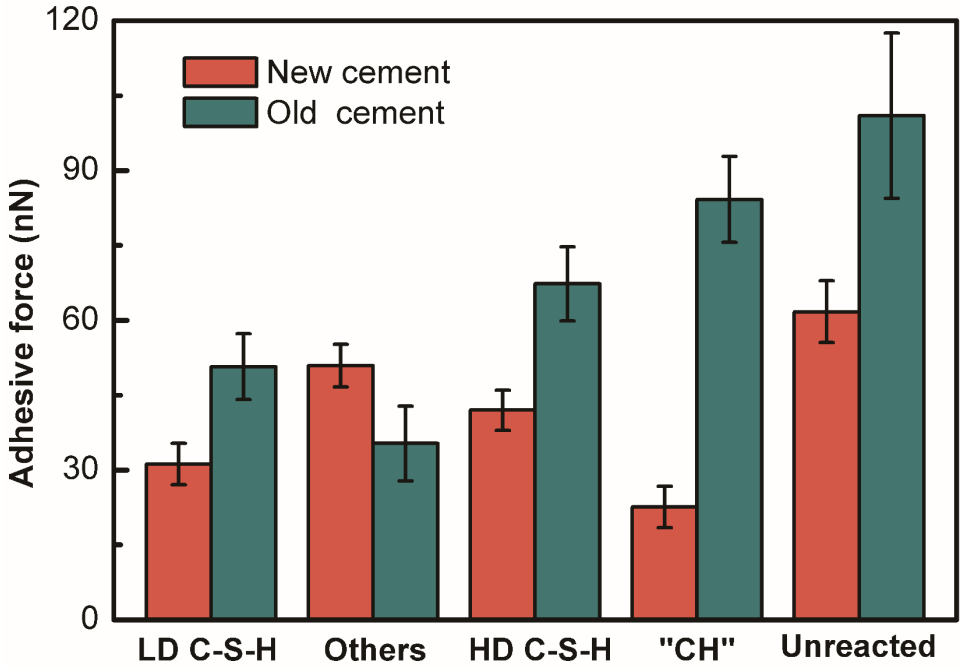

Figure 49: Adhesive forces of different hydrated phases in new and old cement specimens. Part of CH and C-S-H turned into calcium carbonate in the old cement.

The unreacted components covered the least area fractions (<10%) for both the new and old cement. However, the adhesive forces between steel and unreacted components were the largest among the five groups. This may be related to the liquid phase in the clinkering process. When the kiln temperature reaches 1400 to 1500˚C, 20-30 vol.% materials are transformed into liquid. The high surface tension of the liquid phase helps mix agglomerates into larger nodules, which is essential to the clinker quality [209]. The clinkering process is deemed complete when the amount of C_3S, C_2S and free lime is reduced to a certain level, whereas the solidified liquid phases may still maintain unreacted components with high surface tension. This could be linked to the amorphous materials in the XRD curves, on which future research is needed.

The adhesive forces between steel and the group of others were relatively complicated since different hydrated products were involved. Future effort is also needed to study the adhesive forces for these hydrated products. In addition, accurate correlations between adhesive forces and different hydrated phases may be obtained through the high resolution imaging techniques [216].

6.3 Conclusions

In this chapter, we presented a study on adhesion between steel and different hydrated cement phases at microscale using particle probe scanning force microscopy. First, we created particle probes by attaching individual steel microspheres to the free ends of microcantilevers. Then, adhesive forces were collected between steel and new or old cement in air and in saturated lime water, respectively. As a comparison, adhesive forces were measured between conventional scanning force microscope probes and the new or old cement accordingly. The results showed that the adhesive forces measured using steel microspheres were greater than those measured using conventional SFM probes. This is because larger contact areas existed between steel microspheres (~5μm in radius) and cement substrates than those between conventional SFM probes (nanoscale radius) and cement substrates. Meanwhile, larger adhesive forces were measured between probes and cement substrates in air than those measured in saturated lime water. The reason was that the water meniscus formed by capillary forces between the probes and substrates provided the extra adhesive forces. The average adhesive forces between steel and old cement were greater than those between steel and new cement.

The use of mixed Gaussian models has allowed us to decouple adhesive forces between steel and five different hydrated groups in saturated limewater, i.e., LD C-S-H, others, HD C-S-H, CH and unreacted components. Weight percentages of oxides obtained from EPMA analysis were also used to estimate the area fractions of different hydrated phases. In this study, an average function was used to predict the mass ratio between LD C-S-H and HD C-S-H. The capillary pores were assumed evenly distributed proportional to the area fractions of different hydrated phases. Consistent correlations were obtained between the decoupled data and estimations from the hydration model, and between the decoupled Gaussian model and the EPMA analysis.

Based on the decoupled results, adhesive forces of different phases were designated for both the new and old cements. For the new cement, the results showed that LD C-S-H, others and HD C-S-H exhibited intermediate adhesive forces to steel. The adhesive forces between LD C-S-H and steel were smaller than those between HD C-S-H and steel probably because the more porous microstructure of LD C-S-H did not favor effective contact to the steel microspheres. For the old cement, carbonation led to a reduction in porosity. Calcium carbonate crystals nucleated on HD C-S-H fibrils and grew by attracting calcium from the nearby LD C-S-H, making LD C-S-H relatively more porous in microstructure. The hybrid C-S-H and calcium carbonate led to an increase in adhesive forces, but LD C-S-H still exhibited lower adhesive forces than HD C-S-H in the old cement. CH also turned into calcium carbonate by reacting with carbon dioxide in air. An increase in adhesive forces was found between steel and calcium carbonate in the old cement than those between steel and CH in the new cement. The unreacted components exhibited the largest adhesive forces among all groups in new and old cements. This may

be related to the liquid phase in the clinkering process, which maintained some phases exhibiting high surface after solidification.

CHAPTER 7: CONCLUSION AND FUTURE WORK

7.1 Conclusions

The test successfully detected the differences of adhesion in bituminous and cementitious materials at the microscopic scale using the particle-modified probes.

For asphalt binders, the results showed that these modified SFM probes could effectively measure the adhesion between binders and aggregate minerals. Three types of particle probes were created using microspheres representing the primary chemical constituents of aggregates, i.e., silica, calcium carbonate and alumina. Consistent adhesion measurements were obtained between different asphalt binders and aggregate mineral particles. For plain binders, alumina-binder pairs exhibited the largest adhesion, while silica-binder and calcium carbonate-binder pairs exhibited relatively smaller adhesion. The alumina-binder adhesion decreased as the value of the maximum pavement design temperature increased while increased as the value of the minimum pavement design temperature decreased. The silica-binder and calcium carbonate-binder adhesion did not exhibit any monotonic trend.

For modified binders, alumina-binder pairs exhibit highest adhesion compared to silica- or calcium carbonate-binder pairs. Higher alumina-binder adhesion occurs as weight percentages of modifiers (PPA, SBS and SBR) used in this study increase. Based on the SARA fraction of binders, the major part is resin, i.e., polar aromatics. Due to the stronger polarity of alumina particles, stronger interactions occur within alumina-binder pairs. Meanwhile, morphologies of different modified binders clearly demonstrated microstructural variations in these binders. As weight percentages of modifiers increased, more organized flocculent wings occurred around bee structures in PPA modified binders.

In SBS and SBR modified binders, larger bee structures occurred with more sparse distributions. These studies showed the correlation between the binder-aggregate adhesion and binder microstructures.

For cementitious materials, particle probe scanning force microscopy was used to measure the adhesion between steel microspheres and the early-hydrated cement. First, steel particle probes were fabricated by attaching steel microspheres to the free ends of microcantilivers. The adhesive forces between steel microspheres and cement pastes were measured in air and in saturated lime water. As a comparison, conventional silicon SFM probes were used to measure the adhesive forces to cement paste in corresponding conditions.

For early hydrated cement, adhesive forces measured using the particle probes are larger than those measured using SFM probe. This is because larger contact areas between the steel microspheres and cement substrates lead to greater adhesive forces. Due to the capillary bridges, adhesive forces measured in air are greater than those measured in lime water for both particle and conventional probes. Consistent contours were obtained for all matrices between steel microspheres and cement substrates in saturated lime water. Adhesive forces mostly range from 30 to 60 nN. Some islands exhibit adhesive forces greater than 60 nN; while other areas exhibit adhesive forces less than 30 nN. The estimated volume fractions from the hydration model reasonably capture the data trends in the adhesion tests. Based on these results, several groups were deconvoluted, i.e., LD C-S-H, HD C-S-H, CH, other hydrated products and the unreacted components. Results showed that LD C-S-H, HD C-S-H and other hydrated products exhibit intermediate adhesive forces among all groups. LD C-S-H exhibits slightly smaller adhesion than HD C-S-H

possibly because its more porous microstructures do not enable contact to steel microspheres as effectively as that of HD C-S-H. CH exhibits the smallest adhesive forces showing that the irregular sheets in the microstructure did not promote their contact to steel microspheres. The unreacted components exhibit the largest adhesive forces. It is postulated that the isolated adhesive peaks are related to the solidified liquid clinker phases with high surface tension. More work is needed to elucidate the areas with large adhesive forces.

For six-month old cement, the results showed that the adhesive forces measured using steel microspheres were greater than those measured using conventional SFM probes. Meanwhile, larger adhesive forces were measured between probes and cement substrates in air than those measured in saturated lime water. The reason was that the water meniscus formed by capillary forces between the probes and substrates provided the extra adhesive forces. The average adhesive forces between steel and old cement were greater than those between steel and new cement. The use of mixed Gaussian models has allowed us to decouple adhesive forces between steel and five different hydrated groups in saturated limewater, i.e., LD C-S-H, others, HD C-S-H, CH and unreacted components. Weight percentages of oxides obtained from EPMA analysis were also used to estimate the area fractions of different hydrated phases. In this study, an average function was used to predict the mass ratio between LD C-S-H and HD C-S-H. The capillary pores were assumed evenly distributed proportional to the area fractions of different hydrated phases. Consistent correlations were obtained between the decoupled data and estimations from the hydration model, and between the decoupled Gaussian model and the EPMA analysis. Based on the decoupled results, adhesive forces of different phases were designated for both the new

and old cements. For the new cement, the results showed that LD C-S-H, others and HD C-S-H exhibited intermediate adhesive forces to steel. The adhesive forces between LD C-S-H and steel were smaller than those between HD C-S-H and steel probably because the more porous microstructure of LD C-S-H did not favor effective contact to the steel microspheres. For the old cement, carbonation led to a reduction in porosity. Calcium carbonate crystals nucleated on HD C-S-H fibrils and grew by attracting calcium from the nearby LD C-S-H, making LD C-S-H relatively more porous in microstructure. The hybrid C-S-H and calcium carbonate led to an increase in adhesive forces, but LD C-S-H still exhibited lower adhesive forces than HD C-S-H in the old cement. CH also turned into calcium carbonate by reacting with carbon dioxide in air. An increase in adhesive forces was found between steel and calcium carbonate in the old cement than those between steel and CH in the new cement. The unreacted components exhibited the largest adhesive forces among all groups in new and old cements. This may be related to the liquid phase in the clinkering process, which maintained some phases exhibiting high surface after solidification.

7.2 Future work

More work is needed in the future to elucidate the adhesive forces between asphalt binders and aggregates as well as between steel and hydrated cement.

For bituminous materials, this proposed methodology provides opportunities to evaluate the effects of different processing methods on the performance of asphalt binders, and to generate quantitative information for the development of multi-scale asphalt mixture cracking models. Also, this method also can be used to study the interface mechanism

between asphalt and aggregate under different temperatures or to investigate the effect of salt under low temperatures.

For cementitious materials, this work presents a method to study adhesion between steel and the cement paste at microscale. A number of potential studies on the cement-steel adhesion can be further developed, such as the evolution of cement-steel adhesion at different aging periods, and the degradation of cement-steel interfaces due to the chloride attack at microscale. Results of these studies and opened new avenues to study the interactions between steel and cement at microscale under a variety of environmental conditions and can be formulated as crack initiation and propagation criteria incorporated in multiscale models for reinforced concrete structures

References

[1] U.S. Department of Transportation. National transportation statistics. Research and innovative technology administration. http://www.rita.dot.gov/bts/sites/rita.dot.gov.bts/files/publications/national_transportation_statistics/html/table_01_01.html, (accessed 2014.07.20).

[2] American Association of State Highway and Transportation Officials (2009). Rough Roads Ahead: Fix Them now or Pay for it Later Publication RRA-1, AASHTO, U.S. Department of Transportation.

[3] Anderson, D., Youtcheff, J., Zupanick, M. (2000). Transportation Research Board, Asphalt Binders.

[4] National Asphalt Pavement Association, Asphalt pavement overview. Lanham, Maryland. http://www.asphaltpavement.org/index.php?option=com_tent&view=article&id=14&Itemid=34, (accessed 2014.07.20).

[5] Kelly, Willam M. (2011). "Mineral industry of the state of New York." http://www.nysm.nysed.gov/staffpubs/docs/20367.pdf, (accessed 2015.05.05).

[6] Read, J., Whiteoak, D. (2003). The Shell Bitumen Handbook, Thomas Telford.

[7] ASTM D4124 (2009). Standard test method for separation of asphalt into four fractions, in: Annual Book of ASTM, American Society for Testing and Materials.

[8] O'Donnell, G., Snider, L. T., & Rietz, E. G. (1951). Separating asphalt into its chemical constituents. *Analytical Chemistry*, 23(6), 894-898.

[9] Young, J.F., Bentur, A., Mindess, S. (1998). The Science and Technology of Civil Engineering Materials.

[10] Xu, G., & Wang, H. (2017). Molecular dynamics study of oxidative aging effect on asphalt binder properties. *Fuel*, 188, 1-10.

[11] Superpave Performance Grading, https://www.pavementinteractive.org/reference-desk/materials/asphalt/superpave-performance-grading/#refmark-1, (accessed 2017.07.20)

[12] Navarro, F. J., Martínez- Boza, F. J., Partal, P., et al. (2001). Effect of processing variables on the linear viscoelastic properties of SBS-oil blends. *Polymer Engineering & Science*, 41(12), 2216-2225.

[13] Zhang, H. L., Wang, H. C., & Yu, J. Y. (2011). Effect of aging on morphology of organo- montmorillonite modified bitumen by atomic force microscopy. *Journal of microscopy*, 242(1), 37-45.

[14] Roberts, F.L., Kandhal, P.S., Brown, E.R., Lee, D.Y. and Kennedy, T.W. (1996). Hot Mix Asphalt Materials, Mixture Design, and Construction. National Asphalt Pavement Association Education Foundation. Lanham, MD.

[15] What are the Types of Modifier in Bitumen? available at http://www.engineeringcivil.com/what-are-the-types-of-modifier-in-bitumen.html, (accessed 2015.03.05)

[16] Zhu, J., Birgisson, B., & Kringos, N. (2014). Polymer modification of bitumen: Advances and challenges. *European Polymer Journal*, 54, 18-38.

[17] Larsen, D. O., Alessandrini, J. L., Bosch, A., & Cortizo, M. S. (2009). Micro-structural and rheological characteristics of SBS-asphalt blends during their manufacturing. *Construction and Building Materials*, 23(8), 2769-2774.

[18] Rogue, R., Birgisson, B., Tia, M., Kim, B., & Cui, Z. (2004). Guidelines for use of modifiers in Superpave mixtures: evaluation of Ground-Tire-Rubber (GTR). Florida Department of Transportation, Gainesville, FL.

[19] Collins, J. H., Bouldin, M. G., Gelles, R., & Berker, A. (1991). Improved performance of paving asphalts by polymer modification (with discussion). *Journal of the Association of Asphalt Paving Technologists*, 60.

[20] Pradhan, M. M., & Armijo, J. D. (1993). Assessing effects of commercial modifiers on Montana asphalts by conventional testing methods. *Transportation research record*, (1417).

[21] Verhaeghe, B. M. J. A., F. C. Rust, R. M. Vos, and A. T. Viser. (1994). Properties of Polymer- and Fibre Modified Porous Asphalt Mixes. Proceedings for 6th Conference on Asphalt Pavements for Southern Africa, Vol. 1.

[22] The Use and Performance of Asphalt Binder Modified with Polyphosphoric Acid (PPA). https://www.fhwa.dot.gov/pavement/asphalt/pubs/hif12030.pdf, (accessed 2016.08.24)

[23] Chapter 2 Asphalt and Asphalt Paving Materials. http://www.apai.net/Files/content/DesignGuide/Chapter_2B.pdf, (accessed 2015.03.14)

[24] Blatt, H., Tracy, R.J., Owens, B. (2006). Petrology: Igneous, Sedimentary, and Metamorphic, Macmillan.

[25] Market Research Report - Global concrete and cement market analysis. http://www.marketwired.com/press-release/market-research-report-global-concrete-and-cement-market-analysis-1744222.htm, 2013(accessed 2017.06.08)

[26] Global concrete and cement report market 2016-2020. https://www.technavio.com/report/global-construction-concrete-and-cement-market, 2016(accessed 2017.06.08).

[27] Portland cement. http://www.edubilla.com/invention/portland-cement/ (accessed 2016.04.23).

[28] Ricketts, J. T., Loftin, M. K., & Merritt, F. S. (2003). Standard Handbook for Civil Engineers (Handbook). McGraw-Hill Professional.

[29] Brown, C. B. (1966). Bond failure between steel and concrete. *Journal of the Franklin Institute*, 282(5), 271-290.

[30] Almusallam, A. A. (2001). Effect of degree of corrosion on the properties of reinforcing steel bars. *Construction and Building Materials*, 15(8), 361-368.

[31] Fu, X. D. D. L., & Chung, D. D. L. (1997). Effect of corrosion on the bond between concrete and steel rebar. *Cement and Concrete Research*, 27(12), 1811-1815.

[32] Haddad, R. H., Al-Saleh, R. J., & Al-Akhras, N. M. (2008). Effect of elevated temperature on bond between steel reinforcement and fiber reinforced concrete. *Fire Safety Journal*, 43(5), 334-343.

[33] Abrams, D.A. (1913). Tests of bond between concrete and steel. University of Illinois at Urbana Champaign, College of Engineering. Engineering Experiment Station.

[34] R.M. Mains. (1951). Measurement of the distribution of tensile and bond stresses along reinforcing bars, *Journal Proceeding*, 48(11), 225–252.

[35] Tepfers, R. (1979). Cracking of concrete cover along anchored deformed reinforcing bars. *Magazine of concrete research*, 31(106), 3-12.

[36] Eligehausen, R., Popov, E.P., Bertero, V. V. (1982). Local bond stress-slip relationships of deformed bars under generalized excitations.

[37] D.Z. Yankelevsky. (1985). Bond action between concrete and a deformed bar-a new model, *Journal Proceeding*, 82 (2), 154–161.

[38] Panda, A. K., Spencer, R. A., & Mindess, S. (1986). Bond of deformed bars in steel fibre reinforced concrete under cyclic loading. *International Journal of Cement Composites and Lightweight Concrete*, 8(4), 239-249.

[39] ASTM-C900 (1987). Test method for pullout strength of hardened concrete, American of Society of Testing Materials.

[40] Meguro, K., & Hakuno, M. (1989). Fracture analyses of concrete structures by the modified distinct element method. *Doboku Gakkai Ronbunshu*, (410), 113-124.

[41] Malvar, L. J. (1992). Bond of reinforcement under controlled confinement. *Materials Journal*, 89(6), 593-601.

[42] Cox, J.V. (1995). Development of a plasticity bond model for reinforced concrete: Theory and validation for monotonic applications.

[43] Cabrera, J. G. (1996). Deterioration of concrete due to reinforcement steel corrosion. *Cement and concrete composites*, 18(1), 47-59.

[44] Oliveira, R.S., Correa, M.R.S., Ramalho, M.A. (2000). A refined reinforced concrete beam element including bond-slip relationship, *Computational concrete structures technology*, 107–113.

[45] Monti, G., & Spacone, E. (2000). Reinforced concrete fiber beam element with bond-slip. *Journal of Structural Engineering*, 126(6), 654-661.

[46] Teng, J. G., Smith, S. T., Yao, J., & Chen, J. F. (2003). Intermediate crack-induced debonding in RC beams and slabs. *Construction and building materials*, 17(6-7), 447-462.

[47] Haddad, R. H., & Shannis, L. G. (2004). Post-fire behavior of bond between high strength pozzolanic concrete and reinforcing steel. *Construction and Building Materials*, 18(6), 425-435.

[48] Dominguez, N., Brancherie, D., Davenne, L., & Ibrahimbegović, A. (2005). Prediction of crack pattern distribution in reinforced concrete by coupling a strong discontinuity model of concrete cracking and a bond-slip of reinforcement model. *Engineering Computations*, 22(5/6), 558-582.

[49] Feldman, L. R., & Bartlett, F. M. (2005). Bond strength variability in pullout specimens with plain reinforcement. *ACI Structural Journal*, 102(6), 860.

[50] Xu, G., Wei, J., Tan, T., & Liu, H. Q. (2007). Modelling bond strength of corroded plain bar reinforcement in concrete. *Structural concrete*, 8(3), 133-138.

[51] Feldman, L. R., & Bartlett, F. M. (2007). Bond stresses along plain steel reinforcing bars in pullout specimens. *ACI Structural Journal*, 104(6), 685.

[52] Huang, Z. (2010). Modelling the bond between concrete and reinforcing steel in a fire. *Engineering Structures*, 32(11), 3660-3669.

[53] Prince, M. J. R., & Singh, B. (2015). Bond strength of deformed steel bars in high-strength recycled aggregate concrete. *Materials and Structures*, 48(12), 3913-3928.

[54] Shen, D., Shi, X., Zhang, H., Duan, X., & Jiang, G. (2016). Experimental study of early-age bond behavior between high strength concrete and steel bars using a pull-out test. *Construction and Building materials*, 113, 653-663.

[55] Tai, Y. S., & El-Tawil, S. (2017). High loading-rate pullout behavior of inclined deformed steel fibers embedded in ultra-high performance concrete. *Construction and Building Materials*, 148, 204-218.

[56] Wang, X., & Liu, X. (2003). A strain-softening model for steel–concrete bond. *Cement and Concrete Research*, 33(10), 1669-1673.

[57] Albarwary, I. H. M., & Haido, J. H. (2013). Bond strength of concrete with the reinforcement bars polluted with oil. *European Scientific Journal*, ESJ, 9(6).

[58] Drelich, J., & Mittal, K.L. (2005). Atomic Force Microscopy in Adhesion Studies, CRC Press.

[59] Jones, R., Pollock, H. M., Cleaver, J. A., & Hodges, C. S. (2002). Adhesion forces between glass and silicon surfaces in air studied by AFM: Effects of relative humidity, particle size, roughness, and surface treatment. *Langmuir*, 18(21), 8045-8055.

[60] Eastman, T., & Zhu, D. M. (1996). Adhesion forces between surface-modified AFM tips and a mica surface. *Langmuir*, 12(11), 2859-2862.

[61] Meng, J., Orana, A., Tan, T., Wolf, K., et al. (2010). Adhesion and interfacial fracture in drug-eluting stents. *Journal of Materials Research*, 25(4), 641-647.

[62] Tan, T., Meng, J., Rahbar, N., Li, H., Papandreou, G., Maryanoff, C. A., & Soboyejo, W. O. (2012). Effects of silane on the interfacial fracture of a parylene film over a stainless steel substrate. *Materials Science and Engineering: C*, 32(3), 550-557.

[63] Moy, V. T., Florin, E. L., & Gaub, H. E. (1994). Intermolecular forces and energies between ligands and receptors. *Science*, 266(5183), 257-259.

[64] Yang, J. (2004). AFM as a high-resolution imaging tool and a molecular bond force probe. *Cell biochemistry and biophysics*, 41(3), 435-449.

[65] Liu, C. (2005). Van der Waals force and asphalt concrete strength and cracking. *Journal of engineering mechanics*, 131(2), 161-166.

[66] Portland Cement Association (2002). Types and Causes of Concrete Deterioration, Portland Cement Association.

[67] Kerkhoff, B (2007). Effects of Substances on Concrete and Guide to Protective Treatments, Portland Cement Association, Skokie.

[68] Singh, A. K., & Das, G. S. (2016). Migration of chloride ion in the pore solution of reinforced Concrete steel bar. *IRJET*, 3(12), 786-795.

[69] Yousuf, M., Mollah, A., Vempati, R. K., Lin, T. C., & Cocke, D. L. (1995). The interfacial chemistry of solidification/stabilization of metals in cement and pozzolanic material systems. *Waste management*, 15(2), 137-148.

[70] Israelachvili, J.N. (2011). Intermolecular and Surface Forces, Academic press, Cambridge, MA.

[71] Kendall, K. (1994). Adhesion: molecules and mechanics. *Science*, 263(5154), 1720-1725.

[72] Kinloch, A.J. (2012). Adhesion and Adhesives: Science and Technology, Springer Science & Business Media, Berlin, Germany.

[73] Binnig, G., Rohrer, H., Gerber, C., & Weibel, E. (1982). Tunneling through a controllable vacuum gap. *Applied Physics Letters*, 40(2), 178-180.

[74] Binnig, G., Rohrer, H., Gerber, C., & Weibel, E. (1982). Surface studies by scanning tunneling microscopy. *Physical review letters*, 49(1), 57.

[75] Binnig, G., Quate, C. F., Gerber, C. (1986). Atomic Force Microscope, *Physical review letters*, 56(9):930-933

[76] Josef A. kas, Scanning Force Microscopy (SFM). available at http://home.uni-leipzig.de/pwm/web/?section=introduction&page=sfm

[77] Sarid, D. (1991). Scanning force microscopy. Oxford University Press, Oxford, UK.

[78] Loeber, L., Sutton, O., Morel, J. V. J. M., Valleton, J. M., & Muller, G. (1996). New direct observations of asphalts and asphalt binders by scanning electron microscopy and atomic force microscopy. *Journal of microscopy*, 182(1), 32-39.

[79] Jäger, A., Lackner, R., Eisenmenger-Sittner, C., & Blab, R. (2004). Identification of four material phases in bitumen by atomic force microscopy. *Road Materials and Pavement Design*, 5(sup1), 9-24.

[80] Masson, J. F., Leblond, V., & Margeson, J. (2006). Bitumen morphologies by phase-detection atomic force microscopy. *Journal of Microscopy*, 221(1), 17-29.

[81] Schmets, A., Kringos, N., Pauli, T., Redelius, P., & Scarpas, T. (2010). On the existence of wax-induced phase separation in bitumen. *International Journal of Pavement Engineering*, 11(6), 555-563.

[82] Pauli, A. T., Grimes, R. W., Beemer, A. G., Turner, T. F., & Branthaver, J. F. (2011). Morphology of asphalts, asphalt fractions and model wax-doped asphalts studied by atomic force microscopy. *International Journal of Pavement Engineering*, 12(4), 291-309.

[83] Zhang, H. L., Wang, H. C., & Yu, J. Y. (2011). Effect of aging on morphology of organo-montmorillonite modified bitumen by atomic force microscopy. *Journal of microscopy*, 242(1), 37-45.

[84] Lyne, Å. L., Wallqvist, V., & Birgisson, B. (2013). "Adhesive surface characteristics of bitumen binders investigated by atomic force microscopy." *Fuel*, 113, 248-256.

[85] De Moraes, M. B., Pereira, R. B., Simão, R. A., & Leite, L. F. M. (2010). High temperature AFM study of CAP 30/45 pen grade bitumen. *Journal of Microscopy*, 239(1), 46-53.

[86] Das, P. K., Kringos, N., Wallqvist, V., & Birgisson, B. (2013). Micromechanical investigation of phase separation in bitumen by combining atomic force microscopy with differential scanning calorimetry results. *Road Materials and Pavement Design*, 14(sup1), 25-37.

[87] Nahar, S. N., Schmets, A. J. M., Scarpas, A., & Schitter, G. (2013). Temperature and thermal history dependence of the microstructure in bituminous materials. *European Polymer Journal*, 49(8), 1964-1974.

[88] Soenen, H., Besamusca, J., Fischer, H. R., et al. (2014). Laboratory investigation of bitumen based on round robin DSC and AFM tests. *Materials and structures*, 47(7), 1205-1220.

[89] Gong, M., Yang, J., Zhang, J., Zhu, H., & Tong, T. (2016). Physical-chemical properties of aged asphalt rejuvenated by bio-oil derived from biodiesel residue. *Construction and Building materials*, 105, 35-45.

[90] Xu, M., Yi, J., Pei, Z., Feng, D., Huang, Y., & Yang, Y. (2017). Generation and evolution mechanisms of pavement asphalt aging based on variations in surface structure and micromechanical characteristics with AFM. *Materials Today Communications*, 12, 106-118.

[91] Wang, Z., Chang, R., Zhou, Z., Qin, Y., & Wang, G. (2018). Investigation of the Asphalt Binder Sample Preparation Methods Based on AFM. In RILEM 252-CMB-Symposium on Chemo Mechanical Characterization of Bituminous Materials (pp.156-161). Springer, Cham.

[92] Arnold, T. S., & Shastry, A. (2015). Analysis of asphalt binders for recycled engine oil bottoms by X-ray fluorescence spectroscopy. Trans. Res. Board 94th Annual Meeting, Washington, DC.

[93] Greenfield, M. L., Byrne, M., Mitra-Kirtley, S., Kercher, E. M., Bolin, T. B., Wu, T., Craddock, P. R., Bake, K. D. & Pomerantz, A. E. (2015). XANES measurements of sulfur chemistry during asphalt oxidation. *Fuel*, 162, 179-185.

[94] Tarefder, R. A., & Zaman, A. M. (2010). Nanoscale evaluation of moisture damage in polymer modified Asphalts. *Journal of Materials in Civil Engineering*, 22(7), 714-725.

[95] Nazzal, M. D., Abu-Qtaish, L., Kaya, S., & Powers, D. (2015). Using atomic force microscopy to evaluate the nanostructure and nanomechanics of warm mix asphalt. *Journal of Material in Civil Engineering*, 27(10), 04015005.

[96] Das, P. K., Baaj, H., Tighe, S., & Kringos, N. (2015). Atomic force microscopy to investigate asphalt binders: a state-of-the-art review. *Road Materials and Pavement Design*, 1-26.

[97] Yu, X., Burnham, N. A., Mallick, R. B., Tao, M. (2013). A systematic AFM-based method to measure adhesion differences between micron-sized domains in asphalt binders. *Fuel*, 113, 443-447.

[98] Allen, R. G., Little, D. N., Bhasin, A. (2012). Structural characterization of micromechanical properties in asphalt using atomic force microscopy. *Journal of Materials in Civil Engineering*, 24(10):1317-1327.

[99] Arifuzzaman, M., Islam, M. S., & Hossain, M. I. (2017). Moisture damage evaluation in SBS and lime modified asphalt using AFM and artificial intelligence. *Neural Computing and Applications*, 28(1), 125-134.

[100] Yao, Z., Zhu, H., Gong, M., Yang, J., Xu, G., & Zhong, Y. (2017). Characterization of asphalt materials' moisture susceptibility using multiple methods. *Construction and Building Materials*, 155, 286-295.

[101] Gong, M., Yao, Z., Xiong, Z., Yang, J., & Hong, J. (2018). Investigation on the influences of moisture on asphalts' micro properties by using atomic force microscopy and Fourier transform infrared spectroscopy. *Construction and Building Materials*, 183, 171-179.

[102] Liu, W. K., Park, H. S., Qian, D., Karpov, E. G., Kadowaki, H., & Wagner, G. J. (2006). Bridging scale methods for nanomechanics and materials. *Computer Methods in Applied Mechanics and Engineering*, 195(13), 1407-1421.

[103] Kim, Y. R., Allen, D. H., & Little, D. N. (2007). Computational constitutive model for predicting nonlinear viscoelastic damage and fracture failure of asphalt concrete mixtures. *International Journal of Geomechanics*, 7(2), 102-110.

[104] Kim, H., & Buttlar, W. G. (2009). Discrete fracture modeling of asphalt concrete. *Journal of materials in civil Engineering*, 46(13), 2593-2604.

[105] Hogshead, C. G., Manias, E., Williams, P., Lupinsky, A., & Painter, P. (2010). Studies of bitumen-silica and oil-silica interactions in ionic liquids. *Energy & Fuels*, 25(1), 293-299.

[106] Fan, J. (2011). Multiscale analysis of deformation and failure of materials. Wiley, West Sussex, UK.

[107] Al-Rawashdeh, A. S., & Sargand, S. (2013). Performance assessment of warm asphalt binder in presence of water by using surface free energy concepts and nano-scale techniques. *Journal of Material in Civil Engineering*, 26(5), 803-811.

[108] Kumar, K., Dao, E., Mohanty, K. K. (2005). AFM study of mineral wettability with reservoir oils. *Journal of colloid and interface science*, 289(1), 206-217.

[109] Fischer, H. R., Dillingh, E. C., Hermse, C. G. M. (2013). On the interfacial interaction between bituminous binders and mineral surfaces as present in asphalt mixtures. *Applied Surface Science*, 265, 495-499.

[110] Hogshead, C. G., Manias, E., Williams, P., Lupinsky, A., Painter, P. (2011). Studies of bitumen−silica and oil−silica interactions in ionic liquids. *Energy & Fuels*, 25(1), 293-299.

[111] Khodaii, A., Haghshenas, H.F. & Tehrani, H.K. (2012). Effect of grading and lime content on HMA stripping using statistical methodology. *Construction and Building Materials*, 34, 131-135.

[112] Kavussi, A., Qorbani, M., Khodaii, A. & Haghshenas, H.F. (2014). Moisture susceptibility of warm mix asphalt: a statistical analysis of the laboratory testing results. *Construction and Building Materials*, 52, 511-517.

[113] Liu, S., Cao, W., Fang, J. & Shang, S. (2009). Variance analysis and performance evaluation of different crumb rubber modified (CRM) asphalt. *Construction and Building Materials*, 23(7), 2701-2708.

[114] Mangiafico, S., Di Benedetto, H., Sauzéat, C., Olard, F., Pouget, S., Dupriet, S., Planque, L. & Van Rooijen, R. (2015). Statistical analysis of the influence of RAP and mix composition on viscoelastic and fatigue properties of asphalt mixes. *Materials and Structures*, 48(4), 1187-1205.

[115] Moghaddam, T.B., Soltani, M. & Karim, M.R. (2015). Stiffness modulus of polyethylene terephthalate modified asphalt mixture: a statistical analysis of the laboratory testing results. *Materials & Design*, 68, 88-96.

[116] Maragliano, C., Glia, A., Stefancich, M., & Chiesa, M. (2014). Effective AFM cantilever tip size: methods for in-situ determination. *Measurement Science and Technology*, 26(1), 015002.

[117] Nawy, E. (2008). Reinforced Concrete: A Fundamental Approach. 6th ed. New York, NY: Prentice Hall.

[118] Lutz, L. A., & Gergely, P. (1967). Mechanics of bond and slip of deformed bars in concrete. *Journal Proceedings*, 64(11), 711-721.

[119] Tabor, D. (1981). Principles of adhesion-bonding in cement and concrete. In *Adhesion problems in the recycling of concrete* (pp. 63-87). Springer, Boston, MA.

[120] Scrivener, K. L., Crumbie, A. K., & Laugesen, P. (2004). The interfacial transition zone (ITZ) between cement paste and aggregate in concrete. *Interface science*, 12(4), 411-421.

[121] Angst, U. M., Geiker, M. R., Michel, A., Gehlen, et al. (2017). The steel-concrete interface. *Materials and Structures*, 50(2), 143.

[122] Pinchin, D. J., & Tabor, D. (1978). Interfacial phenomena in steel fibre reinforced cement I: Structure and strength of interfacial region. *Cement and concrete research*, 8(1), 15-24.

[123] Pinchin, D. J., & Tabor, D. (1978). Interfacial phenomena in steel fibre reinforced cement II: Pull-out behaviour of steel wires. *Cement and concrete research*, 8, 139-150.

[124] Withey, M.O. (1909). Tests on bond between concrete and steel in reinforced concrete beams. Bulletin of the University of Wisconsin, 321, Engineering Series, 5, 407-470.

[125] Abrams, D. A. (1913). Tests of bond between concrete and steel. Bulletin No. 71, University of Illinois at Urbana Champaign, College of Engineering, Engineering Experiment Station.

[126] Slater, W. A., Richart, F. E., & Scofield, G. G. (1920). Tests of bond resistance between concrete and steel. Technical Paper No. 173, National Bureau of Standards, 9-33.

[127] Clark, A. P. (1949). Bond of Concrete to Reinforcing Bars. *Journal Proceedings*, 46, 161-184.

[128] Bird, C. E. (1962). Bond of galvanized steel reinforcement in concrete. *Nature*, 194, 798.

[129] Wang, C. Y. (1963). A study of bond stress between concrete and steel. Master Thesis, Kansas State University, Kansas.

[130] Brown, C. B. (1966). Bond failure between steel and concrete. *Journal of the Franklin Institute*, 282(5), 271-290.

[131] ASTM Standards C900-87 (1987). Test Method for Pullout Strength of Hardened Concrete.

[132] Xu, G., Wei, J., Tan, T., & Liu, H. Q. (2007). Modelling bond strength of corroded plain bar reinforcement in concrete. *Structural concrete*, 8(3), 133-138.

[133] Chapman, R. A., & Shah, S. P. (1987). Early-age bond strength in reinforced concrete. *Materials Journal*, 84(6), 501-510.

[134] Fu, X., & Chung, D. D. L. (1997). Effect of curing age on the self-monitoring behavior of carbon fiber reinforced mortar. *Cement and concrete Research*, 27(9), 1313-1318.

[135] Fu, X., & Chung, D. D. L. (1998). Effects of Water-Cement Ratio, Curing Age, Silica Fume, Polymer Admixtures, Steel Surface Treatments and Corrosion on the Bond between Concrete and Steel Reinforcing Bar. *Materials Journal*, 95(6), 725-734.

[136] Fu, X., & Chung, D. D. L. (1998). Interface between steel rebar and concrete, studied by electromechanical pull-out testing. *Composite Interfaces*, 6(2), 81-92.

[137] du Béton FI (2000). Bond of reinforcement in concrete: state-of-art report. Bulletin, 10, 160-167.

[138] Harajli, M. H. (2004). Comparison of bond strength of steel bars in normal-and high-strength concrete. *Journal of materials in Civil Engineering*, 16(4), 365-374.

[139] Shen, D., Shi, X., Zhang, H., Duan, X., & Jiang, G. (2016). Experimental study of early-age bond behavior between high strength concrete and steel bars using a pull-out test. *Construction and Building materials*, 113, 653-663.

[140] Sulaiman, M. F., Ma, C. K., Apandi, N. M., Chin, S., Awang, A. Z., Mansur, S. A., & Omar, W. (2017). A review on bond and anchorage of confined high-strength concrete. *Structures*, 11, 97-109.

[141] Hossain, K. M. A. (2008). Bond characteristics of plain and deformed bars in lightweight pumice concrete. *Construction and Building Materials*, 22(7), 1491-1499.

[142] Zhao, Y., Lin, H., Wu, K., & Jin, W. (2013). Bond behaviour of normal/recycled concrete and corroded steel bars. *Construction and building materials*, 48, 348-359.

[143] Seara-Paz, S., González-Fonteboa, B., Eiras-López, J., & Herrador, M. F. (2014). Bond behavior between steel reinforcement and recycled concrete. *Materials and structures*, 47(1-2), 323-334.

[144] Zhu, W., Sonebi, M., & Bartos, P. J. M. (2004). Bond and interfacial properties of reinforcement in self-compacting concrete. *Materials and structures*, 37(7), 442.

[145] Lynch L, Weiss C, Day D, Tom J, Malone P, Hackler C, et al. (2008). Chemical bonding of concrete and steel reinforcement using a vitreous enamel coupling layer. Ceramic Engineering and Science Proceeding (Vol. 28, No. 10, p. 81). American Ceramic Society.

[146] Page, C. L., Al Khalaf, M. N., & Ritchie, A. G. B. (1978). Steel/mortar interfaces: Mechanical characteristics and electrocapillarity. *Cement and Concrete Research*, 8(4), 481-490.

[147] Al Khalaf, M. N., & Page, C. L. (1979). Steel/mortar interfaces: microstructural features and mode of failure. *Cement and Concrete Research*, 9(2), 197-207.

[148] Montgomery, D. G., & Samarin, A. (1987). Adhesion between concrete and treated or untreated flat metal surfaces. *MRS Online Proceedings Library Archive*, 114.

[149] Lacuve, M., Chougnet, A., Allouche, M., & Mazard, C. (2015). A Method to Improve Adhesion Strength at the Cement/Steel-Casing Interface and its Effect on Cement Evaluation Log Response. In Offshore Mediterranean Conference and Exhibition. Offshore Mediterranean Conference.

[150] ZHANG, Z., SCHERER, G. W., & PRUD'HOMME, R. K. (2016). Adhesion and bonding between steel pipe and cement/spacer/mud system. In *9th International*

Conference on Fracture Mechanics of Concrete and Concrete Structures (FraMCoS-9).

[151] Axelsson, H., Darwin, D., & Locke Jr, C. E. (1999). Influence of Adhesion at Steel/mortar Interface on Corrosion Characteristics of Reinforcing Steel. University of Kansas Center for Research, Inc.

[152] Han, J., Carey, J. W., & Zhang, J. (2010). Assessing the effect of cement-steel interface on well casing corrosion in aqueous CO2 environments (No. LA-UR-10-02608; LA-UR-10-2608). Los Alamos National Lab.(LANL), Los Alamos, NM (United States).

[153] Garbacz, A., Courard, L., & Bissonnette, B. (2013). A surface engineering approach applicable to concrete repair engineering. *Bulletin of the Polish Academy of Sciences: Technical Sciences*, 61(1), 73-84.

[154] Bissonnette, B., Courard, L., & Garbacz, A. (2015). Concrete surface engineering. CRC Press.

[155] Lomboy, G., Sundararajan, S., Wang, K., & Subramaniam, S. (2011). A test method for determining adhesion forces and Hamaker constants of cementitious materials using atomic force microscopy. *Cement and Concrete Research*, 41(11), 1157-1166.

[156] Li, Y., Yang, J., & Tan, T. (2015). Study on adhesion between asphalt binders and aggregate minerals under ambient conditions using particle-modified atomic force microscope probes. *Construction and Building Materials*, 101, 159-165.

[157] Li, Y., Yang, J., & Tan, T. (2016). Measuring adhesion between modified asphalt binders and aggregate minerals: use of particle probe scanning force microscopes. *Transportation Research Record: Journal of the Transportation Research Board*, (2574), 117-123.

[158] Li, Y., Yang, J., & Tan, T. (2017). Adhesion between modified binders and aggregate minerals at ambient conditions measured with particle-probe scanning force microscopes. *Journal of Materials in Civil Engineering*, 29(8), 04017068.

[159] Li, Y., Yang, J., & Tan, T. (2017). Statistical Analyses of Aggregate Mineral–Binder Adhesion: Measuring with Particle Probe Scanning Force Microscopes. *Transportation Research Record: Journal of the Transportation Research Board*, (2632), 25-31.

[160] Li, Y., Yang, J., & Tan, T. (2018). Measuring adhesion between steel and early-hydrated Portland cement using particle probe scanning force microscopy. *Cement and Concrete Composites*, 90, 126-135.

[161] Baldino, N., Gabriele, D., Rossi, C. O., Seta, L., Lupi, F. R., & Caputo, P. (2012). Low temperature rheology of polyphosphoric acid (PPA) added bitumen. *Construction and Building Materials*, 36, 592-596.

[162] Yang, J., & Rau, D. C. (2005). Incomplete ion dissociation underlies the weakened attraction between DNA helices at high spermidine concentrations. *Biophysical journal*, 89(3), 1932-1940.

[163] Hutter, J. L., & Bechhoefer, J. (1993). Calibration of atomic- force microscope tips. *Review of Scientific Instruments*, 64(7), 1868-1873.

[164] Butt, H. J., & Jaschke, M. (1995). Calculation of thermal noise in atomic force microscopy. *Nanotechnology*, 6(1), 1.

[165] Hutter, J. L. (2005). Comment on tilt of atomic force microscope cantilevers: effect on spring constant and adhesion measurements. *Langmuir*, 21(6), 2630-2632.

[166] Asylum Research, an Oxford Instrument company (2013). Application Guide, version.13, revision A-1714, dated 10/25/2013.

[167] Cramér, H. (1946). Mathematical methods of statistics (PMS-9) (Vol. 9). Princeton university press.

[168] Coolen, F. (2008). Parametric probability distributions in reliability. *Encyclopedia of Quantitative Risk Analysis and Assessment*.

[169] Cai, W. (2014). Making Comparisons Fair: How LS-Means Unify the Analysis of Linear Models. *SAS Institute Inc. Paper, SA*, S060-2014.

[170] JMP, A., & Proust, M. (2012). Modeling and Multivariate Methods.

[171] Bretscher, Otto (1995). Linear Algebra with applications (3rd ed.). Upper Saddle River, NJ: Prentice Hall.

[172] Cheng, D., Little, D., Lytton, R., & Holste, J. (2003). Moisture damage evaluation of asphalt mixtures by considering both moisture diffusion and repeated-load conditions. *Transportation research record: journal of the transportation research board*, (1832), 42-49.

[173] Derjaguin, B. V., Muller, V. M., & Toporov, Y. P. (1994). Effect of contact deformations on the adhesion of particles. *Progress in Surface Science*, 45(1-4), 131-143.

[174] Popov, V. L. (2010). Contact mechanics and friction (pp. 231-253). Berlin: Springer Berlin Heidelberg.

[175] Touchstone J. C. (1992). Practice of thin layer chromatography: John Wiley & Sons.

[176] Chromatographic Mechanisms, available at http://www.separationprocesses.com/Adsorption/AD_Chp05a.htm#TopPage, (accessed 2013.11.5).

[177] Good, R. J. (1992). Contact angle, wetting, and adhesion: a critical review. *Journal of adhesion science and technology*, 6(12), 1269-1302.

[178] Kogut, L., & Etsion, I. (2003). Adhesion in elastic-plastic spherical microcontact. *Journal of Colloid and Interface Science*, 261(2), 372-378.

[179] Butt, H. J., Graf, K., & Kappl, M. (2006). Physics and chemistry of interfaces. John Wiley & Sons.

[180] Little, D. N., & Bhasin, A. (2006). Using surface energy measurements to select materials for asphalt pavement (No. NCHRP Project 9-37).

[181] dos Santos, S., Partl, M. N., & Poulikakos, L. D. (2015). From virgin to recycled bitumen: A microstructural view. *Composites Part B: Engineering*, 80, 177-185.

[182] Jahangir, R., Little, D., & Bhasin, A. (2015). Evolution of asphalt binder microstructure due to tensile loading determined using AFM and image analysis techniques. *International Journal of Pavement Engineering*, 16(4), 337-349.

[183] Mindess, S., Young, J. F., & Darwin, D. (1981). Concrete, prentice hall. Englewood Cliffs, NJ, 481.

[184] Zhang, J., & Scherer, G. W. (2011). Comparison of methods for arresting hydration of cement. *Cement and Concrete Research*, 41(10), 1024-1036.

[185] Zhang, Z., & Scherer, G. W. (2017). Supercritical drying of cementitious materials. *Cement and Concrete Research*, 99, 137-154.

[186] Lilkov, V., Petrov, O., Tzvetanova, Y., & Savov, P. (2012). Mössbauer, DTA and XRD study of Portland cement blended with fly ash and silica fume. *Construction and Building Materials*, 29, 33-41.

[187] Kamat, S., Su, X., Ballarini, R., & Heuer, A. H. (2000). Structural basis for the fracture toughness of the shell of the conch Strombus gigas. *Nature*, 405(6790), 1036.

[188] Alghamdi, S., Tan, T., Hale-Sills, C., et al. (2017). Catastrophic failure of nacre under pure shear stresses of torsion. *Scientific reports*, 7(1), 13123.

[189] Shin, Y. A., Yin, S., Li, X., et al. (2016). Nanotwin-governed toughening mechanism in hierarchically structured biological materials. *Nature communications*, 7, 10772.

[190] Tegethoff, F. W., Rohleder, J., Kroker, E., eds. (2001). Calcium carbonate: from the Cretaceous period into the 21st century. Springer Science & Business Media.

[191] Taylor, H. F. W. (1997). Cement Chemistry. London: Thomas Telford.

[192] Matschei, T., Lothenbach, B., & Glasser, F. P. (2007). The role of calcium carbonate in cement hydration. *Cement and Concrete Research*, 37(4), 551-558.

[193] Atkinson, A., Hearne, J. A., & Knights, C. F. (1989). Aqueous chemistry and thermodynamic modelling of CaO-SiO_2-H_2O gels. *Journal of the Chemical Society, Dalton Transactions*, (12), 2371-2379.

[194] Harris, A. W., Manning, M. C., Tearle, W. M., & Tweed, C. J. (2002). Testing of models of the dissolution of cements—leaching of synthetic CSH gels. *Cement and Concrete Research*, 32(5), 731-746.

[195] Mori, D., & Yamada, K. (2007). A review of recent applications of EPMA to evaluate the durability of concrete. *Journal of Advanced Concrete Technology*, 5(3), 285-298.

[196] Duguid, A., & Scherer, G. W. (2010). Degradation of oilwell cement due to exposure to carbonated brine. *International Journal of Greenhouse Gas Control*, 4(3), 546-560.

[197] De Leon, A. R., & Chough, K. C. (Eds.). (2013). Analysis of mixed data: methods & applications. CRC Press.

[198] Georgios, C., & Ulm, F. J. (2007). The nanogranular nature of CSH. *J Mech Phys Solids*, 55, 64-90.

[199] Jennings, H. M., & Tennis, P. D. (1994). Model for the developing microstructure in Portland cement pastes. *Journal of the American Ceramic Society*, 77(12), 3161-3172.

[200] Tennis, P. D., & Jennings, H. M. (2000). A model for two types of calcium silicate hydrate in the microstructure of Portland cement pastes. *Cement and concrete research*, 30(6), 855-863.

[201] Bullard, J. W., Jennings, H. M., Livingston, R. A., et al. (2011). Mechanisms of cement hydration. *Cement and concrete research*, 41(12), 1208-1223.

[202] Thomas, J. J., Biernacki, J. J., Bullard, J. W., Bishnoi, S., Dolado, J. S., Scherer, G. W., & Luttge, A. (2011). Modeling and simulation of cement hydration kinetics and microstructure development. *Cement and concrete research*, 41(12), 1257-1278.

[203] Scherer, G. W. (2012). Models of confined growth. *Cement and Concrete Research*, 42(9), 1252-1260.

[204] Taylor, H. F. (1987). A method for predicting alkazi ion concentrations in cement pore solutions. *Advances in Cement Research*, 1(1), 5-17.

[205] Weisenhorn, A. L., Hansma, P. K., Albrecht, T. R., & Quate, C. F. (1989). Forces in atomic force microscopy in air and water. *Applied Physics Letters*, 54(26), 2651-2653.

[206] Leite, F. L., Riul, A., & Herrmann, P. S. P. (2003). Mapping of adhesion forces on soil minerals in air and water by atomic force spectroscopy (AFS). *Journal of adhesion science and technology*, 17(16), 2141-2156.

[207] Constantinides, G. (2006). Invariant mechanical properties of calcium-silicate-hydrates (CHS) in cement-based materials: instrumented nanoindentation and microporomechanical modeling (Doctoral dissertation, Massachusetts Institute of Technology).

[208] Constantinides, G., & Ulm, F. J. (2004). The effect of two types of CSH on the elasticity of cement-based materials: Results from nanoindentation and micromechanical modeling. *Cement and concrete research*, 34(1), 67-80.

[209] Timashev, V. V. (1980). The Kinetics of Clinker Formation The Structure and Composition of Clinker and its Phases. in 7th ICCC, 1.

[210] Reardon, E. J., James, B. R., & Abouchar, J. (1989). High pressure carbonation of cementitious grout. *Cement and concrete research*, 19(3), 385-399.

[211] Groves, G. W., Brough, A., Richardson, I. G., & Dobson, C. M. (1991). Progressive changes in the structure of hardened C3S cement pastes due to carbonation. *Journal of the American Ceramic Society*, 74(11), 2891-2896.

[212] Castellote, M., Fernandez, L., Andrade, C., & Alonso, C. (2009). Chemical changes and phase analysis of OPC pastes carbonated at different CO 2 concentrations. *Materials and Structures*, 42(4), 515-525.

[213] Thomas J, Jennings HM. The science of concrete. http://www.iti.northwestern.edu/cement/index.html (accessed 2016.5.23).

[214] Liu, R., Han, F., & Yan, P. (2013). Characteristics of two types of CSH gel in hardened complex binder pastes blended with slag. *Science China Technological Sciences*, 56(6), 1395-1402.

[215] Morandeau, A., Thiery, M., & Dangla, P. (2014). Investigation of the carbonation mechanism of CH and CSH in terms of kinetics, microstructure changes and moisture properties. *Cement and Concrete Research*, 56, 153-170.

[216] Durdziński, P. T., Dunant, C. F., Haha, M. B., & Scrivener, K. L. (2015). A new quantification method based on SEM-EDS to assess fly ash composition and study the reaction of its individual components in hydrating cement paste. *Cement and Concrete Research*, 73, 111-122.

Appendix 1

Contamination of Probes

Considering the contaminations of probes, the probes were checked before and after measurements. Fig.1 and 2 shows the bare tip and steel particle modified probe before (a) and after (b) one matrix measurements. After the measurements, there are a few residues existed on the cantilevers, but the contact area of probes is clean. Fig.3 shows the particle probes after three matrices measurements, the residues have wrapped the particles. Thus, we designed our experiments using one probe to measure one matrix.

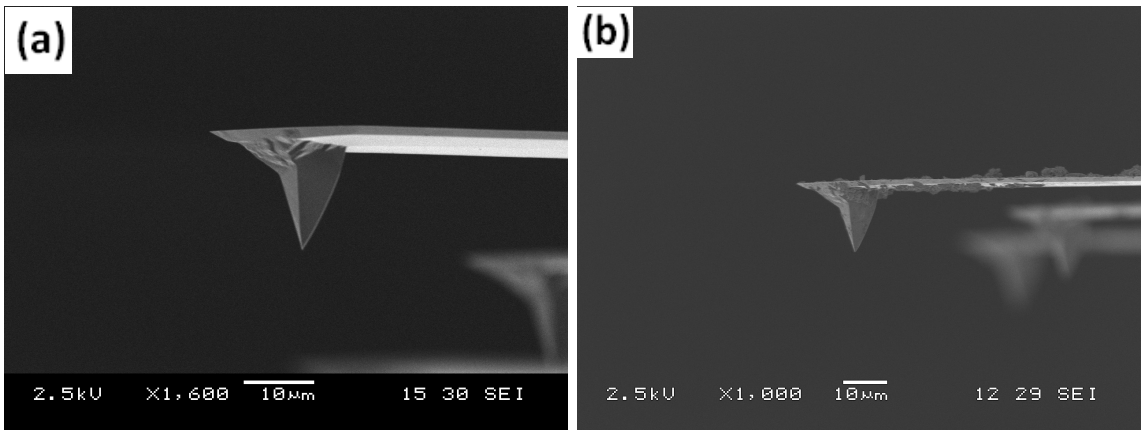

Figure 1: Commercial SFM probe before (a) and after (b) one matrix measurements.

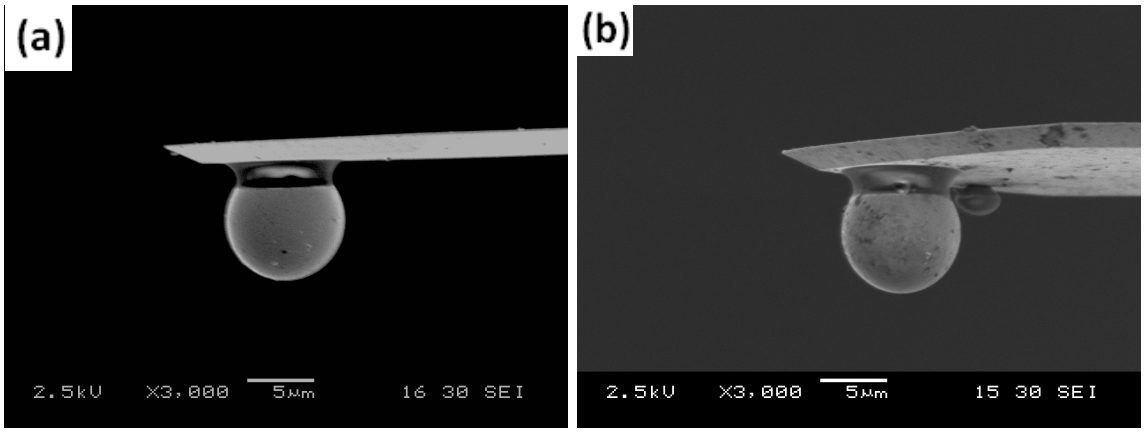

Figure 2: Steel particle modified probe before (a) and after (b) one matrix measurements.

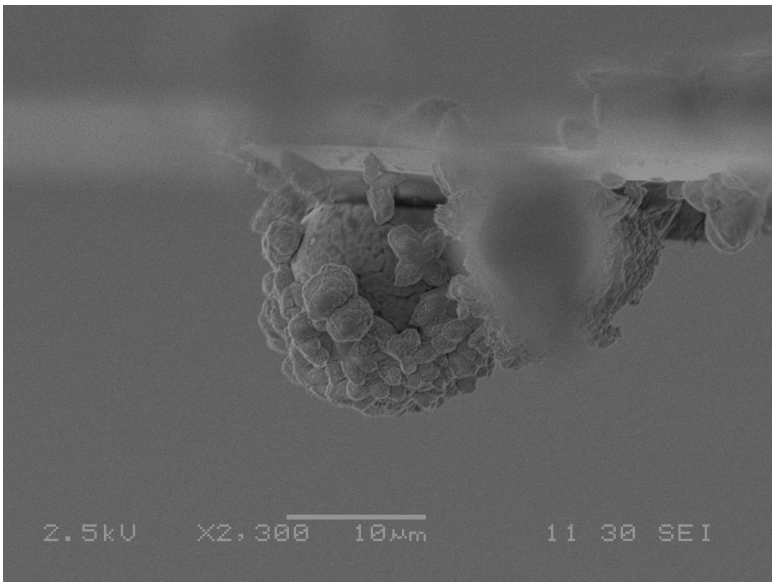

Figure 3: Steel particle modified probe after three matrices measurements.

Appendix 2

Program of the mixed Gaussian model

```
import matplotlib.pyplot as plt
from math import exp, sqrt
import csv
import numpy as np
from scipy.stats import gaussian_kde
from sklearn.mixture import GaussianMixture as GMM


def floatrange(start, stop, steps):
    ''' Computes a range of floating value.
        Input:
            start (float)  : Start value.
            stop   (float)  : stop value
            steps (integer): Number of values
        Output:
            A list of floats
    '''
    return [start + float(i) * (stop - start) / (float(steps) - 1) for i in
range(steps)]

#export raw data from excel file
def raw_data (workfile, number):
    raw_data_column = []
    with open(workfile, 'r') as csvFile:
        csvData = csv.reader(csvFile)
        headings = next(csvFile)
        for line in csvData:
            raw_data_column.append(float(line[number]))
    return raw_data_column


p = raw_data('workbook1.csv', 0)

# plot the frequency density curve for experimental data
def frequency_density(data, number):
    data_size = float(len(data))
    hist, bin_edges = np.histogram(data, bins = number)
    hist = hist.tolist()
    bin_edges = bin_edges.tolist()
    #print(hist)
    #print(bin_edges)
    bin_length = float(bin_edges[1]-bin_edges[0])
    y = []
    x = []

    for i in range(len(bin_edges)-1):
        a = float(bin_edges[i])
        c = a + bin_length/2
        x.append(c)
    #print(x)
```

```
    for i in range(len(hist)):
        n = float(hist[i])
        n = n/(data_size*bin_length)
        y.append(n)
    return (x,y)

experimental_data = frequency_density(p,17)
#print(experimental_data)
x0 = list(experimental_data[0])
y0 = list(experimental_data[1])

density = gaussian_kde(p)
xs = np.linspace(0, 200, 370)
density.covariance_factor = lambda: .15
density._compute_covariance()

def Gaussian_distribution_mixture(raw_data):
    data = []
    data = np.array(raw_data)
    clf1 = GMM(n_components=5, max_iter=1000, covariance_type='full',
random_state=3).fit(data)
    xpdf1 = np.linspace(0, 200, 370)
    density1 = [np.exp(clf1.score(x)) for x in xpdf1]
    return (clf1.means_, clf1.covariances_, clf1.weights_)

fitting_data = Gaussian_distribution_mixture(p)
#print(fitting_data)
mean = list(fitting_data[0])
variance = list(fitting_data[1])
weights = list(fitting_data[2])

def single_normal(fitting_mean, fitting_var, fitting_weights):
    x = floatrange(0,200, 180)
    y = []
    for i in range(0, 180, 1):
        n = exp(-((x[i]-
fitting_mean)**2)/(2*fitting_var))/sqrt(2*3.1415926*fitting_var)
        n = n*fitting_weights
        y.append(n)
    return (x, y)

def all_normal_4(data_1, data_2, data_3, data_4):
    x = []
    y = []
    for i in range(len(data_1[0])):
        m = data_1[0][i]
        n = data_1[1][i]+data_2[1][i]+data_3[1][i]+data_4[1][i]
        x.append(m)
        y.append(n)
    return (x, y)

def all_normal_5(data_1, data_2, data_3, data_4, data_5):
    x = []
    y = []
    for i in range(len(data_1[0])):
        m = data_1[0][i]
        n = data_1[1][i]+data_2[1][i]+data_3[1][i]+data_4[1][i]+data_5[1][i]
        x.append(m)
        y.append(n)
    return (x, y)
```

```
curve_1 = single_normal(mean[0], variance[0], weights[0])
curve_2 = single_normal(mean[1], variance[1], weights[1])
curve_3 = single_normal(mean[2], variance[2], weights[2])
curve_4 = single_normal(mean[3], variance[3], weights[3])
curve_5 = single_normal(mean[4], variance[4], weights[4])
#curve_all = all_normal_4(curve_1,curve_2,curve_3,curve_4)
curve_all = all_normal_5(curve_1,curve_2,curve_3,curve_4,curve_5)


x1 = list(curve_1[0])
y1 = list(curve_1[1])
x2 = list(curve_2[0])
y2 = list(curve_2[1])
x3 = list(curve_3[0])
y3 = list(curve_3[1])
x4 = list(curve_4[0])
y4 = list(curve_4[1])
x5 = list(curve_5[0])
y5 = list(curve_5[1])
x_all = list(curve_all[0])
y_all = list(curve_all[1])

print(x_all)
print(x2)
p = np.array(p)
p = p[:,np.newaxis]
clf5 = GMM(n_components=4, max_iter=1000, covariance_type='full',
random_state=3).fit(p)
xpdf5 = np.linspace(0, 160, 500)
density5 = [np.exp(clf5.score(x)) for x in xpdf5]


#plot all curves in one graph
fig_curve = plt.figure(figsize=(12, 6))
plt.plot(x0, y0, 'ko-')
plt.plot(x_all, y_all, '-r')
#plt.plot(xs, density(xs), '-b')
plt.plot(x1, y1, '-m')
plt.plot(x2, y2, '-m')
plt.plot(x3, y3, '-m')

plt.plot(x4, y4, '-m')
plt.plot(x5, y5, '-m')
plt.plot(xpdf5, density5, '-b')
for i in range(clf5.n_components):
   pdf = clf5.weights_[i] * stats.norm(clf5.means_[i, 0],
np.sqrt(clf5.covariances_[i, 0])).pdf(xpdf5)
   plt.fill(xpdf5, pdf, facecolor='green', edgecolor='none', alpha=0.3)
plt.plot(x5, y5, '-m')
plt.legend(["frequency density", "fitting","kernel density estimation"],
fontsize=12)
plt.legend(["experimental pdf", "fitting pdf"], fontsize=12)
plt.xlim(0, 120)
fig_curve.suptitle('pH=12 Cl=0 (Bin size = 17)', fontsize=20)
plt.xlabel('Adhesive force (nN)', fontsize=18)
plt.ylabel('Frequency density', fontsize=16)
plt.show()
fig_curve.savefig('pH12_Cl0-1.png')
```

Appendix 3

One example to calculate the spring constant of probe

Step 1: engage the probe to make it contact to the substrate as shown in Fig.4, and click on the withdraw button to move the tip back away from the surface.

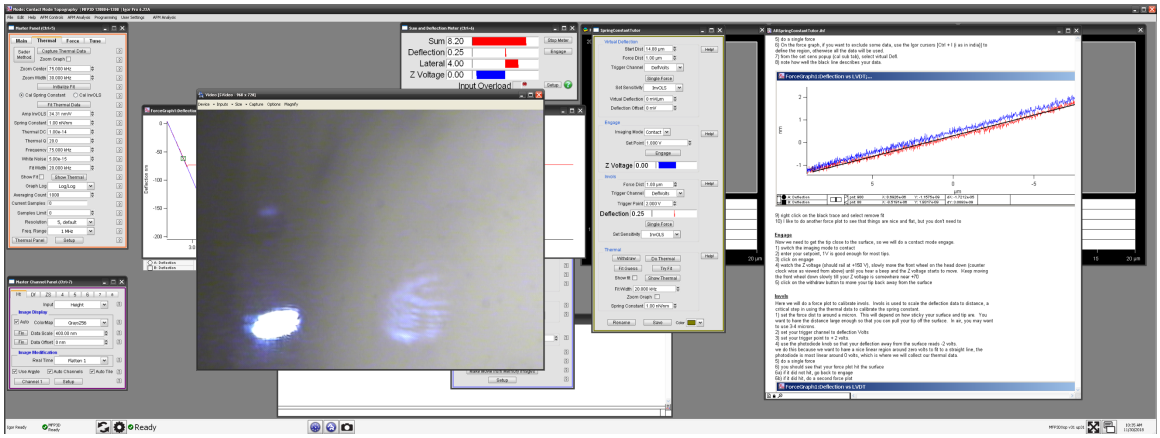

Figure 4

Step 2: do a force to calibrate Invols as shown in Fig. 5. Invols is used to scale the deflection data to distance, a critical step in using the thermal data to calibrate the spring constant.

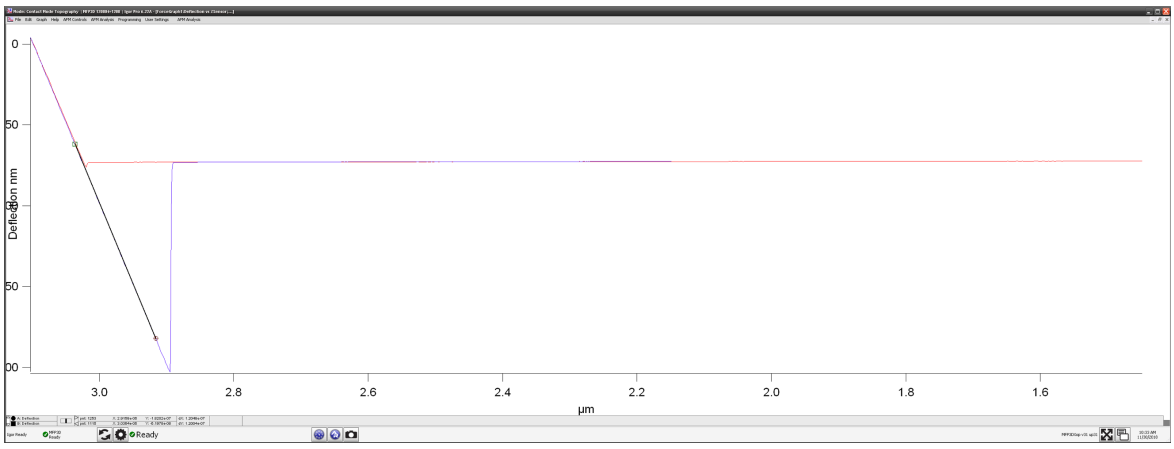

Figure 5

Step 3: collect the thermal data and calibrate the spring constant. Fig. 6 shows the thermal collecting, stop it after 200 measurements. On the thermal graph in Fig. 7, draw a box around the thermal peak, which is the first (lowest frequency) highest peak generally, and zoom it up. After that, click on the fit guess button and try fit button to actually fit the data in Fig.8. At last, the spring constant was calibrated and was shown in Fig.9.

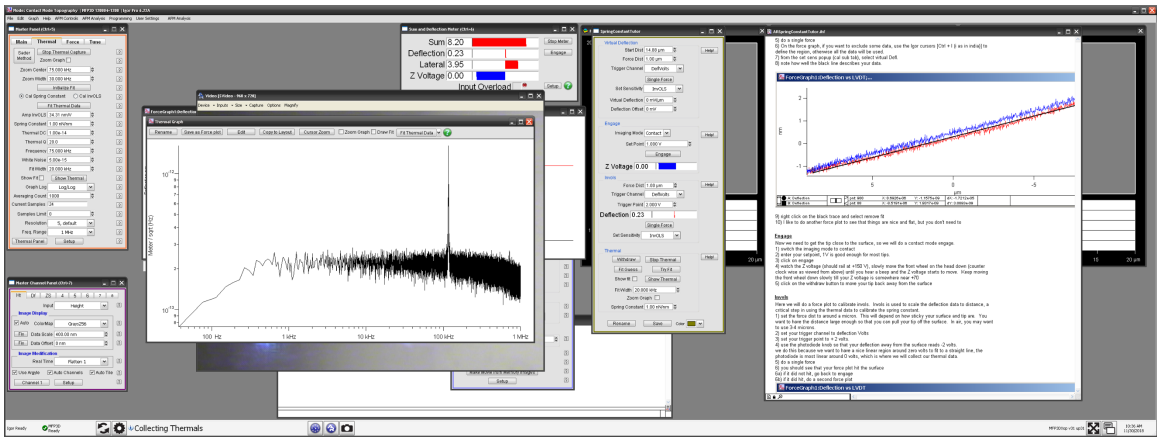

Figure 6

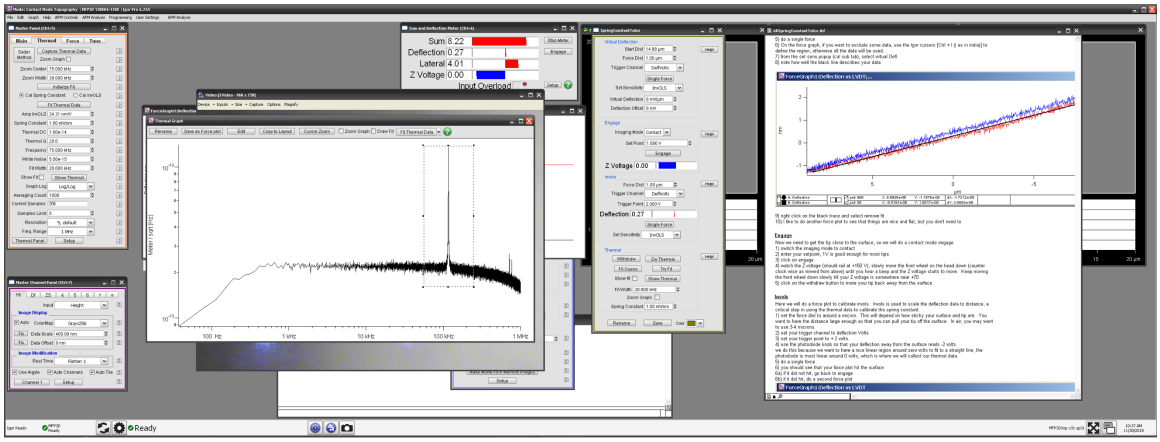

Figure 7

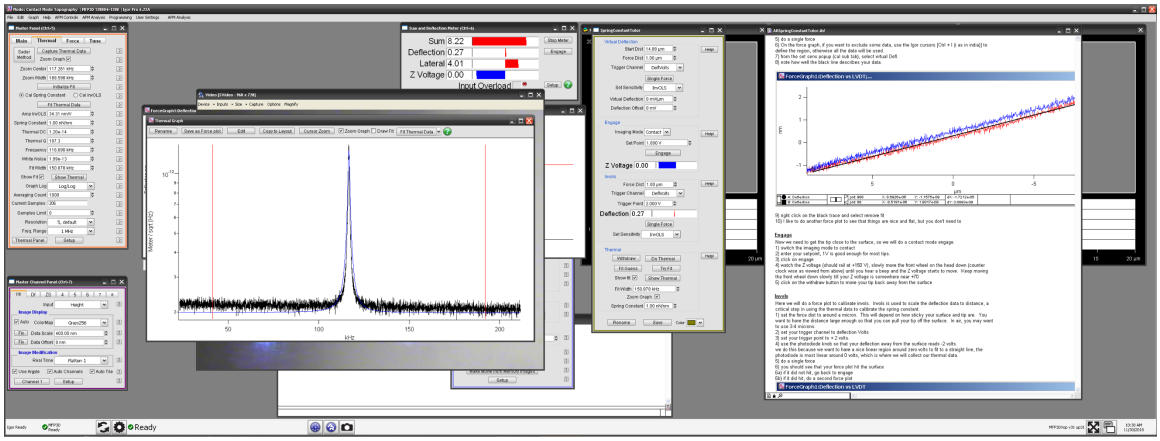

Figure 8

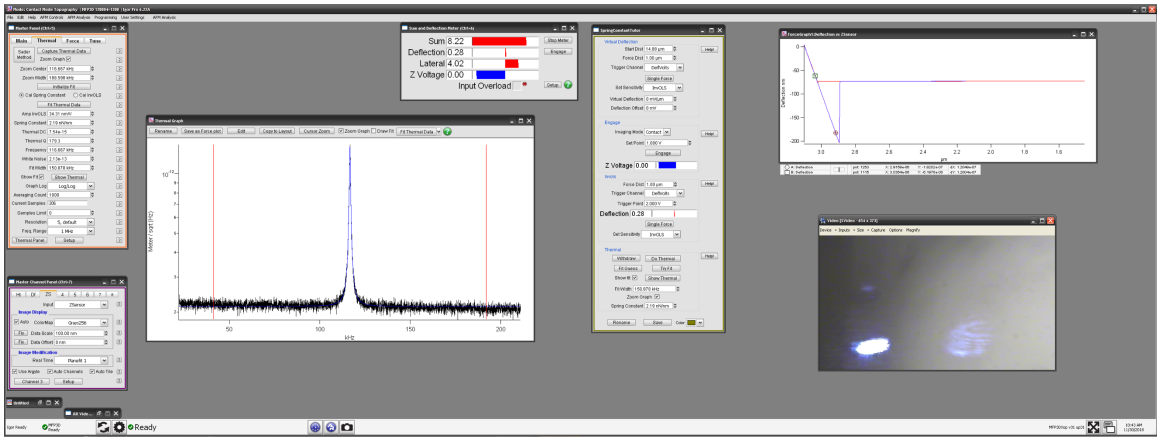

Figure 9